Neural network structure, onset and propagation of epileptic seizures

Juliette Courson

Neural network structure, onset and propagation of epileptic seizures

PhD thesis presented for the title of

DOCTOR IN INFORMATION AND COMMUNICATION SCIENCES AND TECHNOLOGIES of CY Cergy Paris Université

DOCTOR IN COMPUTATIONAL NEUROSCIENCE of the University of Warwick

Juliette COURSON

Thesis defended on the 28th of May, 2025

Rapporteuses	Dr. Simona OLMI	ISC-CNR, Italy
	Dr. Astero PROVATA	National Center for Scientific Research *Demokritos*, Greece
Examiners	Prof. Alessandro TORCINI	CY Cergy Paris Université, France
	Prof. Magnus RICHARDSON	University of Warwick, UK
President	Dr. Frédéric ALEXANDRE	INRIA Bordeaux , France
Director	Assoc. Prof. Thanos MANOS	CY Cergy Paris Université, France
Co-Directors	Prof. Mathias QUOY	CY Cergy Paris Université, France
	Prof. Yulia TIMOFEEVA	University of Warwick, UK

CERGY PARIS UNIVERSITÉ

ETIS Équipes Traitement de l'Information et Systèmes

WARWICK THE UNIVERSITY OF WARWICK

Acknowledgements

Starting with all the obvious stuff. A huge thanks to Thanos for the super nice supervision all the way from my master's thesis to this manuscript, for the unvaluable help, discussions and advice, and the support even through pretty chaotic periods. Thank you as well to Mathias for all the discussions and the great guidance along these past years. Finally, thank you to Yulia for the warm welcome to Warwick and for the insightful discussions.

I would also like to thank the many people I have had to work and chat with over the past years, for their valuable help and advices. Finally, I sincerely acknowledge Frédéric Alexandre, Simona Olmi, Astero Provata, Alessandro Torcini and Magnus Richardson for reviewing this thesis.

Merci à tous les membres du laboratoire ETIS et du LPTM, en particulier à tous les (post-) doctorants et doctorantes[1] que j'ai pu croiser, pour les pauses café, les discussions, les parties de JDR, les matchs de hockey, les bières et le reste. Merci aux permanents et aux permanentes, et à l'équipe administrative[1].

Je fais habilement la transition entre les remerciements pros et persos en adressant un merci tout particulier à Margaux, la (string-)shooting star avec qui j'ai commencé à aimer la recherche.

Merci à toustes les ami-e-s de Sarthe et de Mayenne[1] pour le fun et les bons souvenirs, les retrouvailles toujours trop rares mais jamais décevantes. Merci aux amis de Paris[1].

Merci aux parents pour m'avoir toujours ~~forcée~~ encouragée à poursuivre de belles études. Même quand il s'agissait de prendre option latin en 5^eA pendant que le reste de la classe allait faire des visites d'entreprise en mangeant des croissants. Merci aussi à Léo qui allait aux visites d'entreprise, lui (pour les exposés détaillés que j'avais absolument pas demandés sur l'abattoir de poulets). Merci à vous trois, et à toute la famille[1] (en particulier à ma tante préférée), pour le soutien moral, les fêtes, les vacances et le rire. Merci aux chats pour la supervision.

Un gigantissime merci à ma deuxième famille Gaïa, Maïanne et Pauline, qui font partie de ma vie depuis quasiment son commencement. Je suis super fière de ce que chacune a accompli.

Merci à Margaux, pour m'avoir écoutée me plaindre inlassablement et avoir regardé *Mission Impossible: Rogue Nation* en boucle avec moi.

Enfin merci à Sylvain, ex-voisin de bureau, actuel co-auteur de futures séries policières à succès. Pour ton aide au bureau, et puis en dehors du bureau. Merci de rendre chaque jour un peu plus clair que le précédent[2].

[1] Vous ne m'en voudrez pas de ne pas me lancer dans d'interminables listes de prénoms, j'ai super peur d'oublier quelqu'un donc j'ai choisi de contourner le problème.

[2] Lâcher une larme ici.

À celles et ceux qui sont partis
et à qui je pense souvent.

Abstract

Epilepsy, one of the most common neurological disorders, poses significant challenges for researchers, health practitioners and patients. Understanding neurological conditions remains challenging due to the inherent complexity of the brain, and is further complicated by ethical and practical constraints associated with invasive experiments on the human brain. Furthermore, the proportion of drug resistant epileptic patients—about a third, makes the seek for innovative treatment solutions a critically important focus. This thesis aims to leverage computational neuroscience to investigate the mechanisms underlying epileptic seizures in mice, with a particular focus on complex brain network structures and their role on seizure emergence and propagation. Through computational modeling, we aim to contribute insights that can ultimately inform human epilepsy research.

In the first research chapter of this thesis, we investigate the synchronization dynamics of forced coupled Kuramoto oscillators, embedded in rather simple network structures. This study explores the impact of different network properties on global synchrony across various network structures, and serves as a theoretical foundation for the understanding of network-driven effects in epilepsy. In the second research chapter, we computationally investigate the propagation of epileptic seizures in a large-scale mouse brain network, using the Epileptor phenomenological model for seizure dynamics. We search for common connectivity patterns across brain areas responsible for the production of widespread epileptic seizures. With a focus on Temporal Lobe Epilepsy, we simulate widespread seizures originating in the Hippocampus, and propose different strategies for propagation control mimicking resective strategies and modulation of the Epileptogenic Zone. Finally, we introduce a co-simulation framework between Arbor and The Virtual Brain (TVB), integrating fine-scale neuronal models with large-scale brain network models. Using a biophysical model for seizures at the neuron level, we simulate the emergence of seizure activity in the Hippocampus, then study its effect in a mice brain network where local brain areas are modeled using the reduced Wong-Wang model. This last study serves as a proof of concept for our co-simulation framework, and we ultimately aim to computationally study mechanisms underlying the emergence of seizures.

By bridging multiple scales of brain activity and leveraging advanced computational tools, this thesis gives insight into the role of brain network structures in the propagation of epileptic seizures.

Keywords: Epilepsy, Epileptic Seizures, Nonlinear Dynamics, Complex Systems, Complex Networks, Synchronization, Whole Brain Dynamics, Neurocomputational Platforms, The Virtual Brain, Arbor, Mouse Brain

Résumé

L'épilepsie, l'un des troubles neurologiques les plus répandus, constitue un enjeu important pour les chercheurs, les professionnels de santé et les patients. Comprendre les troubles neurologiques reste un défi de part la complexité inhérente au cerveau, et subit les limites des contraintes éthiques et pratiques associées aux expérimentations invasives sur le cerveau humain. De plus, la proportion de patients pharmaco-résistants—environ un tiers, rend la quête de solutions innovantes pour le traitement de l'épilepsie un centre d'intérêt important pour la recherche. Cette thèse vise à utiliser les outils des neurosciences computationnelles pour examiner les mécanismes sous-tendant les crises d'épilepsie chez la souris, avec un intérêt particulier pour les structures complexes de réseaux neuronaux et leur rôle dans l'émergence et la propagation des crises. Au travers la modélisation computationnelle, cette thèse a pour ambition de contribuer à une connaissance approfondie du cerveau, et, à terme, de participer à la recherche sur l'épilepsie chez l'humain.

Dans le premier chapitre de recherche de cette thèse, nous étudions la dynamique de synchronisation d'oscillateurs de Kuramoto, couplés via des réseaux aux structures relativement simples. Cette étude examine l'impact de différentes propriétés des réseaux sur la cohérence globale à travers plusieurs structures, et sert de fondation théorique pour la compréhension de la dynamique des réseaux neuronaux dans l'épilepsie. Dans le second chapitre de recherche, nous étudions computationnellement la propagation de crises d'épilepsie dans le réseau cérébral des souris à large échelle, en utilisant le modèle phénoménologique de l'Epileptor. Nous cherchons des patterns de connectivité communs aux aires cérébrales responsables de la production de crises généralisées. Avec un intérêt dirigé vers l'épilepsie du lobe temporal, nous simulons des crises généralisées provenant de l'Hippocampe, et nous proposons différentes stratégies visant à contrôler leur propagation, liées à des disconnections de voies neuronales et à la modulation de la Zone Epileptogène. Enfin, nous présentons un environnement de co-simulation entre Arbor et The Virtual Brain (TVB), intégrant des modèles neuronaux à fine échelle et des modèles de réseaux cérébraux à grande échelle. En utilisant un modèle biophysique de crises à l'échelle du neurone, nous simulons l'émergence de crises dans l'Hippocampe, puis en étudions les effets dans un réseau cérébral de souris où les aires cérébrales sont représentées par le modèle réduit de Wong-Wang. Cette dernière étude sert de preuve de concept pour notre environnement de co-simulation, et nous visons, à terme, à étudier les mécanismes sous-tendant l'émergence des crises.

En faisant le lien entre différentes échelles d'activité cérébrale, et en tirant profit d'outils informatiques avancés, cette thèse apporte un éclairage sur le rôle des structures des réseaux cérébraux dans la propagation des crises d'épilepsie.

Mots-clés: Epilepsie, Crises d'Epilepsie, Dynamique Non-linéaire, Systèmes Complexes, Réseaux Complexes, Synchronisation, Dynamique Cérébrale, Plateformes Neurocomputationnelles, The Virtual Brain, Arbor, Cerveau de souris

List of publications

Published

- **Juliette Courson**, Thanos Manos and Mathias Quoy (2023). *Networks' modulation: How different structural network properties affect the global synchronization of coupled Kuramoto oscillators.* Chaos, Fractals and Complexity, vol. 77, no. 1, pp. 233–244. Springer Proceedings in Complexity. DOI: 10.1007/978-3-031-37404-3_16.

- **Juliette Courson**, Mathias Quoy, Yulia Timofeeva and Thanos Manos (2024). *An exploratory computational analysis in mice brain networks of widespread epileptic seizure onset locations along with potential strategies for effective intervention and propagation control.* Frontiers in Computational Neuroscience, vol. 18. p. 1360009. DOI: 10.3389/fncom.2024.1360009.

In preparation

- Thorsten Hater, **Juliette Courson**, Han Lu, Sandra Diaz Pier, Thanos Manos (2025). *Arbor-TVB: A novel multi-scale co-simulation framework with a case study on neural-level seizure generation and whole-brain propagation*, to be submitted.

Funding

This thesis was supported by the LABEX MME-DII (ANR-16-IDEX-0008).

List of Abbreviations

Acronym	Meaning
AP	Action Potential
ASM	Antiseizure Medication
BOLD	Blood Oxygen Level Dependent
DB	Depolarization Block
DG	Dentate Gyrus
DMN	Default Mode Network
EEG	Electroencephalography
ECS	Extracellular Space
ENTC(l, m)	Entorhinal Cortex (lateral part, medial part)
EZ	Epileptogenic Zone
FC	Functional Connectivity
FP	Fixed Point
GFP	Green Fluorescent Protein
HB	Homoclinic Bifurcation
HF	Hippocampal Formation
HS	Hippocampal Sclerosis
ICS	Intracellular Space
ILAE	International League Against Epilepsy
MF	Mean-Field
MPI	Message Passing Interface
MRI	Magnetic Resonance Imaging
MTLE	Mesial Temporal Lobe Epilepsy
PZ	Propagation Zone
RS	Resting-State

Acronym	Meaning
RSN	Resting-State Network
SC	Structural Connectivity
SIA	Sustained Ictal Activity
SLE	Seizure-Like Event
SN	Saddle-Node
SNIC	Saddle-Node on Invariant Circle
ST	Spike Train
STP	Serial Two-Photon Tomography
SUB	Subiculum
SWE	Spike and Wave Event
TS	Tonic Spiking
TVB	The Virtual Brain
TVMB	The Virtual Mouse Brain
VGC	Voltage-Gated Channel

General introduction

Epilepsy is among the most common neurological disorders, yet it continues to present considerable challenges, both in understanding its mechanisms and developing effective treatments. Epileptic seizures may arise from physiological dysfunctions at the neuronal level or structural abnormalities, combined with network effects, making them highly complex phenomena. Studying epilepsy is particularly challenging due to the ethical and practical constraints associated with invasive experiments on the human brain. Over the past decades, the theoretical and computational study of neurological conditions has expanded significantly, driven by the widespread availability of enhanced computational resources. Building on this trend, we propose to investigate the impact of neural network structures on the emergence and propagation of epileptic seizures in the mouse brain from a computational perspective, with the long-term goal of translating this knowledge to the human brain.

Outline

This thesis comprises an introductory chapter as well as three research chapters, two of which being adapted from published work.

- **The first chapter of this manuscript aims to provide general introductions** about epilepsy and brain function, complex networks' theory and non-linear dynamics. It concludes with the presentation of three models for brain activity, namely the reduced Wong-Wang model for macro-scale resting-state activity, the Epileptor model for macro-scale epileptic activity, and a micro-scale biophysical model for seizures.
- **The second chapter presents a computational study of the impact of different network properties on the synchronization of forced coupled Kuramoto oscillators**. In the context of this thesis, this work serves as an introduction for a better understanding of complex network effects under various structural constraints.
- **The third chapter uses the Epileptor model in order to study the propagation of epileptic seizures in mice brain**. It aims to identify common connectivity patterns across epileptogenic brain areas responsible for widespread seizures, and seek for novel approaches for seizure propagation control.
- Finally, **the fourth chapter of this thesis presents ongoing research on the construction of a multi-scale simulation framework for brain activity**, combining fine-scale models of detailed brain areas and mean-field models of brain networks at the large scale. As a proof of concept, we simulate the emergence of seizures in a neuronal population and observe their propagation in the mice brain network.

Contents

Part I

State of the art: Complex network dynamics, brain structure and models of epilepsy

1 Epilepsy and seizure classification

1.1 The epileptic condition: an overview

Epilepsy is a very common neurological disorder. According to the World Health Organization (WHO), around 50 million people in the world suffer from epilepsy (Keezer *et al.* 2016). Epilepsy is characterized by multiple occurrences of so-called epileptic seizures, that is, the production of abnormally excessive and synchronous electrical signals in the brain. These seizures are accompanied by a wide range of symptoms such as loss of consciousness, motor dysfunctions or sensory hallucinations, which are further detailed in section I.1.3.3. In addition to these symptoms, epileptic patients are subject to numerous psychological, cognitive and behavioral comorbidities, such as depression, dementia and heart diseases to name a few. To say the least, epilepsy is a very complex, serious brain disorder, and appropriate patient care is essential.

1.1.1 A historical perspective on epilepsy

First traces of epileptic seizures appear in mesopotamian and babylonian tablets dating from around 3000 BC, with reports of people convulsing, dribbling and being unconscious (Kaculini *et al.* 2021). Back then, and for millenia to come, epileptic seizures would be considered spiritual possessions or divine punishments, and treatment of epilepsy would essentially consist in exorcisms, rituals and persecutions. An early documentation of seizures from a medical perspective appears in an ancient Egyptian papyrus from around 1700 BC, documenting the case of a man having a gaping wound in the head. The palpation of the wound would cause the patient to shudder excessively, leading to the conclusion that the seizure is caused by cortical disturbance. The 5th century before Christ represents a turning point in the understanding of epilepsy, then referred to as the Sacred Disease, with the School of Hippocrates pointing out that the brain might be the source of the disease, and conceptualizing post-traumatic epilepsy, auras and unilateral motor signs. These theories were running counter to the ever-omnipresent thought of divine anger (Magiorkinis *et al.* 2010; Kaculini *et al.* 2021).

It was not until the 17th century that the idea of epilepsy as a brain disease began to become popular in Europe. Scientific advances in epilepsy went hand in hand with a finer understanding of the brain and recent advances in physics. In the mid 17th century, Robert Bentley Todd, driven by the work of Michael Faraday and the emergence of microscopes in the medical field, developed a (now-)rudimentary understanding of the neuron, and of the brain function as electric forces. He postulated that the epileptic seizures would come from disruptive electrical discharges (Reynolds 2004). The end of the century was marked, among others, by the contribution of John Hughlings Jackson, who laid the foundations of epileptology, defining epilepsy as "occasional, sudden, excessive, rapid and local discharges of grey matter", and linking symptoms with specific seizure-recruited cortical areas (Sidiropoulou *et al.* 2010; Magiorkinis *et al.* 2014).

1.1.2 Epilepsy in the world

Today's perception of epilepsy still bears the stigmata of ancient spiritual beliefs. Previous terminology, still in common use, refers to focal and generalized seizures (that is, seizures affecting respectively one or both hemispheres of the brain) as *petit mal* and *grand mal*, that is, small evil and great evil. However, modern perception and management of epilepsy has evolved significantly over the past decades, hand in hand with scientific and technological advances. Several treatment strategies, including medication, surgery but also brain stimulation, are nowadays in use. Research and development keeps working towards a better understanding of epilepsy, and even more efficient and less invasive treatments.

However, access to diagnosis and treatment remains highly unequal. Over 75% of individuals in low-income countries do not receive adequate care due to limited healthcare infrastructure. Social stigma and lack of education also results in marginalization and discrimination of people with epilepsy (Mlinar *et al.* 2016). Epilepsy remains a major challenge for medicine and neuroscientific research.

1.2 Emergence of epileptic seizures

The emergence of epileptic seizures results in a disruption of normal neuronal activity. Understanding the physiological causes of epileptic seizures is a major challenge for the development of antiepileptic drugs. This section aims to present the basic functioning of neurons and neurotransmission, whose dysfunction may underlie the production of seizures.

1.2.1 Transmission of information: the neurons and the action potential

Basic neuron morphology

Neurons are the excitable cells of the nervous system. The human brain approximately contains 86.10^9 neurons, while a mouse brain contains about 71.10^6 neurons (Herculano-Houzel *et al.* 2006). Their complex network arrangement, high sensitivity and excitability are responsible for the brain's ability to perform multiple, complex and coordinated tasks. The neuron consists of a soma and an axon (see **Figure** I.1 **(A)**). At the soma and the axon terminal, arborescent dentrites connect the cell to other neurons, via synapses at the extremity of the dendritic branches. The axons are long projections of the cell, typically protected by a myelin sheath, that consitute the white matter of the neural system. The neurons' cell bodies and dendrites, the glial cells, synapses and capillaries, on the other hand, constitute the brain's grey matter.

After the production of an electric signal is triggered, the cell nucleus produces an action potential (AP) that propagates along the axon. The arrival of the AP at the axon terminal triggers the release of neurotransmitters in the synapses, that consequently trigger the firing of other neurons.

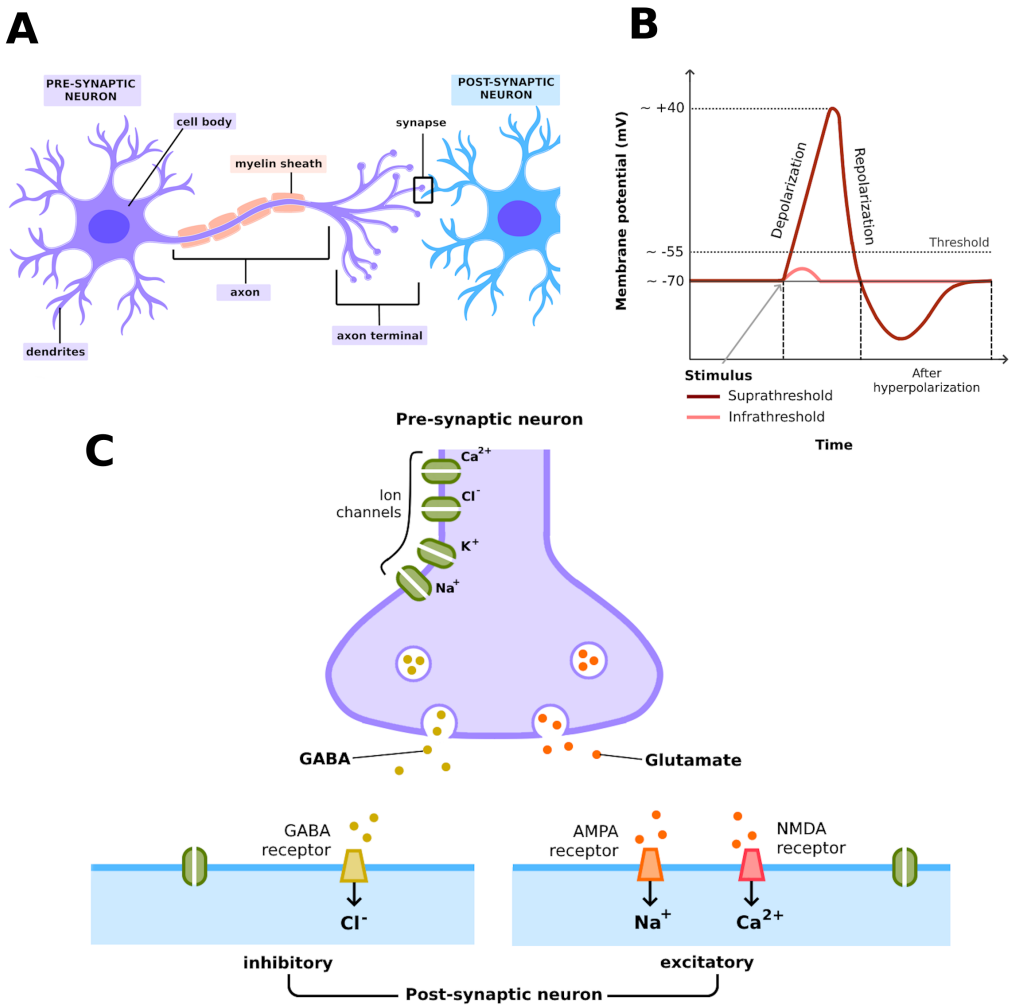

Figure I.1: **Transmission of information at the neuron level. (A)** Neuron morphology. Action potentials (AP) are produced by the pre-synaptic neuron and propagate along its axon. The axon terminal communicates with the post-synaptic neuron's dendrites via the synapse. **(B)** Time evolution of the membrane potential during the production of AP. After suprathreshold stimuli, the cell membrane undergoes a depolarization phase, followed by a repolarization phase. A refractory period brings back the potential to its resting baseline. **(C)** Transmission of information at the synapse level. The arrival of AP at the pre-synaptic neuron axon terminal triggers the release of neurotransmitters in the synapse. On the dendrites of inhibitory (resp. excitatory) post-synaptic neurons, neurotransmitters bind to the GABA (resp. Glutamate) receptors, favoring depolarization (resp. hyperpolarization) of the post-synaptic neuron membrane.

Resting membrane potential

The action potential is the consequence of a modification in the membrane potential of the cell (Kandel *et al.* 2013). The ionic concentration of the intra and extra-cellular environment are regulated by different gating mechanisms along the membrane. Many ions compose theses environments, including mainly sodium Na^+, potassium K^+, calcium Ca^{2+} and chloride Cl^-. **Ion channels** are macromolecular pores, through which specific ions can pass. Ion channels may be non-gated and allow the movement of ions across the cell membrane at any time, or be gated. In the latter case, the channel is only open to specific ions under specific conditions. Voltage-gated ion channels open when a particular electric potential difference is reached, while ligand-gated channels open after a ligand binds to the channel. Ion channels form a passive process in which each ion follows its concentration gradient across the membrane. In other word, if channels are open for ions X, and the concentration $[X]$ of ions X is higher outside the cell (resp. inside the cell), then there will be a flow of ions towards the interior (resp. exterior) of the cell. **Ion pumps** are an active transport process, that intervenes against the concentration gradient. A well-know ion pump is the sodium-potassium pump. By hydrolyzing a molecule of adenosine triphosphate (ATP), the pump gains energy and moves $3Na^+$ out and $2K^+$ in.

At rest, there is therefore a difference of the ionic concentrations on both side of the membrane, from which comes a difference of electrical charges. The equilibrium potential of ion X, at rest, is given by the Nernst equation:

$$V_{eq,X} = \frac{RT}{z_X F} \ln \frac{[X]_o}{[X]_i}, \tag{I.1}$$

with $[X]_o$ (resp. $[X]_i$) the concentration of ion X outside (resp. inside) the cell, z_X the valence of ion X, $R = 8.314$ J.K^{-1}.mol^{-1} is the universal gas constant, $F = 96.485$ C.mol^{-1} is the Faraday constant, and T is the temperature in Kelvin. The principal contributors to the total electrical gradient are K^+, Na^+ and Cl^-. The cell membrane potential reads:

$$V_m = \frac{g_K V_{eq_K} + g_{Na} V_{eq,Na} + g_{Cl} V_{eq,Cl}}{g_K + g_{Na} + g_{Cl}}, \tag{I.2}$$

with g_X the conductance of ion X. The neuronal membrane potential usually falls around $V_m \approx -70$ mV (Hou 2020).

Action Potential

The stimulation of the membrane, due to electrical stimuli or ion channel activations, disturb the resting equilibrium of the membrane. In the case of an hyperpolarizing stimulus, for example an influx of negative ions in the cell or a loss of positive ions via the openings of the Cl^- and K^+ channels, the response in terms of membrane potential is graded, that is, dependent of the stimulus intensity. In the case of a

depolarizing stimulus, for example the arrival of more positive charges into the cell via the opening of Na^+ and Ca^{2+} channels, may lead to the production of an AP. The shape of AP is shown in **Figure** I.1 **(B)**. Disturbances keeping the membrane potential bellow the threshold potential $V_{thresh} \approx -55$ mV, namely subthreshold stimuli, generate graded responses. On the contrary, suprathreshold stimuli generate an AP whose features do not depend on the stimulus intensity. Once reached its critical value, V_m rapidly increases due to the opening of voltage-gated Na^+ channels (VGNaCs) leading to an influx of Na^+ into the cell. This rapid **depolarization phase** causes more VGNaCs to open, and utlimately, to more depolarization. The initial depolarization also causes a flux of K^+ leaving the cell, with a slower opening process of voltage-gated K^+ channels (VGKCs). When reaching positive values, VGNaCs progressively close, while more K^+ tend to leave the cell due to the electrical gradient. The continued loss of $K+$ drags the membrane trough sub-initial potential values during a rapid **repolarization phase**. Finally, an **after hyperpolariztion** process occurs, during which the membrane voltage slowly returns to its baseline (Raghavan *et al.* 2019; Sankaraneni & Lachhwani 2015).

Neurotransmitters: inhibition, excitation

The arrival of an AP at the presynaptic terminal triggers the release of neurotransmitters in the synapse that bind to the postsynaptic receptors, resulting in ion channel activation and consequent electrical signal production as described above. Receptor agonists refer to chemicals activating the receptor. On the contrary, antagonists are chemicals blocking the receptor, see **Figure** I.1 **(C)** for a schema of the synapse.

The principal excitatory neurotransmitter of the nervous system is the glutamate, whose receptors include the ionotropic NMDA, AMPA and kainate receptors. The latter receptors form ligand-gated Ca^{2+} and Na^+ channels, that generates influx of positive charges upon activation, therefore favoring membrane depolarization. The principal inhibitory neurotransmitter is the gamma-aminobutyric acid (GABA). GABA receptors include $GABA_A$ and $GABA_B$. $GABA_A$ receptors form postsynaptic ligand-gated Cl^- channels, favoring membrane hyperpolarization through influx of Cl^-. Inhibition and excitation in the brain are mediated by different types of neurons. In particular,pyramidal cells are either intrinsic or long-range excitatory neurons, and play a key role in signal transmission between distant brain areas. Basket cells, on the other hand, are inhibitory interneurons in the brain that form synapses around the soma of pyramidal cells, and are especially important in regulating their activity and contributing to network stability.

The metabolism of glutamate and GABA are tied together via the glutamate-glutamine and GABA-glutamate/glutamine cycles of the brain. After glutamate neurotransmitter is released in the synapse and interacted with postsynaptic receptors, both the presynaptic neuron and glial cells recapture glutamate. In the glial cell, glutamine is produced from glutamate, before being transfered to glutamaergic neurons, where they react to produce glutamate. Similarly, the glutamate produced

in GABAergic neurons reacts to form GABA. After reuptake at the synapse, glial cells produce glutamate with GABA, using the enzyme GABA-T. The homosteasis of neurotransmitters is preserved through these metabolic cycles (Walls *et al.* 2014).

1.2.2 Initiation of epileptic seizures

Epileptic seizures arise from the production of excessive and synchronous electrical signals within a population of cortical or subcortical neurons. This active phase of abnormal brain activity is called the *ictal* phase of the seizure. Several factors can give rise to neuronal hyperexcitability, such as an increase of excitatory neurotransmission, a decrease of inhibitory neurotransmission, or alterations in voltage-gated ion channels or intracellular and extracellular ion concentration favoring membrane depolarization. These mechanisms represent the basic targets for antiepileptic drugs (see section I.1.4.1). During a seizure, hyperexcitable, hypersynchronous neurons fire following a bursting pattern, that is, the production of rapid trains of AP followed by long refractory periods. Bursts operate on two distinct time scales, neurons being recruited into abnormal firing by a slow ictal wavefront, while faster ictal discharges depicts a propagation of abnormal excitation-inhibition ratios into brain areas (Sumadewi *et al.* 2023).

However, epileptic seizures are not a direct consequence of individual neurons' dysfunction. On the contrary, both their generation and their propagation are complex, network phenomena, resulting from the interaction of distant pyramidal neurons, local circuit basket cells, cortical and subcortical areas.

1.3 Seizure and epilepsy classification

From the first medical reports of epilepsy, the nomenclature has varied greatly over the course of scientific and social advances, and both the terminology and classification are frequently updated to follow the progress in medicine, neuroscience and neurology, and will continue to evolve in the future. This section presents the latest classification published in 2017 by the International League Against Epilepsy (ILAE) (Scheffer *et al.* 2017), based on scientific knowledge and specialists' opinion. The diagnostic process relies on a clinician expertise, and on neuroimaging data, mainly EEG. **Figure** I.2 presents an overview of the main cerebral areas, and further details on the anatomy of the brain and on brain imaging are provided in section I.2.

1.3.1 Epilepsy etiology

Epileptic activity in the brain can arise from various causes, making accurate identification essential for providing appropriate medical care. The underlying etiology of epilepsy may be structural, genetic, immune-related, metabolic, or infectious in nature.

The presence of **structural** abnormalities in the brain, either they are coming from genetic malformation or appearing after undergoing traumatisms, strokes or infections. These brain lesions are detected using structural MRI, and open the way for epilepsy surgery. Well-known lesions associated with epileptic seizures are, among other, hippocampal sclerosis and hypothalamic hamartoma (HH). Hypothalamic hamartoma is a developmental tumor in the ventral region of the Hypothalamus, a region often related to learning and cognitive disabilities, psychiatric disorders (particularly, but not exclusively, aggressive behaviors) and production of epileptic seizures. The seizures experienced are mainly gelastic, characterized by sudden uncontrollable laughing (Wang *et al.* 2023; Cohen *et al.* 2021; Adamczyk *et al.* 2021). Hippocampal sclerosis (HS) is one of the principal causes of focal epilepsy. It refers to gliosis and neuronal loss in the different parts of the Hippocampus. The origins of HS may be a combination of diverse factors, either coming from infections or brain injuries, with probable genetic and developmental predispositions. The Hippocampus being very vulnerable to damage caused by seizures, HS could be both the cause and consequence of prolonged epileptic activity (Walker 2015; Thom 2014). The examples of HH and HS clearly illustrate the fact that there can be multiple etiologies of epilepsy, whose different implications for treatment all have to be considered.

1.3.2 Epileptogenic Zone and seizure types

Excessive electrical discharges often originate in specific regions of the brain, known as the Epileptogenic Zone (EZ) before spreading to other areas forming the Propagation Zone (PZ). The current classification sorts the resulting epileptic seizures according to their EZ and PZ:

- **Focal onset seizures** arise within a single brain hemisphere. Among these seizures, focal to bilateral seizures refer to seizures arising within a single brain hemisphere, but propagating in both hemispheres. Focal seizure can affect or not the awareness of the patient, and generate various sensory and motor symptoms.
- **Generalized onset seizures** arise on different brain regions located in both left and right brain hemispheres. Generalized seizure always affect the patient's awareness.
- **Unknown onset seizures** group together epileptic seizures that can not be classified in any of the previous categories, due to the lack of information.

By extension, the different types of epilepsy are divided within focal epilepsies, generalized epilepsies and combined focal and generalized epilepsies.

1.3.3 Seizure semiology

As the seizure propagates within different brain areas, symptoms and clinical signs appear. The brain areas and cortical networks activated or disrupted by

the seizure form the Symptomatogenic Zone. The impacted brain areas generate different symptoms. Therefore, retracing the semiology of an epileptic seizure, via neuroimaging, clinical history and observations, can help both obtaining precise diagnosis of epilepsy and localizing the EZ that could be surgically removed (Tufenkjian & Lüders 2012).

Several motor manifestations of epileptic seizures include **tonic** (tension in the members and upper body), **atonic** (limpness of various parts of the body), **clonic** (jerking in the arms and legs), **myoclonic** (brief jerking in various parts of the body), **epileptic spams** (clusters of brief flexions of extensions of the head and members). Non-motor manifestations include **automatisms** (unvoluntary movements, such as grimacing or chewing), **cognitive dysfunctions** (such as speech impairment), **emotional alterations** (sudden feeling of fear and anxiety, or uncontrollable laughing, for example), **sensory feature**s (such as visual, auditory or gustatory hallucinations, vertigos, hot and cold sensations). During an epileptic seizure, the patient might suffer from one or more of these clinical signs. They may appear in one side of the body, either ipsilateral (on the same side as the seizure-recruited brain hemisphere) or contralateral (on the opposite side as the seizure-recruited hemisphere), or in both sides. Finally, the patient may suffer from a loss of awareness at different levels, from confusion to loss of consciousness (Chowdhury *et al.* 2021).

The symptoms and clinical signs experienced during a seizure arise from the dysfunction of particular brain areas. Seizures originating in the frontal lobe are often associated with motor symptoms, and can sometimes lead to confusion or loss of awareness. Temporal lobe seizures typically manifest as sensory symptoms, such as auditory hallucinations, sensation of déjà vu, or olfactory distortions, along with emotional changes. Seizures affecting the parietal lobe can cause sensory disturbances, such as numbness, tingling, or a distorted sense of body position, and may also involve visual symptoms. The occipital lobe is primarily linked to visual disturbances, including hallucinations or temporary loss of vision. Furthermore, subcortical structures like the thalamus and basal ganglia are often involved in more generalized motor symptoms, such as myoclonus or dystonia, and can also lead to autonomic changes, such as alterations in heart rate or breathing, see **Figure** I.2.

1.4 Treatment of epilepsy

The main objective of the different treatment strategies is to prevent the occurrence of epileptic seizure. The best possible outcome is to achieve seizure freedom, and even remission, with several years of seizure freedom after surgery or medication discontinuation. A reduction of frequency and intensity of experienced seizures may also constitute a relatively good outcome (Sillanpää *et al.* 2017).

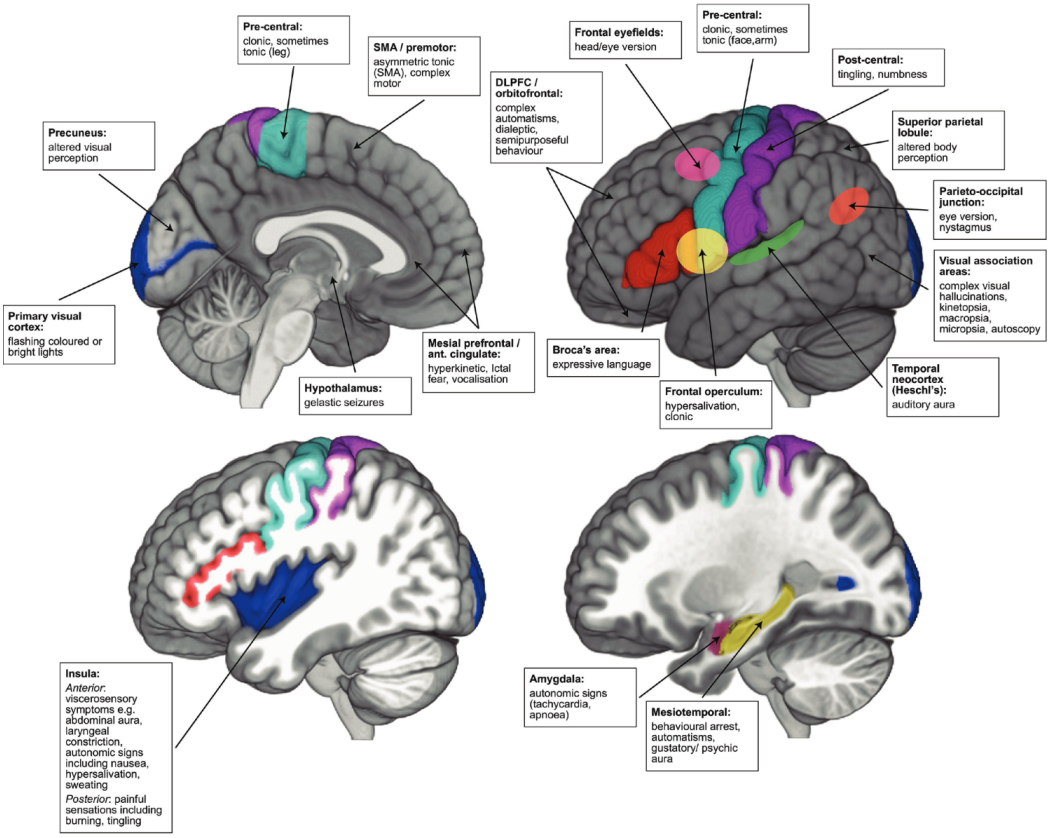

Figure I.2: **Summary of semiological signs by symptomatogenic zone on mesial and lateral structures.** DLPFC, dorsolateral prefrontal cortex; SMA, supplementary motor area. **From:** Chowdhury FA, Silva R, Whatley B, et al. *Localisation in focal epilepsy: a practical guide.* Practical Neurology 2021;21:481-491. Reproduced with permission from BMJ Publishing Group Ltd., License No. 5983611502290.

1.4.1 Anti-epileptic medication

Antiseizure medication (ASM) is the most common strategy to treat epilepsy. Nowadays, over 30 ASM are available to suppress seizure activity in the brain. They rely on different mechanisms at the molecular level (Sankaraneni & Lachhwani 2015; Sánchez *et al.* 2024):

- **Modulation of ion channels.** ASMs such as phenytoin, ethosuximide and ezogabine act on Na^+, Ca^{2+} and K^+ ion channels of excitatory and postsynaptic neurons, in favor of a membrame hyperpolarization.
- **Enhancement of inhibitory neurotransmission.** ASMs may act on diverse phases of the GABA cycle, either binding to the $GABA_A$ receptors of the postsynaptic neurons to enhance inhibition (for example benzodiazepines), inhibiting the GABA-degrading enzyme GABA-T in the glial cells (for example vigabatrin), or preventing the recapture of GABA in the synapse (for example tiagabine).
- **Attenuation of excitatory neurotransmission.** ASMs such as perampanel or felbamate target the glutamate neurotransmitter, by blocking NMDA and AMPA receptors at the level of the postsynaptic neuron.

ASMs may act on a single or on several of these targets. Consequently, the action of so-called narrow-spectrum ASMs is fitted to prevent specific types of seizure, while broad-spectrum ASMs acts on multiple types of seizures.

As all drugs do, ASMs may present multiple side-effects and contraindications. 30% of epileptic patients suffer from refractory epilepsy, either due to unresponsiveness to medication, or to high sensitivity to side-effects or contraindications making the medical treatment impossible. Epilepsy syndromes frequently associated with pharmacoresistance include Mesial Temporal Lobe Epilepsy (MTLE), one of the most common epilepsy syndrome, where seizures initiate within the Hippocampus.

1.4.2 Focal resective surgery

Currently, the principal approach to control epileptic activity in pharmacoresistant patients consists in the resection of the brain area producing epilepsy. Frequent resected areas include portions of the temporal, frontal, parietal and occipital lobes. The most frequent operation, with the best outcomes, consists in anterior temporal lobectomy for people with MTLE, that is, the resection of the hippocampus and part of the amygdala. The surgery results in seizure freedom for up to 70% of the patients. The surgery is ineffective in 10 to 15% of the patients. When epileptic seizures are caused by structural abnormalities such as benign tumors or HS, the resection of the lesion and the surrounding brain tissue is also a common strategy (Jobst & Cascino 2015; Miller & Hakimian 2013).

Candidates for resective surgery should have focal epilepsy with a well-identified EZ. The latter brain area should also be accessible, and not critical in brain function.

To obtain good surgical outcomes, surgeons have to resect enough brain tissue to effectively remove the seizure initiation area. However, they should also seek to minimize the risk of neurologic and cognitive alterations. Resecting more tissue in the identified area results in higher chance of seizure freedom, but also higher risk of serious undesirable effects.

1.4.3 Alternative techniques to resective surgery

Resective surgery is a highly invasive, costly and risky operation. Therefore, alternative techniques aim to propose minimally invasive, faster and more precise solutions. Such techniques are commonly used for refractory epilepsy with small lesions and localized EZ, for example in MTLE with HS or epilepsy with HH. They can also be used for disconnection surgery to resect important pathways between the brain areas, and prevent the wide spread of the seizure. It is the case in corpus callosotomy, where the surgical target is the corpus callosum, a major nerve tract of the brain.

- **Laser Interstitial Thermal Therapy (LITT)** is a minimally invasive ablation technique, that does not require any craniotomy. It uses a thin laser probe inserted in the brain through a hole in the skull. At the level of the neuronal population responsible for the production of epileptic seizures, the tip of the probe acts as a focal heat source, that induces nearly immediate cell death by applying high temperatures over 60°C. To apply an optimal temperature, and to control the position of the probe, the LITT process is monitored using MRI (Shukla *et al.* 2017; Wicks *et al.* 2016).
- **Stereotactic radiosurgery (SRS)** is a non-invasive ablation technique, that does neither require craniotomy nor any incision in the skull or brain. SRS devices aim to reach precise targets with focal ionizing radiation beams. Photons form the most common radiation source, with multiple beams directed to a single target (Quigg *et al.* 2011).
- **Multiple Subpial Transections (MST)** is a lesionectomy technique, used in cases where the epileptogenic zone is located in cortical areas involved in essential brain functions. It consists in performing several cuts on the grey matter below the external membrane of the brain in order to disrupt fiber pathways involved in the propagation of the seizure instead of perform ablation of the brain tissue (Spencer *et al.* 2002).

1.4.4 Neurostimulation devices

Electrical devices may be used to send stimuli to brain areas in order to modulate brain activity. Neurostimulation is used to treat severe neurological conditions, mainly Parkinson's disease and refractory epilepsy. For patient with refractory epilepsy, neurostimulation devices can be used alternatively, or in addition to surgical and medical treatments, to suppress seizures or reduce frequency and intensity. Although the mechanisms of neurostimulation is yet to be fully understood,

it was shown that it can effectively reduce seizure frequency and intensity, with 50 to 68% of epileptic seizure reduction in patients using Deep Brain Stimulation (Wu *et al.* 2021).

- **Vagus Nerve Stimulation (VNS)** consists in an electrical generator implanted on the chest and wired to the Vagus Nerve. The device produces electrical pulses at regular intervals, continuously helping modulate brain activity (Fisher & Velasco 2014; Foutz & Wong 2022).
- **Deep Brain Stimulation (DBS)** involves one or multiple electrodes implanted in deep brain areas, through a small hole in the skull and under MRI guidance. Similarly to VNS, an electrical generator is implanted on the chest, and delivers electrical pulses to modulate brain activity (Li & Cook 2018).
- **Responsive Neurostimulation (RNS)** delivers brain stimulation when abnormal brain activity is detected. It consists in an electrical generator implanted in the skull, combined with electrodes placed on the initiation areas of epileptic seizures. The device continuously monitors brain activity, and provides modulation whenever seizure starts arising (Rao & Rolston 2023).

2 Network topology and the reconstruction of brain networks

Computational and theoretical studies of the brain leverage tools from fundamental physics. In particular, the mapping of complex brain structures aims to incorporate empirical data within a mathematical framework. This section outlines the mathematical foundation of network theory, then presents the main brain imaging techniques used for network reconstruction. Finally, it showcases the structure of brain networks.

2.1 Complex networks: an overview

Network structures are omnipresent in nature, in human creations, and in the human society itself. We call *networks* structures of inter-connected elements. In a big city, multiple subway stations are spatially connected via different train lines, which make navigating the city possible from any station. In the human society, people themselves are connected through their social interactions and relationships. In the brain, billions of neurons connected by synapses communicate with electrical and chemical signals, and coordinate their activities to perform a large variety of tasks.

2.1.1 Mathematical formalism

Network theory aims to describe complex structures as graphs, where the elements, called *nodes* or *vertices*, are linked through *edges* (Newman 2010; Fornito *et al.* 2016). The network is described as a graph $G = (E, V)$ containing a set V of vertices and a set E of edges. The set of vertices contains N elements indexed from 1 to N: $V = \{i \in [\![1 : N]\!]\}$. The set of vertices contains all existing connections of the graph, $E = \{(i, j) \in [\![1 : N]\!]^2\}$. The element (i, j) represents a connection going from a source node i to a target node j. For simplicity, we denote such connection with $i \longrightarrow j$.

Graphs might be weighted or unweighted. If weighted, each connection is defined not only by its direction, but also by its specific weight. The strength of the connections affects how information spreads through the network, creating stronger and weaker links. Other properties might be attached to network connections, such as their length. Finally, graphs might be directed, i.e. with directional connections, or undirected, in which case E necessarily contains both (i, j) and (j, i) with the exact same properties. **Figure** I.3 shows a simple example of weighted, directed graph.

The adjacency matrix of a network $\boldsymbol{A} = (a_{ij})$ contains the information of all connections. Each element a_{ij} is equal to the weight of the connection from node i

to node j. In particular,

$$\begin{cases} a_{ij} = 0 & \text{if the connection is inexistent,} \\ a_{ij} = 1 & \text{if the connection exists and the graph is unweighted,} \\ a_{ij} \neq 0 & \text{if the connection exists and the graph is weighted.} \end{cases} \tag{I.3}$$

Note that, in the case of an undirected graph, the adjacency matrix is symmetrical.

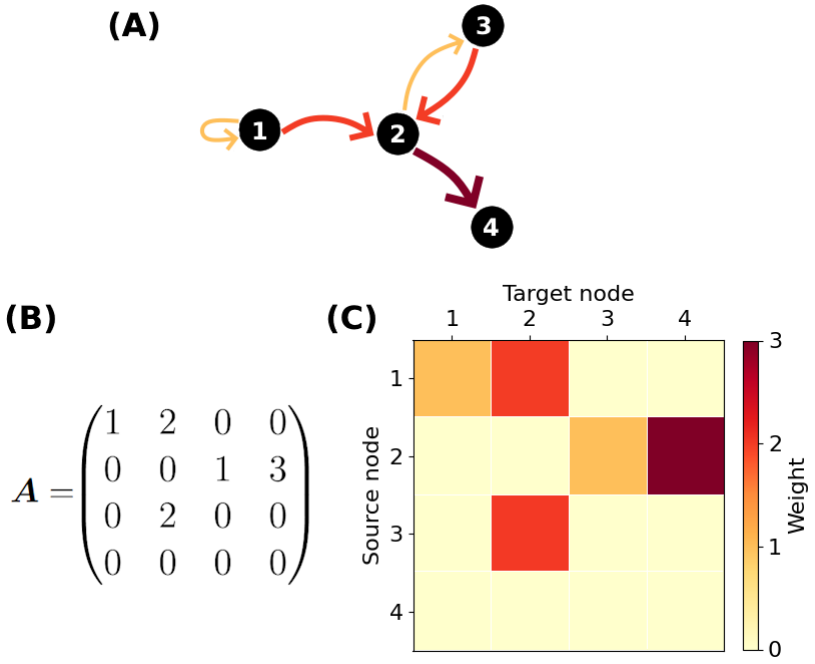

Figure I.3: **Basic example of a weighted, directed network.** **(A)** Graph representation of the network. The color and width of each edge show the weight of the connection. **(B)** Adjacency matrix of the network. **(C)** Matrix representation of the network.

2.1.2 Local network measurements

Different metrics can be used to quantify the topology of network structures, connections and nodes. The importance of individual nodes regarding different properties vary depending on the arrangement of the connections they establish with each others. This section presents several local measurements (Fornito *et al.* 2016; Newman 2010), widely used latter on this thesis.

- **Degree.** The amount of connections leaving (resp. arriving) a node i is given

by its outdegree $\deg^+(i)$ (resp. indegree $\deg^-(i)$):

$$k_i^+ = \sum_{j \in V} a_{ji}, \tag{I.4}$$

$$k_i^- = \sum_{j \in V} a_{ij}. \tag{I.5}$$

For an unweighted graph, indegree and outdegree represent a number of connections. However, in the case of a weighted graph, they take the real value of the total connective strength the node receives or releases. Moreover, for undirected graphs, $k_i^+ = k_i^-$.

- **Eigenvector centrality.** The eigenvector centrality x_i is used to quantify the relative importance of a given node i within the network. From the adjacency matrix of the network, one can derive a set of eigenvalues $\{\lambda_n\}$ and their associated eigenvectors $\{\boldsymbol{x}_n\}$ such that:

$$\lambda_n \mathbf{x}_n = \boldsymbol{A}\mathbf{x}_n. \tag{I.6}$$

For simplicity, let λ be the highest eigenvalue, and $\boldsymbol{x}$ its associated eigenvector. If all the elements of the adjacency matrix are positive, then $\boldsymbol{x}$ only has non-null elements. For each network node i, the eigenvector centrality is defined by the i^{th} element of $\boldsymbol{x}$:

$$x_i = \frac{1}{\lambda} \sum_{j \in V} a_{ij} x_j, \tag{I.7}$$

Eigenvector centrality gets higher when a node has more, stronger connections, especially connections with other central nodes of the network. In a subway network, stations with high centrality would be big stations, receiving many train lines, and connecting them to other big stations.

- **Average shortest path length.** The shortest path length l_{ij} between any two nodes i and j is the total connective length on the shortest path going from one to another . We define the average shortest path length of a node i as the mean shortest path between i and any other node of the network:

$$L_i = \frac{1}{N} \sum_{j \in V} l_{ij}. \tag{I.8}$$

Note that for l_{ij} to be defined, there has to be a way connecting node i to node j, therefore the average shortest path length is only suitable for complete graphs. The lower the shortest path length, the fastest the information goes from one node to another. For example, when building a subway network (that is, a graph of interconnected stations), one might want to minimize the stations' average shortest path length so the users can easily navigate accross the city.

- **Clustering.** The local clustering coefficient is defined for unweighted graphs. Let $k_i = k_i^+ + k_i^-$ be the degree of node i. In the case of a directed graph, $k_i(k_i - 1)$ edges can exist within its neighborhood. With n_i the number edges that actually exist, the local clustering coefficient is defined as:

$$C_i = \frac{n_i}{k_i(k_i - 1)}. \tag{I.9}$$

Note that, for undirected graphs,

$$C_i = \frac{2n_i}{k_i(k_i - 1)}. \tag{I.10}$$

That is, in a subway network where stations B and C are the next stop after station A on their line, clustering would give the probability that there exists a line directly connecting B and C.

2.1.3 Global network features

Network measurements defined in section I.2.1.2 only describe the local features of network nodes. However, global network characteristics arise from the individual nodes' topology. One can therefore define the clustering C of a network as the mean clustering of its nodes, or its shortest path length L as the mean shortest path length of its pairs of nodes. This subsection lists important global network features, illustrated in **Figure** I.4.

Small-world networks

Small-world networks exhibit both high clustering and low shortest path length (Watts & Strogatz 1998). Small-worldness is a feature of many real-life networks. In the brain, structural and functional networks of brain regions show small-world properties (Liao *et al.* 2017; Bassett & Bullmore 2016).

A simplistic version of small-world networks can be constructed from a regular unweighted, undirected lattice of nodes connected to their k nearest neighbors. The network undergoes multiple random rewiring phases: going clockwise over the lattice, a vertex and the edge to its nearest neighbor are selected. The edge is removed, and the vertex reconnected to a random node with probability p, without duplicating any existing edge. This random rewiring is repeated, considering the following nearest neighbour, until having rewired with probability p all edges of the network. Choosing p in an adequate range of values, the built network exhibits both high mean clustering and low mean shortest path length, that is small-worldness.

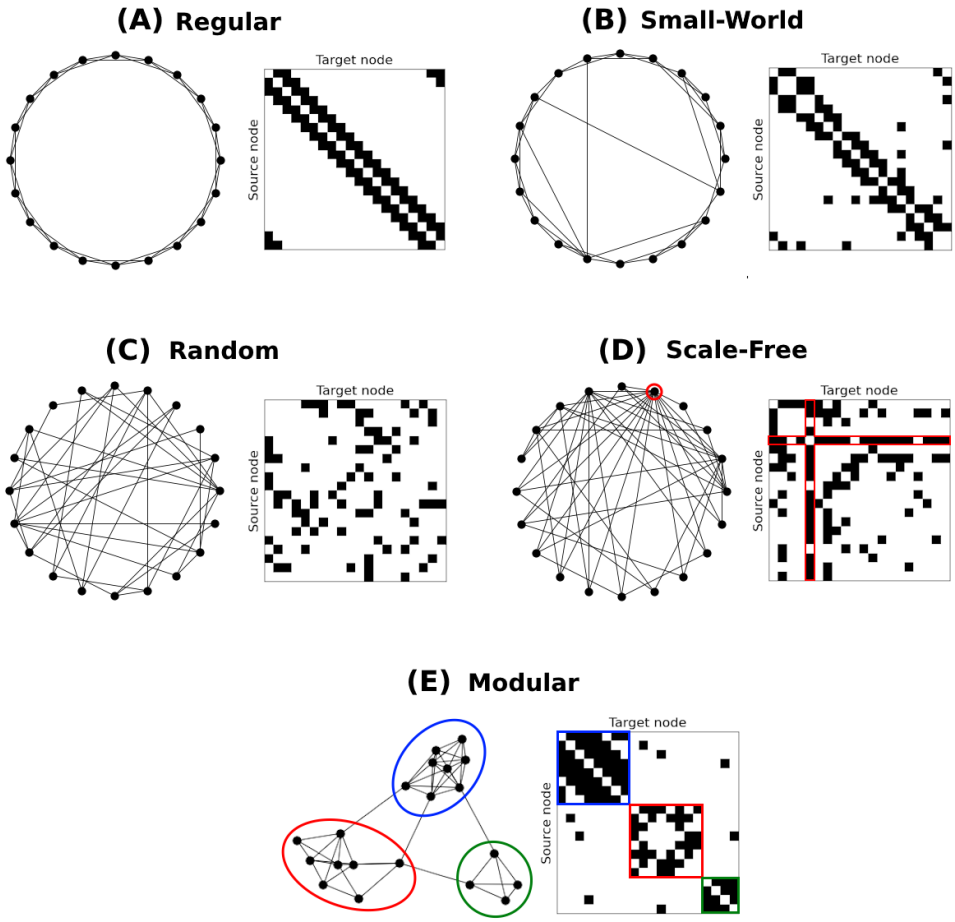

Figure I.4: **Graph representation and adjacency matrix of characteristic networks. (A)** Regular lattice network. All nodes have the exact same connectivity. **(B)** Small-World (SW) network exhibiting both high clustering and low mean shortest path length. **(C)** Random network typically exhibit low clustering and low shortest path length. **(D)** Scale-free (SF) network. The node highlighted in red is a hub of the network, with a significantly stronger connectivity than the other nodes. **(E)** Modular network. The different modules highlighted in blue, red and green, exhibit strong connectivity and few inter-connections.

Scale-free networks

In scale-free networks, the degree distribution of the nodes follows a power law. The probability $p(k)$ for a node to be of degree k is such that:

$$p(k) \propto k^{-\gamma}, \tag{I.11}$$

with $\gamma \in \mathbb{R}$. In other words, a small portion of the network nodes, called the network's hubs, exhibit a way higher degree. The Barabási-Albert model gives a procedure for the construction of scale-free networks (Barabási & Albert 1999), by starting with a small Fully-Connected network of m_0 nodes then adding one by one the $N - m_0$ remaining nodes, connecting them to the m already present nodes with probability

$$p_v = \frac{k_v}{\sum_w k_w}, \tag{I.12}$$

$w \in [\![0 : m - 1]\!]$. Scale-free networks exhibit nodes with degrees that are several standard deviations away from the average degree of the network. These highly connected nodes are called *hubs*. Note that, however, for smaller networks with size $N < 100$, the scale-free property might not be properly observable.

The relevance of *scale-freeness* in nature is still a debated topic. However, hub structures are important features of many real-world networks. In the brain, highly connected areas act as important pathways between different parts of the brain, at both structural (that is, linked by physical neuronal connections) and functional (that is, linked through activation patterns) levels (Broido & Clauset 2019; van den Heuvel & Sporns 2013).

Modular networks

Modular networks exhibit groups of nodes, called modules or communities, with very strong internal connections, and sparse inter-connections. Modularity is a key feature in mammal brains, whose architecture relies on various anatomical regions with dense intra-connections. Their communication with each others, following different patterns, ultimately give rise to brain function (Newman 2006; Meunier *et al.* 2010).

2.2 Brain imaging

A wide range of techniques are in use to map the brain's structure, and record cerebral activity. This section briefly introduces common imaging techniques which will be mentioned later in this thesis, but obviously does not claim to be exhaustive.

2.2.1 MRI, fMRI: Magnetic Resonance Imaging

MRI

Magnetic resonance imaging (MRI) is a widely used non-invasive tomography technique, including in brain imaging. It uses a magnetic field along which the hydrogen nuclei of the brain align, and radio frequency pulses to disrupt their orientation. It detects the signal emitted by the nuclei when returning to their baseline alignment. MRI thus builds images of the brain's anatomy, including veins and capillaries and white and gray matter (Naidich *et al.* 2013).

fMRI

Functional MRI (fMRI) uses MRI to capture and map activity patterns of the brain. Increased activity in brain areas is linked to an increased cerebral blood flow towards them. Red cells of the blood carry hemoglobin proteins, that can either bind or not to oxygen molecules, forming oxyhemoglobin (in contrast with deoxyhemoglobin). The oxygen consumption of active brain areas does not rise proportionally to the blood flow, leading to an excess of oxyhemoglobin in regions of stronger activity. fMRI utilizes the dia-(resp. para-)magnetic property of oxyhemoglobin (resp. deoxyhemoglobin), leading the hemoglobin proteins to align or not with the magnetic field. The resulting signals are called **blood oxygen level-dependent (BOLD) signals** (Lv *et al.* 2018).

2.2.2 EEG: Electrophysiological imaging

Electroencephalography (EEG) is a common non-invasive technique used to capture brain activity. It consists in a set of electrodes placed on the scalp, recording the electrical potential arising from the firing of surrounding neuronal populations (see. section I.1.2.1) (Chaddad *et al.* 2023). The applications of EEG are numerous, since it enables real-time brain monitoring, and is a relatively affordable and accessible system. In particular, it is commonly used for the diagnosis of epilepsy, from the identification of the epileptogenic zone to seizure spreading patterns through the brain (Mecarelli 2019).

2.2.3 STP: Serial two-photon tomography

Serial two-photon tomography (STP) is an ex-vivo technique used in neuroscience for the reconstruction of detailed neural maps of whole brains. It uses two-photon microscopy to capture fluorescence images of the tissue layer by layer, thus producing a high-resolution volumetric dataset (Amato *et al.* 2016).

2.3 Brain structure and function

The brain controls a large variety of functions, from simple tasks such as moving a finger and breathing to more complex cognitive functions such as thinking. This

behavior is enabled by the modular organization of the brain, with different brain areas involved in specific functions. However, brain function does not arise from the activation of individual areas, but rather from complex patterns of activation across the brain (Lynn & Bassett 2019; Sporns 2013).

2.3.1 The human brain and the mouse brain

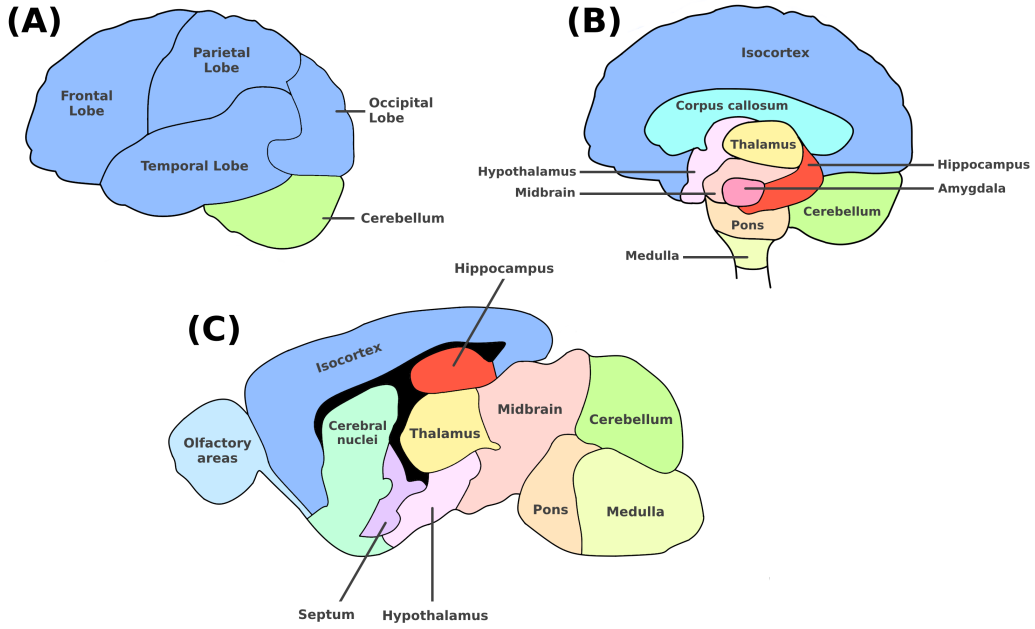

Figure I.5: **Overview of the principal local brain areas. (A)** The human brain cortex is divided into frontal, parietal, temporal and occipital lobes. **(B)** Slice view of the human brain, showing the inner brain structures. **(B)** Slice view of the mouse brain.

Figure I.5 provides an overview of the anatomical regions forming the human and the mouse brain (Oh *et al.* 2014; Ding *et al.* 2020). The cerebral cortex constitute the larger part of the human brain. It is divided into four lobes, each one containing brain areas involved in specific cognitive, motor and sensory functions. The frontal lobe contains brain areas responsible for motor function, but also for speech and complex cognitive functions such as thinking and decision making. The parietal lobe mostly controls somatosensory functions. The occipital lobe contains visual brain areas. Finally, the temporal lobe contains the auditory areas, as well as brain areas involved in language and memory. In the mouse brain, the cortical structures are way smaller, but are responsible for similar functions.

For both mice and humans, subcortical areas include the thalamus, the hypothalamus and the hippocampus, the latter being a common epileptogenic zone. The Hippocampal formation (HF) is composed of the Dentate Gyrus (DG), the Parahippocampal Gyrus, containing the Subiculum (SUB) and the Entorhinal Cor-

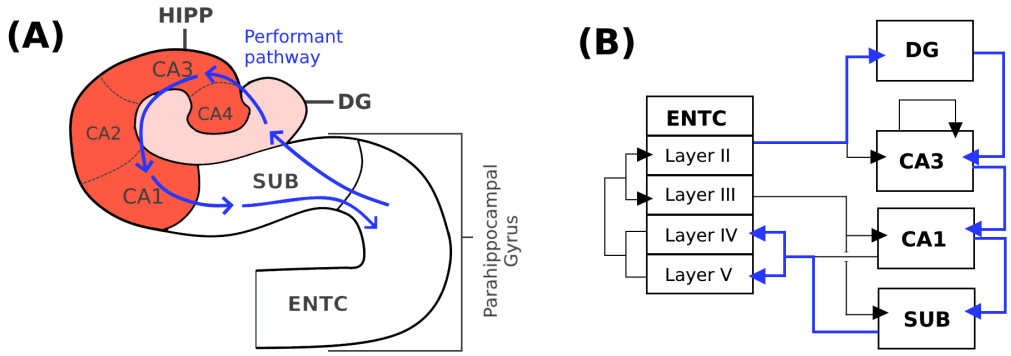

Figure I.6: **Overview of the Hippocampal formation.** **(A)** Anatomical overview of the Hippocampus. The blue arrows show the performant pathway through which the information navigate. **(B)** Circuit representation of the main connections in mice Hippocampal formation. The black arrows show the main connections between the different areas and neuron layers of the Entorhinal Cortex. The blue arrows show the performant pathway.

tex (ENTC), and the proper Hippocampus, composed of brain areas CA1, CA2, CA3 and CA4. The SUB forms a transition area between the six-neuron-layers composition of cortical areas and the three-layers composition of the Hippocampus. The ENTC acts as way in and out for information coming from the rest of the brain. Although the different areas share many intricate connections, the information mostly navigates through the Hippocampus via the *performant pathway* forming a loop connecting ENTC $\longrightarrow$ DG $\longrightarrow$ CA3 $\longrightarrow$ CA1 $\longrightarrow$ SUB $\longrightarrow$ ENTC, as shown on **Figure** I.6. Finally, the brainstem contains the midbrain, pons and medulla, and connects the brain to the spinal cord, enabling the communication with the rest of the body.

2.3.2 Large-scale brain networks: Structural Connectivity

The brain has a highly complex architecture. The multiple cortical and subcortical brain areas are composed of neuronal populations sharing intricate connections. **Connectomes** aim to describe the structure of the brain by mapping its axonal connections linking neurons and neuronal populations. Such mapping may describe the brain at different scales. Micro-scales networks describe brain structure at the level of individual neurons and synapses. However, the difficulty for mapping these fine-scale structures, and their precision, make them inadequate for the study of whole-brain phenomena. On the other hand, large-scale brain networks aim to map the long-range white-matter tracts between brain regions (Lynn & Bassett 2019; Sporns 2013).

Structural connectivity matrix

The structure of whole-brain networks consists of a set of nodes accounting for local brain areas, and a set of vertices accounting for the total connective strength linking the different brain areas. The structure is encapsulated within an adjacency matrix called the Structural Connectivity (SC) matrix. Other structural information might consists in a matrix of tract lengths containing the length of the neuronal projections between brain areas, and a list containing spatial information for each local brain area.

The Allen mouse brain atlas

The Allen mouse brain atlas is a well-known meso-scale connectome for mice, mapping both long-range and local connections. The Allen mouse brain aims to be representative of an average mouse brain (Oh *et al.* 2014). Connections were identified using anterograde tracing. Sites of stereotactic injection of the tracer were manually determined and indexed. The tracer was the adeno-associated virus (AAV1) expressing the green fluorescent protein (GFP). Using serial two-photon tomography, GFP signals were obtained and segmented into pixel grids. They enabled the identification of each injection site's axonal projections. The connective strength between a source and a target was then defined by the volume of segmented pixels in the target, normalized by the volume of segmented pixels of the injection site. A weight matrix can be obtained by averaging the strength of each connection over 1231 mice brains.

The Allen Mouse Brain SC derived in (Melozzi *et al.* 2017) contains the connective strengths between 98 brain regions, indexed from 1 to 98. **Figure** I.7 shows the SC weights in base-ten logarithmic scale for better visualisation. The Allen Institute neuroimaging analysis consistently involves source regions exclusively situated in the right hemisphere. The SC matrix used here the left hemisphere's counterpart constructed by mirroring the right hemisphere. Originally, the strength of connections between a given region and another was computed as the average across several experiments utilizing those specific brain areas as source and target region. The SC matrix is divided into four blocks, i.e., R-R, R-L, L-R, and L-L (in a clockwise order from the upper left), symmetries emerge where R-R equals L-L and R-L equals L-R. This assumption is grounded in the notable lateral symmetry observed in the mouse brain, as reported in (Calabrese *et al.* 2015).

2.3.3 Functional Connectivity

Beyond physical connections, the different brain areas are connected through patterns of activation. At rest or while performing tasks, the coherent firing of neuronal populations even in absence of direct structural connection constitutes a functional connection.

The Functional Connectivity (FC) matrix of the brain is obtained by calculating the temporal correlation between BOLD time-series recorded in each brain area

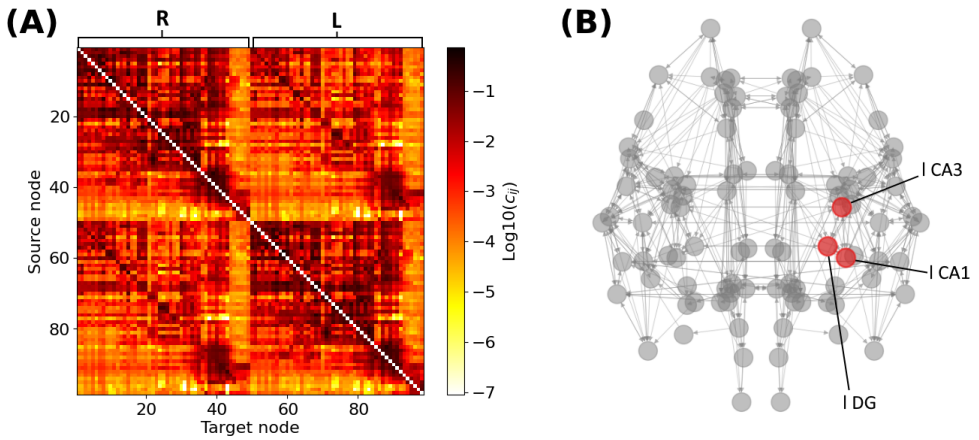

Figure I.7: **Structural connectivity matrix and mouse brain network. (A)** Allen Structural Connectivity matrix. The elements of the matrix show the logarithm of the weight for the connections between any pair of brain areas. Node indices ranging from 1 to 49 form the right hemisphere (R), node indices ranging from 50 to 98 form the left one (L). **(B)** Mouse brain network graph. Only connections of weight higher than 0.1 are shown for visibility reasons. The red nodes indicate the areas composing the left hippocampus. Note that the left brain hemisphere appears on the right hand side of our template.

at rest (Bastos & Schoffelen 2016). Let $(x_{i,t})$, $(x_{j,t})$ be the sampled time-series for brain areas i and j. Their Pearson correlation coefficient is defined as:

$$r_{ij} = \frac{\sum_t (x_{i,t} - \overline{x_i})(x_{j,t} - \overline{x_j})}{\sqrt{\sum_t (x_{i,t} - \overline{x_i})^2 \sum_t (x_{j,t} - \overline{x_j})^2}}, \tag{I.13}$$

with $\overline{x_i}$ the average value of the series over time. $r = 1$ denotes perfect coherence between the two time-series, while $r = -1$ denotes perfect anti-coherence and $r = 0$ shows the absence of coherence. The Functional Connectivity is encapsulated within the matrix $FC = (r_{ij})$. In practice, individual's FC is recorded using fMRI. Numerical models of FC can also be computed based on simulated time-series (see section I.4.1.3).

Resting-state functional networks

At rest, brain areas presenting important patterns of coherent activity form the Resting-State Networks (RSN) of the brain (Seitzman *et al.* 2019). In mammalian brains, well-known RSNs include for instance the Default Mode Network (DMN), but also specific tasks-related networks such as the visual or motor networks. The disruption of RSNs may be associated with neurological and psychiatric disorders. In Alzheimer's diseased patients, loss of connectivity was observed in the DMN, suggesting impaired processing of the information. In patients with multiple sclerosis, decreased functional connectivity of the primary motor network

was associated with deterioration in the white matter of the callosum area. Alteration of FC might therefore be a consequence of a disrupted brain structure (van den Heuvel & Hulshoff Pol 2010).

3 Non-linear dynamical systems

Studies and simulations of pathological and healthy brain dynamics rely on mathematical translations of complex phenomena. In this section, we give a brief summary of the important mathematical concepts of non-linear dynamical systems.

3.1 Dynamical systems: an overview

Dynamical systems theory aims to describe the behavior of complex systems, see e.g. (Strogatz 2018; Corinto & Torcini 2019; Ott 2002). From well-known physical systems to more abstracts models for economical markets or human behaviors, complex systems have applications in a wide range of areas.

3.1.1 Mathematical formalism

Let X be a set of any dimension. A dynamical system is described by a transformation (Gros 2024):

$$f : X \longrightarrow X, \tag{I.14}$$

where X is the set of the possible states of the system, called the phase space. With discrete time, the function $\mathbf{f}$ defines the system's new state at each iteration. An initial state of the system $\mathbf{x}_0$ is called the initial conditions. After n iterations (ie., after i time steps), the state of the system is defined by:

$$\mathbf{x}_i = \mathbf{f}^i(\mathbf{x}_0). \tag{I.15}$$

Identically, with continuous time and within a N-dimensional phase space $\mathbb{R}^N$, the system is described by a set of differential equations:

$$\dot{\mathbf{x}}(t) = \frac{d\mathbf{x}(t)}{dt} = \mathbf{f}(\mathbf{x}(t)) \tag{I.16}$$

where $\mathbf{x}$ is in $\mathbb{R}^N$. More explicitly, $\mathbf{x} = (x_1, x_2, \ldots, x_N)$, and $\mathbf{f} = (f_1, f_2, \ldots, f_N)$, and for all i in $[\![1 : N]\!]$, $x_n \in \mathbb{R}$ and $f_i \in \{f : \mathbb{R}^N \longrightarrow \mathbb{R}\}$. Equation I.16 then results in a set of differential equations:

$$\begin{cases} \dot{x}_1(t) & = f_1(x_1(t), x_2(t), \ldots, x_N(t)) \\ \dot{x}_2(t) & = f_2(x_2(t), x_2(t), \ldots, x_N(t)) \\ & \vdots \\ \dot{x}_N(t) & = f_N(x_N(t), x_2(t), \ldots, x_N(t)). \end{cases} \tag{I.17}$$

In the phase space, a given solution $\boldsymbol{x}(t)$ defines a system's trajectory.

3.1.2 Non-linear systems

The dynamics of linear dynamical systems can be expressed through linear evolution functions. In other words, the coupling of the one-dimensional differential equations

results from a matrix $\boldsymbol{A}$ in $\mathbb{R}^{N\times N}$ such that:

$$\dot{\mathbf{x}}(t) = \boldsymbol{A}\mathbf{x}(t), \tag{I.18}$$

or explicitly:

$$\begin{cases} \dot{x}_1(t) & = a_{1,1}\cdot x_1(t) + a_{1,2}\cdot x_2(t) + \ldots + a_{1,N}\cdot x_N(t) \\ \dot{x}_2(t) & = a_{2,1}\cdot x_1(t) + a_{2,2}\cdot x_2(t) + \ldots + a_{2,N}\cdot x_N(t) \\ & \vdots \\ \dot{x}_N(t) & = a_{N,1}\cdot x_1(t) + a_{N,2}\cdot x_2(t) + \ldots + a_{N,N}\cdot x_N(t). \end{cases} \tag{I.19}$$

Non-linear systems on the other hand refer to all dynamical systems that can not be expressed through linear functions. Non-linearity is a very important feature of dynamical systems, that can give rise to a large repertoire of behaviors. High sensitivity to parameter variation, initial conditions and external inputs may result in drastic shifts in the dynamics under very small perturbations.

3.2 Stability and attractors

State bifurcation characterizes systems whose behavior changes, either spontaneously or consequently to external causes. The mathematical formalism underlying bifurcation includes a description of the system's different *behaviors* in the form of attractors guiding the system towards one state or another.

3.2.1 Mathematical formalism

Different regions of the phase space may tend to attract or repel the trajectory of a system. Let us consider the N-dimensional system as described in equation I.17. In the phase space, the trajectory of any of the N solutions $\dot{x}_i(t) = 0$, $i \in [\![1 : N]\!]$ defines a curve of equilibrium along the i^{th} dimension. The intersection of the N nullclines defines a **Fixed-Point (FP)** at which the time derivative of $x_i(t)$ is zero, that is:

$$f_i(\mathbf{x}^*) = \mathbf{0} \tag{I.20}$$

ie., the system is not evolving and is in an equilibrium state.

The analytical assessment of the stability of a FP requires the linearization of the equation of motion in its close neighbouring region. With δx_i an infinitesimal variation of the FP along the i^{th} dimension:

$$x_i(t) = x_i^*(t) + \delta x_i. \tag{I.21}$$

Using the Taylor theorem, the flux of the system around the FP is defined as:

$$\begin{cases} \dot{x}_1(t) & \approx (\frac{\partial f_1}{\partial x_1} + \frac{\partial f_1}{\partial x_2} + \ldots + \frac{\partial f_1}{\partial x_N})\big|_{\boldsymbol{x}=\boldsymbol{x}^*}\delta x_1 \\ \dot{x}_2(t) & \approx (\frac{\partial f_2}{\partial x_1} + \frac{\partial f_2}{\partial x_2} + \ldots + \frac{\partial f_2}{\partial x_N})\big|_{\boldsymbol{x}=\boldsymbol{x}^*}\delta x_2 \\ \vdots & \\ \dot{x}_N(t) & \approx (\frac{\partial f_N}{\partial x_1} + \frac{\partial f_N}{\partial x_2} + \ldots + \frac{\partial f_N}{\partial x_N})\big|_{\boldsymbol{x}=\boldsymbol{x}^*}\delta x_N, \end{cases} \tag{I.22}$$

or more concisely:

$$\dot{\mathbf{x}}(t) = \frac{d}{dt}\delta\mathbf{x} \approx \boldsymbol{J}\delta\mathbf{x} \tag{I.23}$$

where:

$$\boldsymbol{J} = \begin{bmatrix} \frac{\partial f_1}{\partial x_1}\big|_{\boldsymbol{x}=\boldsymbol{x}^*} & \frac{\partial f_1}{\partial x_2}\big|_{\boldsymbol{x}=\boldsymbol{x}^*} & \cdots\cdots & \frac{\partial f_1}{\partial x_N}\big|_{\boldsymbol{x}=\boldsymbol{x}^*} \\ \frac{\partial f_2}{\partial x_1}\big|_{\boldsymbol{x}=\boldsymbol{x}^*} & \frac{\partial f_2}{\partial x_2}\big|_{\boldsymbol{x}=\boldsymbol{x}^*} & \cdots\cdots & \frac{\partial f_2}{\partial x_N}\big|_{\boldsymbol{x}=\boldsymbol{x}^*} \\ \vdots & & & \\ \frac{\partial f_N}{\partial x_1}\big|_{\boldsymbol{x}=\boldsymbol{x}^*} & \frac{\partial f_N}{\partial x_2}\big|_{\boldsymbol{x}=\boldsymbol{x}^*} & \cdots\cdots & \frac{\partial f_N}{\partial x_N}\big|_{\boldsymbol{x}=\boldsymbol{x}^*} \end{bmatrix} \tag{I.24}$$

is the Jacobian matrix of the system, evaluated at the FP. The Jacobian matrix thus determines the direction and form of the flow near the system's equilibrium.

The Jacobian matrix comes with a set of eigenvalues $\{\lambda_i\}$ and their associated eigenvectors $\{\mathbf{e}_i\}$, such that $\boldsymbol{J}\mathbf{e}_i = \lambda_i\mathbf{e}_i$ for all i in $[\![1 : N]\!]$. Along each dimension i, equation I.23 therefore is:

$$\frac{d}{dt}\delta\mathbf{x}\mathbf{e}_i = \boldsymbol{J}\mathbf{e}_i\delta\mathbf{x} \tag{I.25}$$

$$\text{i.e.} \quad \frac{d}{dt}\delta x_i = \lambda_i x_i, \tag{I.26}$$

and therefore the evolution around $\boldsymbol{x}^*$ around the i^{th} eigendirection takes the form:

$$\delta x_i = e^{\lambda_i t}. \tag{I.27}$$

The set of eigenvalues form the system's spectrum of *Lyapunov exponents*. Near the FP, a positive real part of the Lyapunov exponent $\mathrm{Re}(\lambda_i) > 0$ causes the infinitesimal perturbation δx_i to grow exponentially, while a negative value $\mathrm{Re}(\lambda_i) < 0$ causes exponential decay of the perturbation, attracting the trajectory towards the system. The corresponding trajectories $x_i(t)$ form the stable (when $\mathrm{Re}(\lambda_i) < 0$) and unstable (when $\mathrm{Re}(\lambda_i) > 0$) manifolds of the system.

3.2.2 Stable and unstable attractors

When all Lyapunov exponents of a Jacobian matrix at a FP are positive, then the FP rejects the system's trajectory and is said to be an **unstable node**. When all exponents are negative, the FP attracts the trajectory, causing the system to reach and remain on a steady state. In that case, the FP is said to be a **stable node**

(Ott 2002; Crawford 1991).

In a bi-dimensional system, common types of unstable FP include **saddle nodes (SN)**, when $\mathrm{Re}(\lambda_1) > 0$ and $\mathrm{Re}(\lambda_2) < 0$, at which the trajectory is attracted towards the FP along one eigendirection, and rejected along the other. Other common types of attractors include **limit cycles**, or periodic orbits, that is, closed manifolds of the phase space. Periodic orbits may be stable, when they attract trajectories from inside and outside the cycle, unstable, when they repel these trajectories, saddle, when the attract one and repel the other, or have more complex stability patterns. Periodic orbits therefore play a key role for the modelization of oscillatory behaviors.

Nodes and periodic orbits are rather simple types of attractors, however high dimension systems may present more complex ones. In particular, *strange attractors* can generate chaotic behaviors. The presence of noise or external stimuli may also disrupt the system's stability, generating unpredictable dynamics.

3.2.3 Visualization of the dynamics: phase portraits

To visualize the dynamics of a system, one draws its flux, trajectories and attractors on its parameter space (see **Figure** I.8). Conventionally, stable FP are represented by full circles, and unstable FP by empty circles. Manifolds follow the directions of the Jacobian eigenvectors. They may be straight lines, in the case of real Lyapunov exponents, or curves when the exponents contain a non-null imaginary part. In the phase portrait, no trajectory can ever cross a manifold. To indicate the direction and intensity of the flow on the phase space, the vector field shows the gradient of the system's flow.

3.3 Bifurcations

In parameter-dependent dynamical equations:

$$\dot{\mathbf{x}}(t) = \mathbf{f}(\mathbf{x}(t), \boldsymbol{\mu}) \tag{I.28}$$

with $\boldsymbol{\mu} \in \mathbb{R}^N$, variations of a the control parameter $\boldsymbol{\mu}$ passed a critical point $\boldsymbol{\mu}_c$ may modify the form of the solutions for the dynamical equations. Attractors may appear, disappear, collide or interact in a more complex fashion. Bifurcation refers to the transition from one set of attractors to another one (Crawford 1991).

3.3.1 Visualization of bifurcations: bifurcation diagrams

Bifurcation diagrams represent the system's attractors by showing their position in the phase space as a function of the control parameter. Conventionally, stable equilibrium positions are represented by a full line, unstable equilibrium positions by a dashed line. **Figure** I.9 shows a example of a bifurcation diagram.

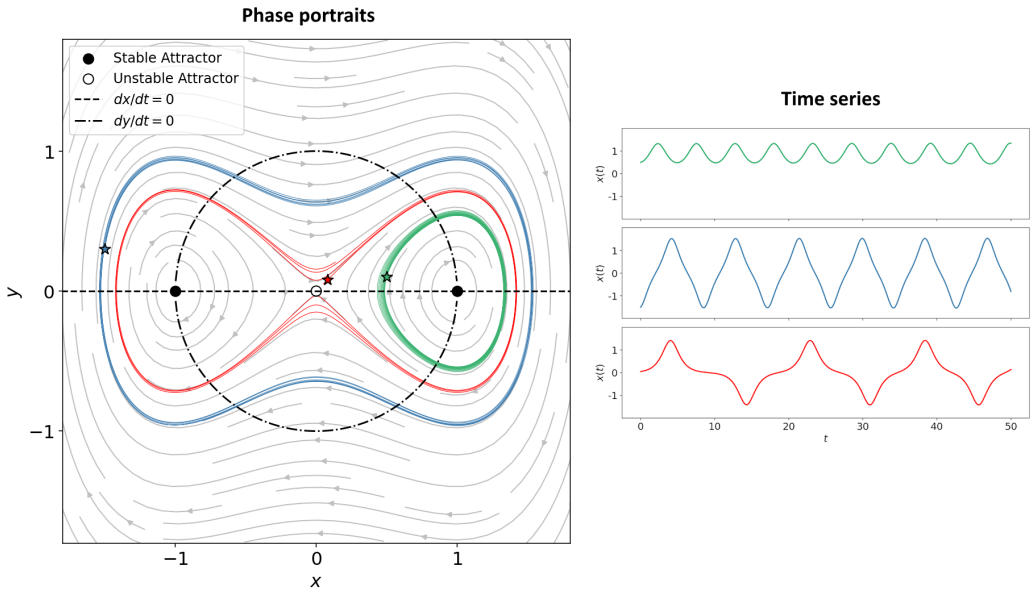

Figure I.8: **Phase portrait representation of a dynamical system.** Dynamical features are shown on the phase plane (x, y). Dashed lines show the system's nullclines. Full (resp. empty) circles represent stable (resp. unstable) attractors. Namely, the system exhibits one saddle-node and two limit cycles. A vector field shows the flow of the dynamics. Star markers show the initial position of three trajectories. The blue, red and green trajectories are shown both as phase portraits and as time series. Note that on the phase plane, the red trajectory is close to the system's manifold.

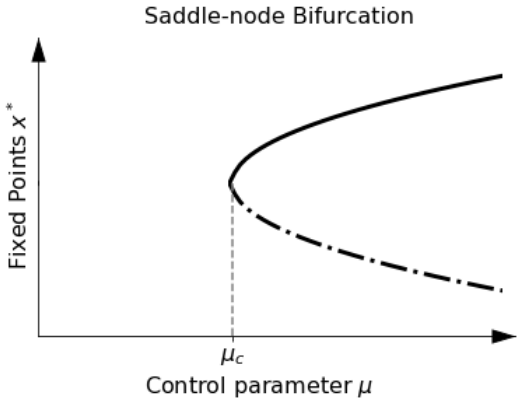

Figure I.9: **Bifurcation diagram of a Saddle-node (SN) bifurcation.** The dashed line represents an unstable fixed-point (FP). The full line represents a stable FP. The bifurcation occurs when the value of the control parameter reaches its critical value $\mu > \mu_c$. Before the bifurcation, the system is free of attractor. After the bifurcation, the system exhibits both stable and unstable FP.

3.3.2 Common types of bifurcation

This section presents an overview of common bifurcations. Local bifurcations are illustrated by their *normal form*, i.e. simple dynamical equations exhibiting the bifurcation.

- **Saddle-Node (SN)** bifurcation occurs when a stable node and an unstable node collide into a saddle-node past the critical value of the control parameter, then leaving the system free of attractors (see **Figure** I.10 **(A)**). **Saddle-node on in invariant circle (SNIC)** bifurcation occurs when both nodes lie on a same closed manifold. In that case, their collision results in the creation of a periodic orbit instead of a saddle-node (see **Figure** I.10 **(B)**). The normal form of SN bifurcation is the one dimensional equation:

$$\dot{x}(t) = \mu - x^2(t), \tag{I.29}$$

with $x(t) \in \mathbb{R}, \mu \in \mathbb{R}$. Therefore:

$$\begin{cases} \text{For } \mu > 0, \text{ the system has two FP } x^*_\pm = \pm\sqrt{\mu} \\ \text{For } \mu = 0, \text{ the system has one FP } x^* = 0 \\ \text{For } \mu < 0, \text{ the system has no FP.} \end{cases}$$

In one-dimensional systems, the FP stability is simply given by the sign of the flow $\dot{x}(t)$ from each side. In the present case, when $\mu > 0$:

$$\dot{x}(t) \begin{cases} < 0 \text{ for } x < x^*_- \\ > 0 \text{ for } x \in [x^*_-, x^*_+] \\ < 0 \text{ for } x > x^*_+, \end{cases} \tag{I.30}$$

and when $\mu = 0$:

$$\dot{x}(t) \begin{cases} < 0 \text{ for } x < x^* \\ > 0 \text{ for } x > x^*. \end{cases} \tag{I.31}$$

Therefore x^*_- is unstable, x^*_+ is stable and x^* is a saddle node.

- **Homoclinic bifurcation (HB)** results from the collision of a saddle-node with a growing periodic orbit. As the periodic orbit grows, its trajectory approaches the SN, until reaching it and colliding into a single limit cycle. Finally, the limit cycle disappears (see **Figure** I.10 **(C)**).

3.3.3 Network dynamics

Dynamical equations, rather than only describing isolated systems, may incorporate coupling functions binding the dynamics of multiple subsystems. The embedding of dynamical subsystems within a network structure may cause the emergence of

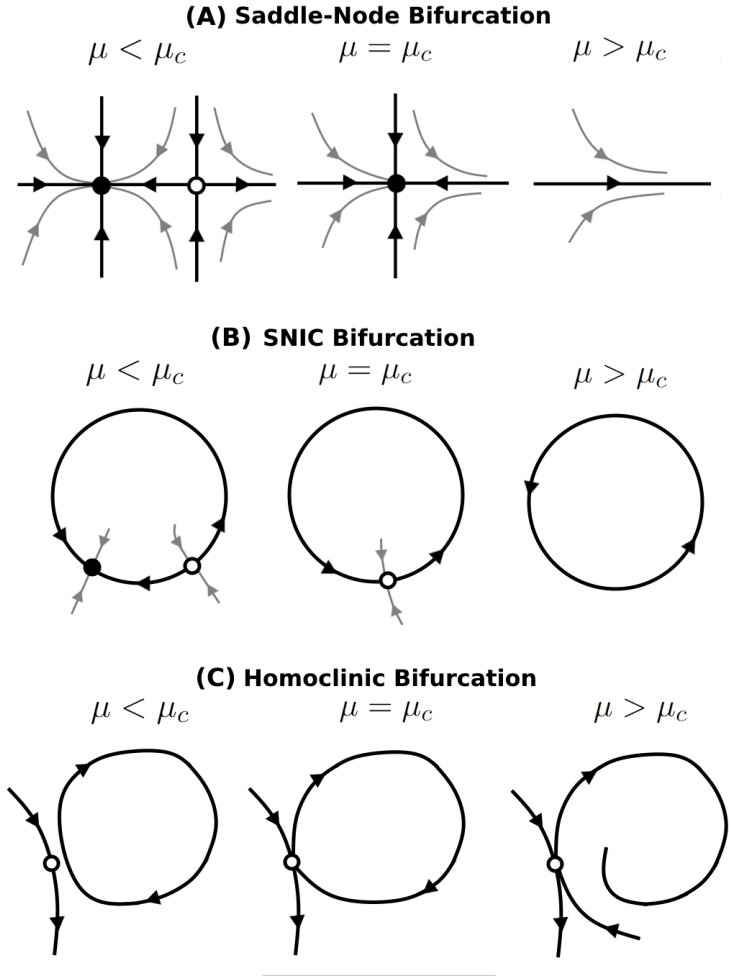

Figure I.10: **Representation of bifurcations. (A)** Saddle-Node (SN) bifurcation. Before the bifurcation, the system exhibits a stable FP and a saddle-node. Both attractors collide at the bifurcation, ultimately leaving the system free of attractors. **(B)** Saddle-Node on invariant circle (SNIC) bifurcation. Before the bifurcation, the system exhibits a stable FP and a saddle-node, both located on the trajectory of a limit circle. Both nodes collide at the bifurcation. The system is left with a limit circle. **(C)** Homoclinic bifurcation. Before the bifurcation, the system exhibits an saddle-node and a limit circle. The orbit of the limit circle grows with the control parameter. Both attractors collide at the bifurcation, and the system is left with a unique saddle-node.

unique dynamical features. The dynamics of the network may for example exhibit specific information diffusion patterns. The individual subsystems' activities may also vary coherently. In groups of animals, interactions of individuals underlie collective motion behaviors (Gómez-Nava *et al.* 2022; Heffern *et al.* 2021). In our body, cognitive, motor or sensory functions emerge from the coherent activity of distinct brain areas (Chialvo 2010).

4 Models of healthy and epileptic brain activity

In this section, we present three models of brain dynamics. These models describe the complex neural phenomena mentioned in section I.1, within the mathematical framework introduced in sections I.2, I.3. We discuss a model for resting state dynamics, as well as two models for seizure dynamics at macro and micro scales.

4.1 The Wong-Wang model

The Wong-Wang model (Wang 2002) was developed to model a visual discrimination task with two alternatives, namely, looking left or looking right. The model takes as its basis cognitive studies of monkeys, where the monkeys' reaction time was correlated with the ramping of spiking activity in the lateral intraparietal cortex (LIP).

4.1.1 Reduced set of dynamical equations

The more straightforward model for neuronal populations would consist in a set of equations describing each neuron's membrane potential. A single neuron, equipped with excitatory AMPA and NMDA receptors and inhibitory GABA-A receptors, is described by a leaky integrate and fire (LIF) model:

$$\begin{aligned} C_m \frac{dV_i(t)}{dt} &= -g_m(V_i(t) - V_L) \\ &\quad - g_{AMPA,ext}(V_i(t) - V_E) s^{AMPA,ext}(t) \\ &\quad - g_{AMPA,rec}(V_i(t) - V_E) \sum_{j=1}^{N_E} w_{ij} s_j^{AMPA,rec}(t) \\ &\quad - g_{NMDA} \frac{V_i(t) - V_E}{1 + \lambda e^{-\beta V_i(t)}} \sum_{j=1}^{N_E} w_{ij} s_j^{NMDA}(t) \\ &\quad - g_{GABA}(V_i(t) - V_I) \sum_{j=1}^{N_I} w_{ij} s_j^{GABA}(t), \end{aligned} \tag{I.32}$$

with C_m the membrane capacitance, g_m the leak conductance, and V_L the resting potential of the cell. The conductances and populations labelled $AMPA, ext$, $AMPA, rec$, and $NMDA$ describe external excitatory inputs, recurrent excitatory inputs and excitatory inputs exhibiting voltage-dependent gating, respectively. Finally, g_{GABA} and s_{GABA} parametrize the inhibitory inputs. V_I, V_E are the inhibitory and excitatory reversal potentials, respectively.

The Wong-Wang model consists of four neuronal populations interacting with each others: one inhibitory, one non-selective excitatory, and two selective excitatory populations, labeled 1 and 2, accounting for the two alternative solutions for the

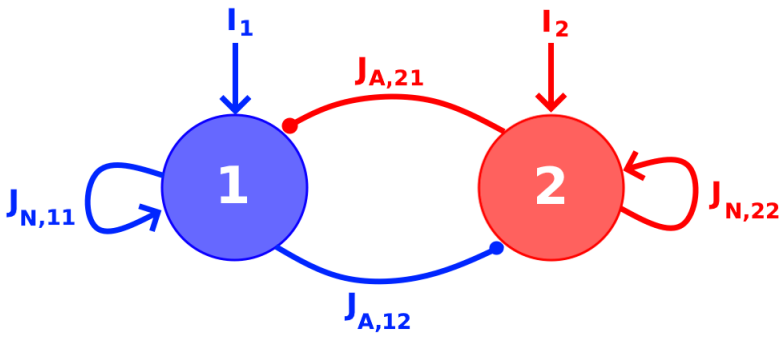

Figure I.11: **Schema of the reduced Wong-Wang model.** Two populations of excitatory neurons communicate via NMDA and AMPA coupling (J_A, J_N respectively). The two populations receive inputs from inhibitory neurons.

discrimination task. The reduced model (Wong & Wang 2006) uses the mean-field (MF) approach along with further reductions to obtain a set of only two differential equations. In a large homogeneous neuronal population, the collective influence of all individual components is approximated by a single averaged field. This approximation replaces the complex, high-dimensional interactions with a simplified effective field, allowing for a more tractable analysis of the system's macroscopic behavior.

Synaptic currents are assumed to be constant, and the contribution of recurrent connections to the dynamics of the membrane potentials is assumed to be minimal. Further reductions include the assumption that the activity of the non-selective neurons is constant, and that the dynamics of AMPA and GABA receptors are negligible compared to the slow dynamics of NMDA receptors. Finally, the system resumes in a set a two equations for the dynamics of the NMDA synaptic gating variables S of each selective excitatory population:

$$\frac{dS_i}{dt} = -\frac{S_i}{\tau_s} + (1 - S_i)\gamma H(x_i), \tag{I.33}$$

$$H(x_i) = \frac{ax_i - b}{1 - \exp(-d(ax_i - b)}, \tag{I.34}$$

where

$$x_1 = J_{N,11}S_1 - J_{N,21}S_2 + I_1 + I_0 + I_{noise,1} \tag{I.35}$$

$$x_2 = J_{N,22}S_2 - J_{N,12}S_1 + I_2 + I_0 + I_{noise,2}. \tag{I.36}$$

$H(x_i)$ is the average firing rate of population i, $J_{N,ij}$ (resp. $J_{A,ij}$) is the coupling constant from population i to j mediated by NMDA (resp. AMPA). I_0 accounts for the mean external inputs, and I_1 and I_2 represent visual stimuli.

4.1.2 Biased and unbiased stimulus dynamics

The stimuli received by the two selective neuronal populations of LIP cortex from Middle Temporal area encode visual motions. They are expressed through:

$$I_1 = J_{A,ext}\mu_0(1 + \frac{c'}{100}) \tag{I.37}$$

$$I_2 = J_{A,ext}\mu_0(1 - \frac{c'}{100}), \tag{I.38}$$

with μ_0 the stimulus strength, and c' the percentage coherence. c' is an important feature in the model for visual discrimination task, for it contains potential bias in the monkey's field of vision. Briefly, any movement occuring on its left will make the subject more likely to look on the left.

The intersection of the two nullclines $\frac{dS_1}{dt} = 0$ and $\frac{dS_2}{dt} = 0$ infers on the system's attractors. The phase space (r_1, r_2) of mean firing rates are expected to be similar to the phase space (S_1, S_2). In the absence of any stimulus, the system exhibits two unstable and three stable FP. The trajectory either reaches the spontaneous state where the firing rate of both populations remains low, or one of the two mnemonic persistent states where one of the populations produce self-sustained spiking activity (Wong & Wang 2006).

Unbiased system

With $c' = 0$, the system is not biased and only exhibits one saddle-node and two stable FP, corresponding to the two mnemonic persistant states. The two basins of attraction therefore leads the trajectory on either of the two steady state where one population exhibits high spiking activity, see **Figure** I.12.

Biased system

When increasing the coherence percentage, the phase space of the system looses its symmetry, with one basin of attraction larger than the other. At high values c', the SN collides with one stable FP, so that the system is left with a single attractor, see **Figure** I.13.

4.1.3 The reduced Wong-Wang model for resting state

In (Deco *et al.* 2013), the authors used the Wong-Wang model described above to study the resting-state functional connectivity of brain networks. Local brain areas are modelled with one Wong-Wang system and embedded within a large-scale network. The mean firing rate $H(x_i)$ and mean synaptic gating variable of area i are

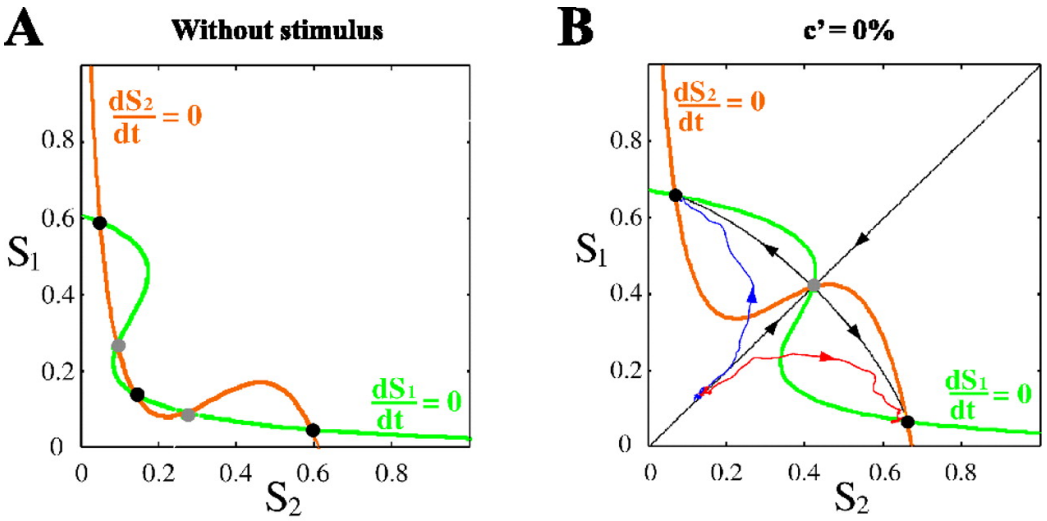

Figure I.12: **Random choice with stimulus at zero coherence.** **(A)** Phase-plane without stimulus. Black circles, Stable steady states (attractors); gray circles, saddle-type unstable steady states. The green and orange lines are the nullclines for the synaptic dynamical variables S1 and S2. **(B)** With an unbiased stimulus of 30 Hz, the two unstable steady states together with the low stable steady state disappear, and a new symmetric unstable steady state is formed. The black line with arrows toward (away) from the saddle point is the stable (unstable) manifold of this saddle point. The stable manifold is exactly the boundary between the two basins of attraction of the two choice attractors (when there is no noise). Superimposed are two typical single-trial trajectories (blue and red lines) of the state of the system from simulations. **From:** Wong, K., Wang, X. (2006) *A Recurrent Network Mechanism of Time Integration in Perceptual Decisions.* Journal of Neuroscience, 26 (4)1314-1328; DOI: 10.1523/JNEUROSCI.3733-05.2006. Licensed under CC BY 4.0.

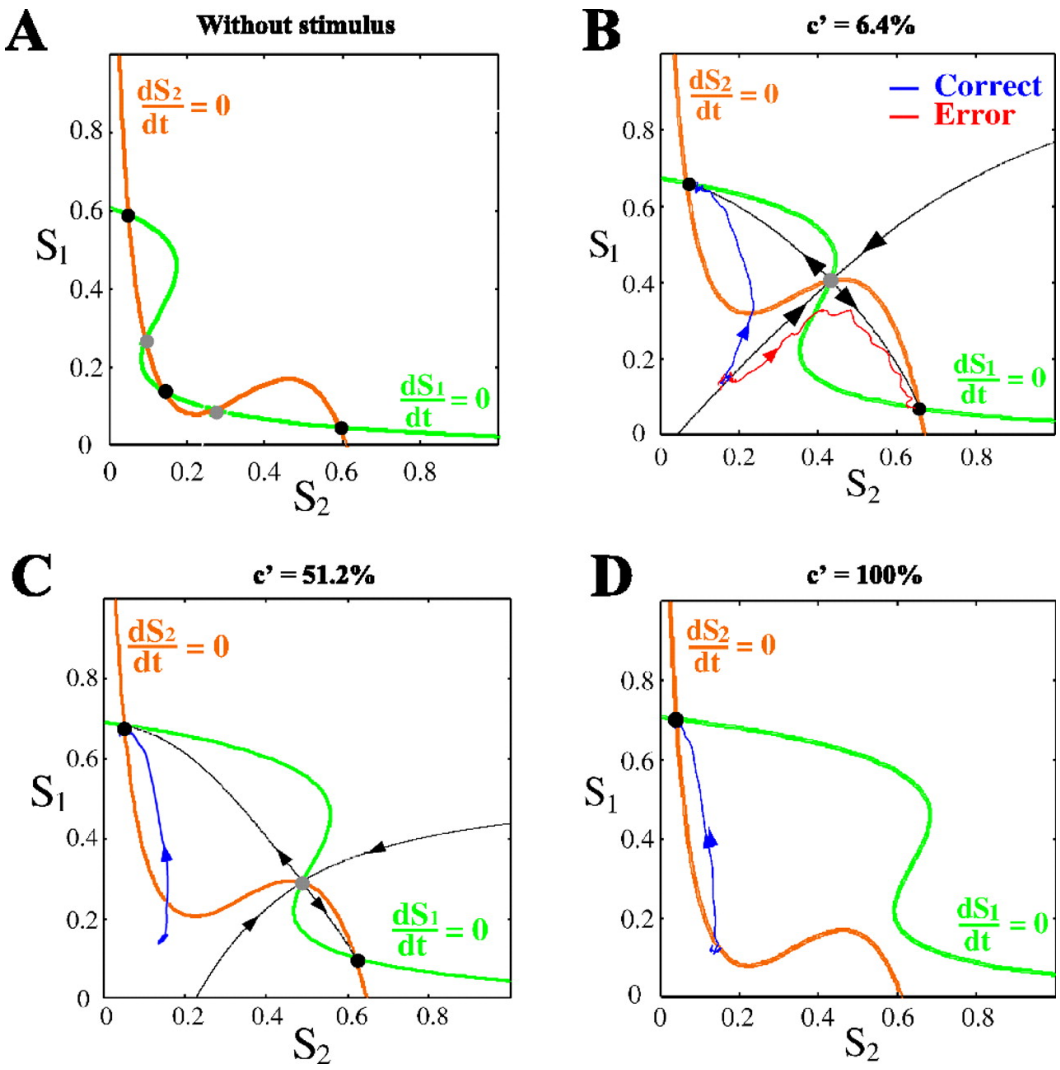

Figure I.13: **Basins of attraction with stimulus at nonzero coherence** ($c' > 0\%$)**. (A)** Phase-plane without stimulus. **(B)** The stable manifold is tilted away from the spontaneous state and toward the less favored attractor when c' is nonzero (6.4%). As a result, at the onset of stimulus, the system starts in a resting state that has a higher chance of falling in the basin of attraction of the favored attractor state. The blue and red lines are typical single-trial trajectories for correct and error choices, respectively. **(C)** Stronger bias between the basins of the two competing attractor states with a larger c' (51.2%). **(D)** When c' is sufficiently large, the saddle steady state annihilates with the less favored attractor, leaving only one choice attractor $c' = 100\%$. **From:** Wong, K., Wang, X. (2006) *A Recurrent Network Mechanism of Time Integration in Perceptual Decisions.* Journal of Neuroscience, 26 (4)1314-1328; DOI: 10.1523/JNEUROSCI.3733-05.2006. Licensed under CC BY 4.0.

described by:

$$\frac{dS_i}{dt} = -\frac{S_i}{\tau_s} + (1 - S_i)\gamma H(x_i) + \sigma\nu_i(t) \tag{I.39}$$

$$H(x_i) = \frac{ax_i - b}{1 - \exp(-d(ax_i - b))} \tag{I.40}$$

$$x_i = wJ_N S_i + GJ_N \sum_j c_{ij} S_j + I_0, \tag{I.41}$$

with w the local excitatory recurrence, c_{ij} the strength of the structural connection from local area i to j, and G a global coupling strength. J_N is the synaptic coupling of NMDA receptors, I_0 the external input. The kinetic parameters are τ_s and γ. The parameters for the input-output function H are a, b and d. $\nu_i(t)$ denodes Gaussian white noise with amplitude σ. Depending on the tuning of G, the system exhibits a multistable regime, with both high-activity and low-activity steady states.

Reproduction of FC matrices

To produce simulated FC matrices, the synaptic activity time-series are converted into simulated BOLD signals, using the Balloon-Windkessel hemodynamic model as decribed in (Friston *et al.* 2000; Friston *et al.* 2003). The Balloon-Windkessel model describes how neuronal activity in the brain triggers a cascade of physiological responses, utlimately leading to observable BOLD signals in fMRI. Synaptic activity increases vasodilation, which in turn affects blood flow and the volume of blood in the brain region, as well as the quantity of deoxyhemoglobin. This is captured by a series of differential equations that model blood volume, deoxygenation, and blood flow dynamics. The resulting changes in blood oxygenation and volume are then translated into a BOLD signal.

4.2 The Epileptor model

While biological-based models explain phenomena by focusing on underlying biological mechanisms, aiming to understand how systems function at a mechanistic level, phenomenological models focus on describing observed patterns and behaviors without delving into the biological details. In (Jirsa *et al.* 2014), the authors identify the main dynamical features of epileptic seizure, then develop the Epileptor model, a phenomenological model for seizure dynamics.

4.2.1 The common patterns of seizure dynamics: coupling fast and slow subsystems

In-vivo EEG recordings of epileptic patients as well as in-vitro models of epilepsy in mice and zebrafish exhibit common activity patterns during seizures. Bursting, composed of an alternation of silent and active periods during which fast discharges are

produced, operate on a short time scale. Spike and wave events (SWE), characteristic of excitable systems, produce large amplitude spikes followed by slow refractory periods, operate on a longer time scale.

Dynamical systems may exhibit a large variety of bursts, classified according to the type of bifurcation leading from equilibrium to oscillations (either SN, SNIC, supercritical Hopf or subcritical Hopf bifurcations), and the type of bifurcation leading from oscillations to equilibrium (either SNIC, homoclinic, supercritical Hopf or fold cycle bifurcations). Each bifurcation comes with specific patterns of variation of the frequency and amplitude of the discharges. In the recordings of in-vitro and in-vivo epileptic seizures, the abrupt apparition of discharges with a shift in DC currents indicates the presence of SN bifurcation at seizure onset. At seizure offset, the logarithmic scaling of the interspike interval approaching bifurcation, and the shift of DC currents, indicate the presence of a homoclinic bifurcation.

The general activity patterns of seizures identified experimentally are reproduced in the phenomenological Epileptor model by coupling subsystems operating at distinct time scales:

- A model of bursting mimics the fast discharges, using two state variables (x_1, y_1).

- A model of spiking neuron mimics the relatively slow SWE, using two state variables (x_2, y_2).

- A unique state variable z, called slow permittivity, is used to couple the fast and slow subsystems (x_1, y_1) and (x_2, y_2). The dynamics of z is way slower than the one of any other state variable and its evolution guides the system through state bifurcations. Although z does not have any biological meaning, its process accounts for slow processes in the brain, such as extracellular ionic concentrations or extracellular ATP concentration.

In addition, coupling functions $f_1(x_1, x_2)$ and $f_2(x_1, x_2)$ are used to manage the possible embedding of bursts and SWE.

$$\dot{x}_1 = y_1 - f_1(x_1, x_2) - z + I_1, \tag{I.42}$$

$$\dot{y}_1 = 1 - 5x_1^2 - y_1, \tag{I.43}$$

$$\dot{z} = \begin{cases} r(4(x_1 - x_0) - z - 0.1z^7) & \text{if } z < 0, \\ r(4(x_1 - x_0) - z) & \text{if } z \geq 0, \end{cases} \tag{I.44}$$

$$\dot{x}_2 = -y_2 + x_2 - x_2^3 + I_2 + 0.002g(x_1) - 0.3(z - 3.5), \tag{I.45}$$

$$\dot{y}_2 = \frac{1}{\tau}(-y_2 + f_2(x_2)), \tag{I.46}$$

$$\dot{g}(x_1) = -0.01(g - 0.1x_1), \tag{I.47}$$

where

$$f_1(x_1, x_2) = \begin{cases} 3x_1^3 - x_1^2 & \text{if } x_1 < 0, \\ (x_2 - 0.6(z-4)^2)x_1 & \text{if } x_1 \geq 0, \end{cases} \tag{I.48}$$

and

$$f_2(x_2) = \begin{cases} 0 & \text{if } x_2 < -0.25, \\ 6(x_2 + 0.25) & \text{if } x_2 \geq -0.25. \end{cases} \tag{I.49}$$

Gaussian white noise may be added to equations (I.45) and (I.46) to act as a physiological seizure trigger. $x_2 - x_1$ mimics the evolution of the potential of the brain area during rest and epileptic seizures. For this thesis, following the work of (Melozzi *et al.* 2017), the parameters of the system are set at $I_1 = 3.1$, $I_2 = 0.45$, $r = 3.5.10^{-4}$, $\tau = 10$ s. Additive Gaussian white noise has standard deviation $\sigma = 0.0025$.

4.2.2 Tuning the system's excitability

Bifurcation diagram of the Epileptor

The dynamics of the Epileptor is extensively discussed in (Jirsa *et al.* 2014; Houssaini *et al.* 2020; Saggio & Jirsa 2024). For the analysis of the dynamics of the Epileptor model, the slow evolving variable z is used as the control parameter.

With the setting provided by (Melozzi *et al.* 2017), the system exhibits an unstable FP at the centre of a stable limit cycle with decreasing orbit, a stable FP and a saddle-node. **Figure** I.14 shows the corresponding bifurcation diagram, reproduced from (Houssaini *et al.* 2020). At $z \approx 2.8$, the stable FP and the saddle node collide through a SN_1 bifurcation. At $z \approx 4.2$, the unstable attractors collide through a SN_2 bifurcation. Above the unstable FP, the system exhibits two saddle nodes and a stable FP. With decreasing values of z, the stable foci collides with the saddle-node through a SNIC bifurcation (see section I.3.3.2). With increasing values of z, the stable foci and the saddle-node collide through a SN_3 bifurcation.

In the absence of noise, the slow permittivity of the system repeatedly decreases during the interictal phase, then increases during the ictal phase (that is, during the epileptic seizure). The interictal phase corresponds to *healthy* spiking activity where the system remains on the stable FP. Seizure onset occurs at SN_1, where the trajectory is attracted by the limit cycle and the system starts generating bursts. At the SNIC bifurcation, the limit cycle collides with the stable FP and the system shortly remains on a stable position corresponding to an ictal active resting state, before reaching back the original stable position at SN_3.

The same alternation of interictal and ictal phases occurs in noisy systems. However, during the ictal phase, the noise allows the trajectory to explore the phase space around the limit cycle. Seizure offset occurs before expected through a homoclinic bifurcation, when the trajectory crosses the saddle-node within the interval of

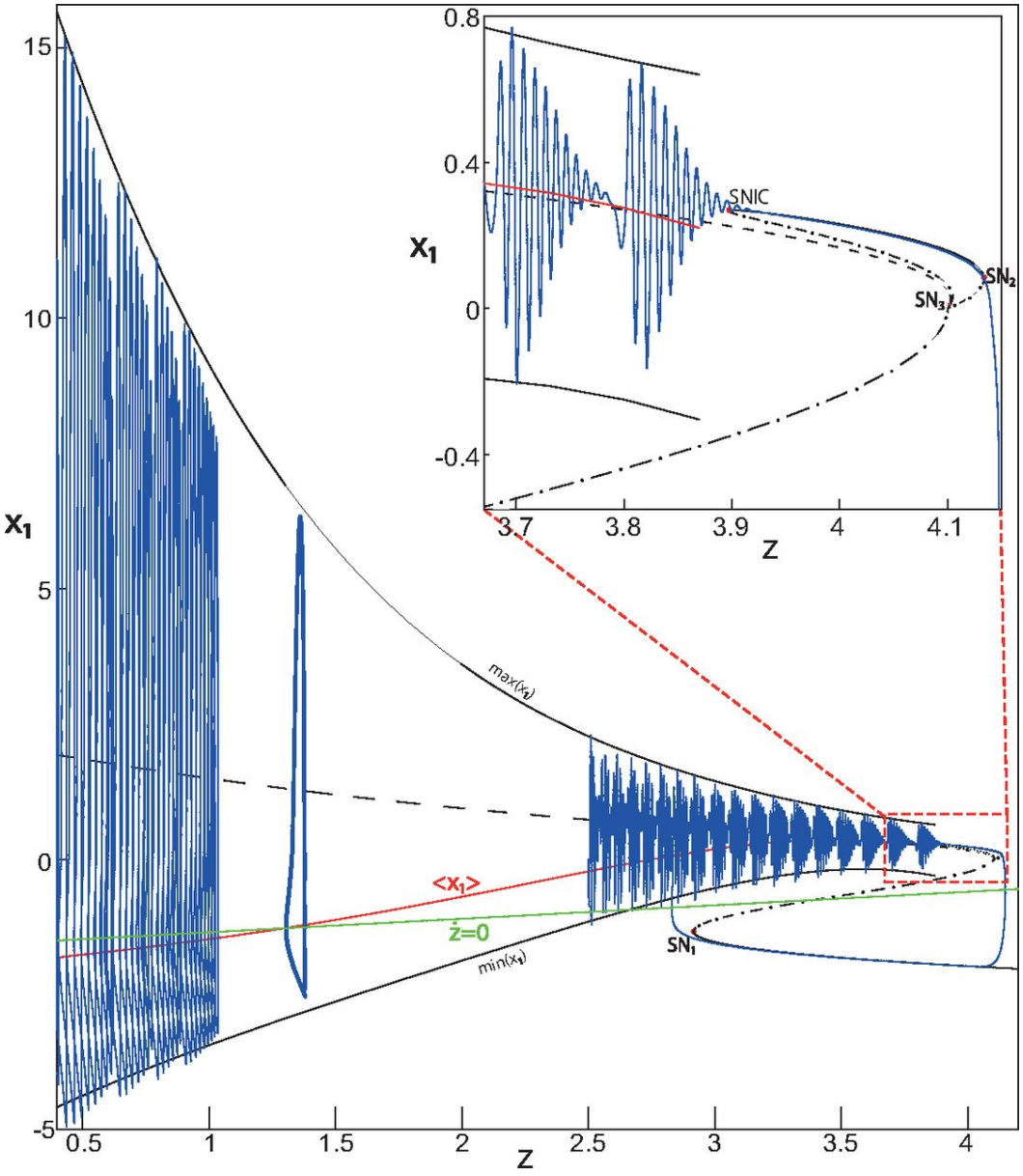

Figure I.14: **The Epileptor model bifurcation diagram.** Z-lower, Z-middle, and Z-upper branches consists of stable nodes, saddles, and unstable foci. Key bifurcations include SN1 (Z-lower and Z-middle branches collide), SN2 (upper sub-branches merge), and SNIC (upper and lower branches collide). Deterministic trajectories illustrate two basins of attraction separated by a saddle orbit. **From:** Kenza El Houssaini, Christophe Bernard and Viktor K. Jirsa. *The Epileptor Model: A Systematic Mathematical Analysis Linked to the Dynamics of Seizures, Refractory Status Epilepticus, and depolarization Block.* eneuro, vol. 7, no. 2, 2020. DOI: ENEURO.0485-18.2019. Licensed under CC BY 4.0.

bistability.

Epileptogenicity

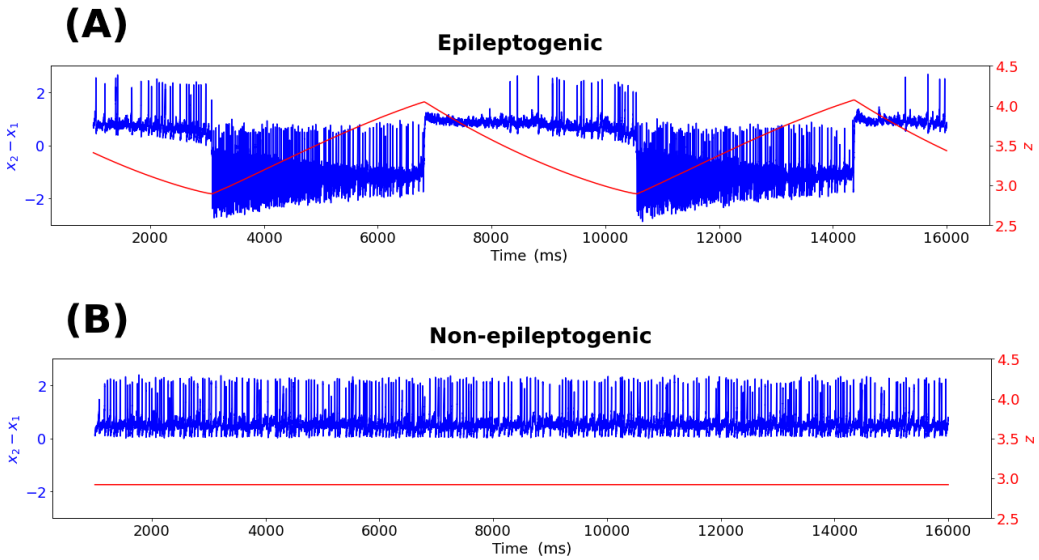

Figure I.15: **Epileptor time-series.** Time-series of **(A)** an epileptogenic Epileptor, with epileptogenicity $x_0 = -1.6$, and **(B)** a non-epileptogenic time-series, with $x_0 = -2.1$. In blue we show $x_2 - x_1$, in red we show the slow permittivity z as a function of time.

The value of the epileptogenicity parameter x_0 acts on the system's distance to bifurcation, and therefore on its ability to produce spontaneous seizures. **Figure** I.15 shows representative time-series of the Epileptor exhibiting epileptic and healthy activity. Below the critical value $x_{0,c} \approx -2.06$, the slow permittivity remains constant over time outside of the bistability region, and the system therefore remains in a *healthy state* where no bursting is produced. For higher values of x_0, the Epileptor follows the trajectories described above with the production of spontaneous seizures.

4.2.3 Coupled Epileptors

Linear coupling term

Multiple Epileptors might be coupled within a network with the addition of a coupling term to the expression of the slow permittivity evolution (equation I.44) (Proix *et al.* 2018; Vattikonda *et al.* 2021). In a network of N coupled Epileptors,

the dynamical evolution of node i is:

$$\dot{x}_{1,i} = y_{1,i} - f_1(x_{1,i}, x_{2,i}) - z_i + I_1, \tag{I.50}$$

$$\dot{y}_{1,i} = 1 - 5x_{1,i}^2 - y_{1,i}, \tag{I.51}$$

$$\dot{z}_i = \begin{cases} r(4(x_{1,i} - x_{0,i}) - z_i - 0.1z_i^7) + K\sum_j c_{ij}(x_{1,i} - x_{1,j}) & \text{if } z_i < 0, \\ r(4(x_{1,i} - x_{0,i}) - z) + K\sum_j c_{ij}(x_{1,i} - x_{1,j}) & \text{if } z_i \geq 0, \end{cases} \tag{I.52}$$

$$\dot{x}_{2,i} = -y_{2,i} + x_{2,i} - x_{2,i}^3 + I_2 + 0.002g(x_{1,i}) - 0.3(z_i - 3.5), \tag{I.53}$$

$$\dot{y}_{2,i} = \frac{1}{\tau}(-y_{2,i} + f_2(x_{2,i})), \tag{I.54}$$

$$\dot{g}(x_{1,i}) = -0.01(g - 0.1x_{1,i}), \tag{I.55}$$

where

$$f_1(x_{1,i}, x_{2,i}) = \begin{cases} 3x_{1,i}^3 - x_{1,i}^2 & \text{if } x_{1,i} < 0, \\ (x_{2,i} - 0.6(z_i - 4)^2)x_{1,i} & \text{if } x_{1,i} \geq 0, \end{cases} \tag{I.56}$$

and

$$f_2(x_{2,i}) = \begin{cases} 0 & \text{if } x_{2,i} < -0.25, \\ 6(x_{2,i} + 0.25) & \text{if } x_2 \geq -0.25, \end{cases} \tag{I.57}$$

with c_{ij} the strength of the connection from node j to node i, and $K = 0.2$ a global coupling strength.

The additive coupling term $K\sum_j c_{ij}(x_{1,i} - x_{1,j})$ represents the total synaptic inputs received by brain area i from other parts of the brain. If brain region i is at rest, adjacent areas already recruited in a seizure (that is, with $x_{1,j} > x_{1,i}$) tend to decrease the slow permittivity of area i, ultimately bringing the system to seizure onset.

Other structural features can be embedded within the Epileptor model. The tract length of each connection can be taken into account through small time delays in the coupling τ_{ij}, so that the additive coupling term is:

$$K\sum_j c_{ij}(x_{1,i}(t - \tau_{ij}) - x_{1,j}). \tag{I.58}$$

Epileptogenic and Propagation Zones

The network of Epileptors can be divided into two groups of nodes:

- Epileptogenic nodes forming the **Epileptogenic Zone (EZ)**, with $x_{0,i\in EZ} > x_{0,c}$, generating spontaneous seizures.

- Non-epileptogenic nodes forming the **Propagation Zone (PZ)**, with $x_{0,i\in PZ} < x_{0,c}$, unable to generate spontaneous seizures. These nodes can

however be recruited in a seizure if they receive external stimuli or inputs from other nodes.

4.2.4 Simulation of seizure propagation

Virtual Epileptic Patient

The Epileptor model has been used in a clinical context to reproduce the propagation pattern of epileptic seizures in the brain of individual patients. The patient's connectome was reconstructed using personnal imaging data. The coupling of specific brain regions could be adjusted to reflect the effect of structural abnormalities in their brain. The epileptogenicity of the different brain regions was set according to clinican expertise and data fitting. The brain model was able to adequately reproduce the propagation of the seizure in the patient's brain, thus creating a *Virtual Epileptic Patient*. Individual models for epileptic brains open the path for a better understanding of the mechanisms underlying epilepsy, but also for new approaches for presurgical evaluation.

Using systematic exploration of parameters and data fitting, the Epileptor model prove to be useful in patient's EZ assessment, by identifying brain regions with high likelihood to generate seizures (Makhalova *et al.* 2022). In (Jirsa *et al.* 2016; Hashemi *et al.* 2020), the authors build a probabilistic framework to generate patient-specific epileptogenicity maps, thus providing a helpful tool for the identification of critical brain regions.

Patient-specific brain models of epilepsy also allow the clinicians to test for different resection options before proceeding to surgical interventions. Various studies showed the advantage of preferentially removing nodes and connections based on their centrality and their location in modular brain structures, rather than removing entire brain areas or equivalent amount of random connections in the same areas. More precisely, highly connected nodes, as well as nodes and edges connecting the different modules of the brain, were identified as good candidates for resection procedures (An *et al.* 2019; Nissen *et al.* 2021).

Virtual Mouse Brain

The Epileptor model has also been used to mimic seizure propagation in mouse brain using the Allen institute's structural connectivity for mice (Melozzi *et al.* 2017). It provided promising results, with simulated seizure spreading patterns similar to experimental observations. The so-called *Virtual Mouse Brain* (TVMB) is further detailed in section I.4.4.1.

4.3 Biophysical model of seizures at the neuron level

With the aim of bridging the dynamics of the phenomenological Epileptor model (see section I.4.2) with biology-based models, (Depannemaecker *et al.* 2022) builds a biophysical model of single neuron for the simulation of seizure-related activity.

4.3.1 Biophysical description of slow-fast neuronal activity

The biophysical model describes the ionic exchanges between the intracellular and extracellular spaces (ICS, ECS) of a neuron immersed within an external bath. Ions flow between the ICS and ECS through the sodium-potassium pump and the sodium, potassium and chloride voltage-gated channels (see **Figure** I.16). The external bath acts as a potassium buffer.

The model consists in a slow-fast dynamical system. Eqs. I.59 and I.60 are derived from Hodgkin-Huxley (HH) type models for single neuron dynamics, and constitute the fast subsystem governing the membrane potential and potassium conductance gating variable:

$$\frac{dV}{dt} = -\frac{1}{C_m}\left(I_{Cl} + I_{Na} + I_K + I_{\text{pump}}\right) \tag{I.59}$$

$$\frac{dn}{dt} = \frac{n_\infty(V) - n}{\tau_n} \tag{I.60}$$

$$\frac{d\Delta[K]_i}{dt} = -\frac{\gamma}{\omega_i}\left(I_K - 2I_{\text{pump}}\right) \tag{I.61}$$

$$\frac{d[K]_g}{dt} = \varepsilon\left([K]_{\text{bath}} - [K]_o\right), \tag{I.62}$$

where the currents and gating variables are expressed through:

$$I_{Na} = (g_{Na,l} + g_{Na} m_\infty(V) h(n))\left(V - 26.64 \log \frac{[Na]_o}{[Na]_i}\right) \tag{I.63}$$

$$I_K = (g_{K,l} + g_K n)\left(V - 26.64 \log \frac{[K]_o}{[K]_i}\right) \tag{I.64}$$

$$I_{Cl} = g_{Cl}\left(V + 26.64 \log \frac{[Cl]_o}{[Cl]_i}\right) \tag{I.65}$$

$$I_{\text{pump}} = \rho \frac{1}{1 + \exp\left(\frac{1}{2}(21 - [Na]_i)\right)} \frac{1}{1 + \exp(5.5 - [K]_o)} \tag{I.66}$$

$$n_\infty(V) = \frac{1}{1 + \exp\left(\frac{1}{18}(-19 - V)\right)} \tag{I.67}$$

$$m_\infty(V) = \frac{1}{1 + \exp\left(\frac{1}{12}(-24 - V)\right)} \tag{I.68}$$

$$h(n) = 1.1 - \frac{1}{1 + \exp(-8(n - 0.4))}, \tag{I.69}$$

with $[K]_{bath}$ the potassium concentration in the external bath, $[X]_i$ (resp. $[X]_o$) the intracellular (resp. extracellular) concentration of ion X, and g_X (resp. $g_{X,l}$) the conductance (resp. leak conductance) governing the ability of ion X to actively and passively pass across the membrane.

Following the principle of electroneutrality, the membrane potential of the neu-

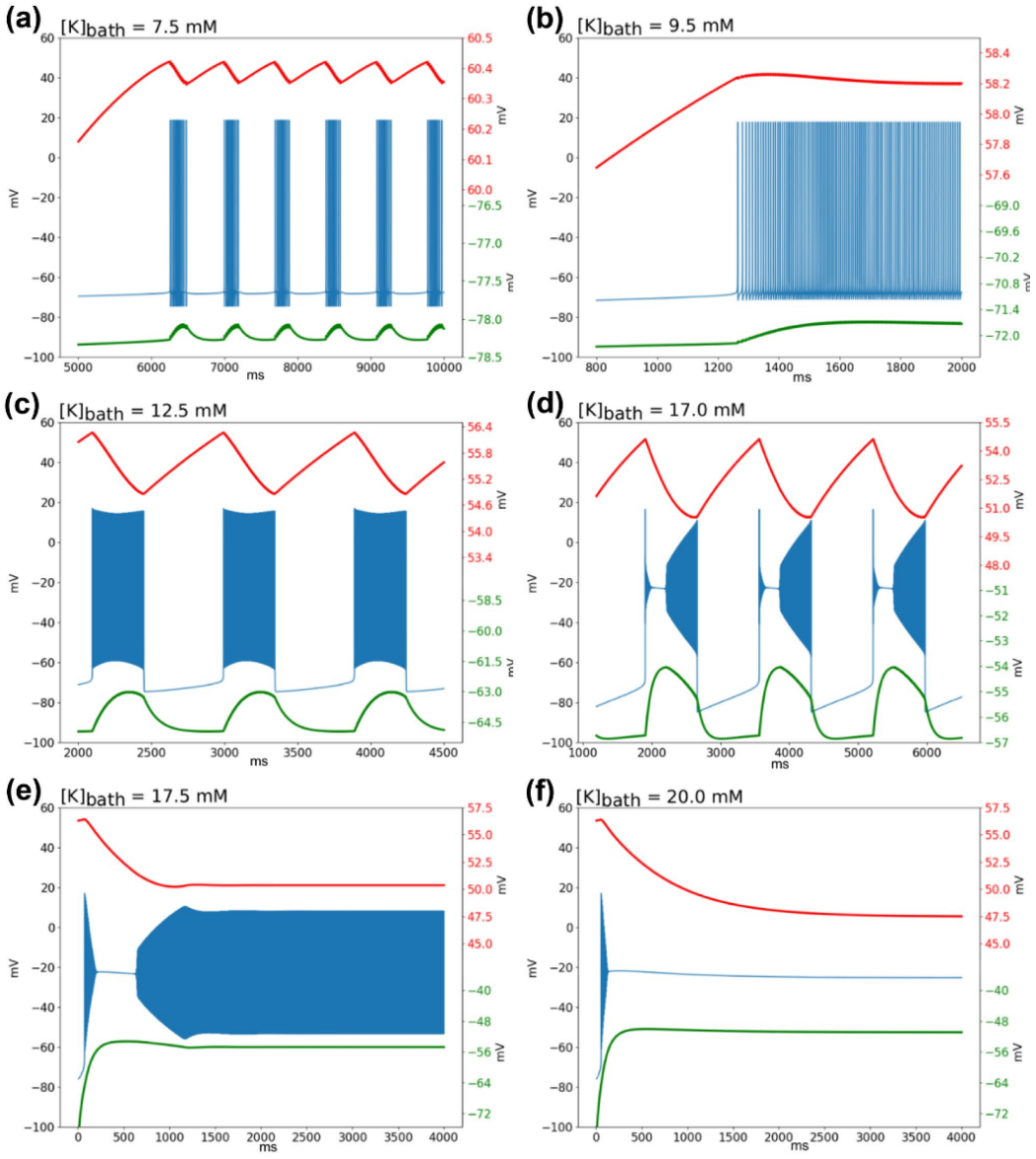

Figure I.16: **Dynamics of the biophysical model of neuronal activity.** Qualitative mode of behavior of the membrane potential and Nernst potentials. In blue: time series of the membrane potential V_m for the following patterns of activity: (a) ST, (b) TS, (c) Bursting, (d) SLE, (e) SIA, (f) DB. In red: Nernst potential of sodium. In green: Nernst potential of potassium. Specific patterns of activities start to appear with a diminution of the Nernst potential of sodium and an increase of the Nernst potential of potassium. **From:** Depannemaecker, D., Ivanov, A., Lillo, D., Spek, L., Bernard, C., & Jirsa, V. (2022). *A unified physiological framework of transitions between seizures, sustained ictal activity and depolarization block at the single neuron level.* Journal of computational neuroscience, 50(1), 33–49. https://doi.org/10.1007s10827-022-00811-1. Licensed under CC BY 4.0.

ron is expressed through:

$$\frac{dV}{dt} = \frac{\omega_i}{C_m \gamma}\left(\frac{d\Delta[K]_i}{dt} + \frac{d\Delta[Na]_i}{dt} + \frac{d\Delta[Cl]_i}{dt}\right) \tag{I.70}$$

and therefore:

$$\Delta[K]_i + \Delta[Na]_i + \Delta[Cl]_i = \frac{C_m \gamma}{\omega_i}(V - V_0), \tag{I.71}$$

with $\frac{C_m \gamma}{\omega_i} \approx 0$, and therefore:

$$\Delta[K]_i + \Delta[Na]_i + \Delta[Cl]_i \approx 0. \tag{I.72}$$

Further assuming the concentration of chloride is constant, the model considers:

$$\Delta[Na]_i = -\Delta[K]_i. \tag{I.73}$$

Variations of the ionic concentrations in the ECS are then expressed through:

$$\Delta[Na]_o = -\beta\Delta[Na]_i \tag{I.74}$$
$$\Delta[K]_o = -\beta\Delta[K]_i \tag{I.75}$$

Finally, the potassium and sodium concentrations are:

$$[K]_i = [K]_{i,0} + \Delta[K]_i \tag{I.76}$$
$$[Na]_i = [Na]_{i,0} + \Delta[Na]_i \tag{I.77}$$
$$[Na]_o = [Na]_{o,0} + \Delta[Na]_o \tag{I.78}$$
$$[K]_o = [K]_{o,0} + \Delta[K]_o + [K]_g, \tag{I.79}$$

with $\beta \in \mathbb{R}$ and $[X]_{i,0}$ (resp. $[X]_{o,0}$) the initial ionic concentration of ion X in the ICS (resp. ECS).

The opening of the K^+ channels is governed by the activation variable n. The dynamics of n is described in equation I.60, and depends on $n_\infty(V)$ the probability of a K^+ channel being open at membrane potentiel V, and on its activation time constant τ_n. Similarly, the Na^+ channel opening (resp. closing) variables m_∞ (resp. h) are treated as instantaneous functions of the membrane potential and tuned to fit mammalian neuron behavior. The slow subsystem (Eqs. I.61, I.62) describes changes in intracellular potassium concentration and extracellular potassium buffering.

4.3.2 Activity patterns

By gradually increasing the external bath concentration of potassium ions $[K]_{bath}$, the model sequentially presents the following activity patterns: resting state (RS), spike train (ST), tonic spiking (TS), bursting, seizure-like events (SLE), sustained

ictal activity (SIA) and depolarization block (DB) (see **Figure** I.16).

4.4 Simulation framework

This section gives a brief presentation of the framework used in this thesis. The Virtual Brain (TVB) is used for the simulation of macro-scale brain networks. Arbor is used for the simulations of micro-scale networks. Both TVB and Arbor are open-source software.

4.4.1 The Virtual Brain (TVB)

The Virtual Brain (TVB) framework (Sanz Leon *et al.* 2013; Sanz-Leon *et al.* 2015) was designed for the integration of large-brain networks dynamics. It provides both a Python setup for theoretical and computational neuroscience-oriented work, and a platform with a visual interface offering more accessibility to healthcare professionals. TVB provides an implementation for multiple mean-field models such as the Wong-Wang and the Epileptor models, while allowing the user to easily tune the model's parameters, noise, coupling and integration. It also provides a large variety of tools, such as hemodynamic models to link simulated neural activity to simulated BOLD signals. Finally, TVB contains multiple sets of imaging data. For instance, TVMB (Melozzi *et al.* 2017) incorporated tools and data from the Allen Institute, providing the user with mouse brain structural connectivity features (see section I.2.3.2) and MRI-based templates.

4.4.2 Arbor

Arbor (Akar *et al.* 2019) is a new-generation neural simulation library suitable for simulating single neurons and neural networks with reduced or detailed neural morphology. It is particularly optimized for speedy, energy-efficient simulations by leveraging GPU resources. Among others, it provides tools for the description of detailed neuron morphology, as well as models of neuronal and synaptic dynamics, and probe mechanisms to monitor multiple properties, such as spiking, membrane potential, ion channel activity, etc. As for TVB, Arbor is highly flexible for the user to tune the simulation setups.

4.4.3 Specific Python libraries

For network analysis, we used the NetworkX open-source Python library (Hagberg *et al.* 2008).

Part II

Modulation of coupled Kuramoto oscillators networks

Adapted from:

Juliette Courson, Thanos Manos and Mathias Quoy (2023).
Networks' Modulation: How Different Structural Network Properties Affect the Global Synchronization of Coupled Kuramoto Oscillators. In: Bountis, T., Vallianatos, F., Provata, A., Kugiumtzis, D., Kominis, Y. (eds) Chaos, Fractals and Complexity. COSA-Net 2022. Springer Proceedings in Complexity.
DOI: 10.1007/978-3-031-37404-3_16.

Introduction

Complex networks' theory is a powerful tool in various fields that allow us to investigate and understand the real world (Barrat *et al.* 2008; Nicolis & Nicolis 2012). For example, different ensembles of neurons connected by synapses coordinate their activity to perform certain tasks (in biology), infrastructures like the Internet are formed by routers and computer cables and optical fibers (in hardware communication) and the human personal or professional relationships (in social sciences) to name a few (Dorogovtsev & Mendes 2003).

Nonlinearity is a very important feature in complex systems giving a rich repertoire of different activity patterns, such as stable, unstable, periodic etc. A modification of some parameter might also produce a change in their stability, and therefore in the dynamics of the system. Furthermore, such systems may have a high sensitivity to initial conditions, or to any external input, that could completely change their dynamics (Strogatz 2018).

Such dynamics often yield to a self-organised coherent activity, i.e. to synchronization. The latter can be loosely defined as the capacity of different oscillating objects to adjust their rhythm due to their interaction and plays a key role in a large variety of systems, whether biological, physical, or even social (see e.g. (Pikovsky *et al.* 2001)). In a more formal way, synchronization emerges from the interaction of several autonomous oscillators, also called self-sustained oscillators. That is, nonlinear dynamical systems that produce oscillations without any need of external source. Their dynamics is given by a nonlinear differential equation or, in the case of multiple coupled oscillators, by several coupled differential equations.

The relative way that autonomous oscillators are connected within a given network can affect their global activity and synchronization properties. Neural networks can be represented as a graph of connections between the different neurons. Since the introduction of small-world networks and scale-free networks (see e.g. (Watts & Strogatz 1998; Barabási & Albert 1999)), the field of network graph analysis has attracted the attention of many studies aimed to better understand complex systems (see e.g. (Jeong *et al.* 2000; Strogatz 2001; Li & Cai 2004; Bassett & Bullmore 2016; Berry & Quoy 2006)). Furthermore, modern network connectivity techniques allow us to capture various aspects of their topological organization, as well as to quantify the local contributions of individual nodes and edges to network's functionality (see e.g. (Sporns 2010)).

In neuroscience, synchronization plays a very important role. The human brain is a very large and complex system whose activity comprises the rapid and precise integration of a gigantic amount of signals and stimulus to perform multiple tasks (see e.g. (Sporns 2010; Chialvo 2010; Fornito *et al.* 2016)). One example occurs in epileptic seizures, where periods of abnormal synchronization in the neural activity can spread within different regions of the brain, and cause an attack in the affected person (see e.g. (Wong *et al.* 1986)). More examples are found in other brain diseases such as Parkinson disease, where an excessively synchronized activity in a brain region correlates with motor deficit (see e.g. (Brown 2003; Manos *et al.* 2021) and references therein) or tinnitus (see e.g.

(Eggermont & Tass 2015; Manos *et al.* 2018a; Manos *et al.* 2018b) and references therein).

In this chapter, we focus at a rather theoretical framework. We set out to investigate the impact of different network architectures, such as Fully-Connected, Random, Regular ring lattice graph, Small-World and Scale-Free in the global dynamical activity of a system of coupled Kuramoto phase oscillators (Kuramoto 1984). The Kuramoto model has been broadly used to study various types of oscillatory complex activity, see e.g. (Acebrón *et al.* 2005; Rodrigues *et al.* 2015; Popovych *et al.* 2021) (to name only a few) and references therein. Our goal is to investigate the impact of the network (graph) structure in the system's global degree of synchronization when applying identical and fixed external stimulus to different subsets of nodes which are chosen according to various network connectivity criteria.

In the context of this thesis, this work aims to gain a better insight on certain dynamical properties occurring in such complex networks. We set up and implement graph theory tools, and study a first case of complex dynamics using a simple model. We discuss network effects, in particular spontaneous and forced synchronization, and demonstrate the impact of network structures on global dynamics.

1 Kuramoto model and network structures

1.1 Network configurations

1.1.1 Network types

In this chapter, we study the dynamics of phase oscillators coupled via binary (that is, unweighted), undirected graphs $G = (V, E)$, containing a set of N vertices. Let $A = (c_{ij})$ be the corresponding adjacency matrix, with $c_{ij} = c_{ji} = 1$ if there is a connection between node i and node j, 0 otherwise. Self-connections are excluded, so $c_{ii} = 0$ for any vertex i.

We investigate synchronization properties in various network configurations that exhibit in general different characteristics. In more detail we here employ the neural networks described in the following list (see e.g. (Watts & Strogatz 1998)):

- **Fully-Connected networks.** They contains $(N-1)^2$ edges connecting every node in one layer to every node in the other layer.
- **Regular networks.** They consist of a lattice of N nodes, each being connected to their k nearest neighbors.
- **Small-World networks.** The Small-World network is constructed from a Regular one after multiple random rewiring phases described in section II.2.1.3. The rewiring occurs with probability $p = 0.2$. The resulting network exhibits both high mean clustering and low mean characteristic path length, that is small-worldness.
- **Random networks.** Using the same procedure as for Small-World networks, setting $p = 1$ produces a Random graph, with all edges being systematically randomly rewired.
- **Scale-Free networks.** The Scale-Free network is built following the Barabási-Albert model (Barabási & Albert 1999), described in section II.2.1.3, with initial size $m_0 = 5$. Scale-free networks exhibit nodes with degrees that are several standard deviations away from the average degree of the network. These highly connected nodes are called *hubs*.

Figure II.1 provides a visual representation of the above mentioned graphs. Note that for visualization purposes we here show only a small fraction of the actual networks that we use later in our simulations where the number of nodes is set be $N = 500$.

1.1.2 Connectivity measurements

In this chapter, we characterize the nodes using their local clustering coefficient, average shortest path length (called shortest path length here for simplicity), and eigenvector centrality, as defined in section II.2.1.2.

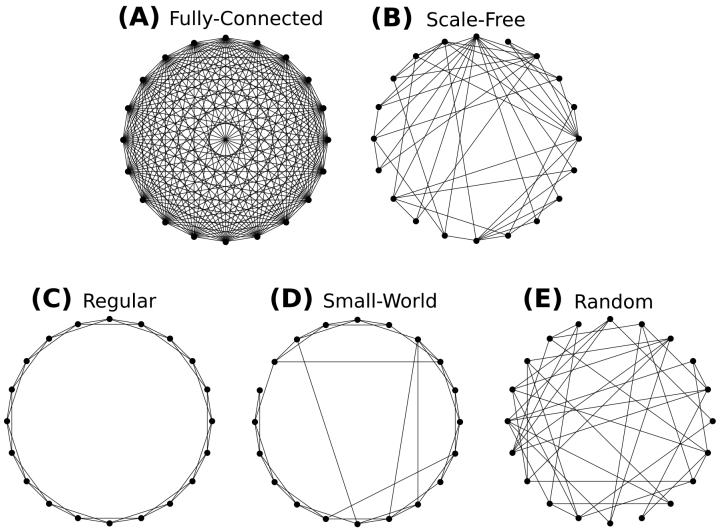

Figure II.1: **Network graphs.** Small graphs of size $N = 20$ showing the different network structures: **(A)** Fully-Connected graph, **(B)** Scale-Free graph with initial size $m_0 = 5$, **(C)** Regular graph with node degree $k = 4$, **(D)** Small-World graph with initial node degree $k = 4$ and rewiring probability $p = 0.2$ and **(E)** Random graph with initial node degree $k = 4$. See text for more details.

1.2 Coupled Kuramoto oscillators

1.2.1 The Kuramoto model

The Kuramoto model aims to describe the dynamics of a population of N self-sustained oscillators, coupled within a network structure. Autonomously, each oscillator rotates around a unit circle with a frequency ω_i, $i \in [\![1 : N]\!]$. In this chapter, the oscillators' respective frequencies ω_i are drawn from a Lorentz probability distribution $g(\omega)$ of scale parameter $\gamma = 0.5$, centered in $x_0 = 1$. The Kuramoto models gives the evolution of the phase of the oscillators:

$$\dot{\theta}_i = \omega_i + \sum_{j=1}^{N} \Gamma_{ij}(\theta_j - \theta_i), \tag{II.1}$$

where θ_i denotes the phase of the $i-$th oscillator, and $\Gamma_{ij}(\theta_j - \theta_i)$ denotes a coupling function linking oscillators i and j. The simpliest case for a system of coupled oscillators corresponds to a fully-connected unweighted network, with a sinusoidal coupling so that:

$$\dot{\theta}_i = \omega_i + \frac{K}{N} \sum_{j=1}^{N} sin(\theta_j - \theta_i), \tag{II.2}$$

where K is a constant global coupling strength. A general form of the latter coupling functions, adapted for more complex network architectures, is:

$$\dot{\theta}_i = \omega_i + \frac{K}{k_i} \sum_{j=1}^{N} c_{ij} sin(\theta_j - \theta_i), \tag{II.3}$$

with k_i the degree of node i, and c_{ij} the strength of connection from node i to node j.

1.2.2 Spontaneous synchronization

The *synchrony* of a system denotes a state of coherent activity. The system's degree of synchrony is measured using its order parameter r (Kuramoto 1984):

$$re^{i\psi} = \frac{1}{N} \sum_{j=1}^{N} e^{i\theta_j}, \tag{II.4}$$

where Ψ denotes the population's mean phase. The order parameter r tends to $\mid r \mid = 1$ for a perfectly synchronized population, and $r = 0$ in the absence of synchronization respectively (see **Figure** II.2 (A), (B) for representations of synchronized and unsynchronous populations). The system's degree of synchrony depends on the coupling strength's relative position to a critical coupling strength K_c, whose value depends on the network configuration (see e.g. (Mirollo & Strogatz 2007; Chiba *et al.* 2018)). At $K < K_c$, the system is desynchronized and all oscillators rotate at their own natural frequency. At $K = K_c$, the system undergoes a pitchfork bifurcation corresponding to a phase transition between desynchronization and synchronization. With a strong global coupling, the oscillators show a self-organized coherent activity. Here, we set this value at $K = 0.2$ so that all considered networks are desynchronized in the absence of any external stimulation.

1.2.3 Forced coupled oscillators

The dynamics of coupled Kuramoto oscillators when an external stimulus of fixed amplitude F and frequency Ω is applied to a subset of nodes is given by:

$$\dot{\theta}_i = \omega_i + F\delta_i \sin(\Omega t + \theta_i) + \frac{K}{k_i} \sum_{j} c_{ij} \sin(\theta_j - \theta_i), \tag{II.5}$$

where δ_i is a binary function indicating the subset of nodes where the stimulation is applied,

$$\delta_i = \begin{cases} 1 & \text{if node } i \text{ is in the stimulated subset} \\ 0 & \text{else.} \end{cases} \tag{II.6}$$

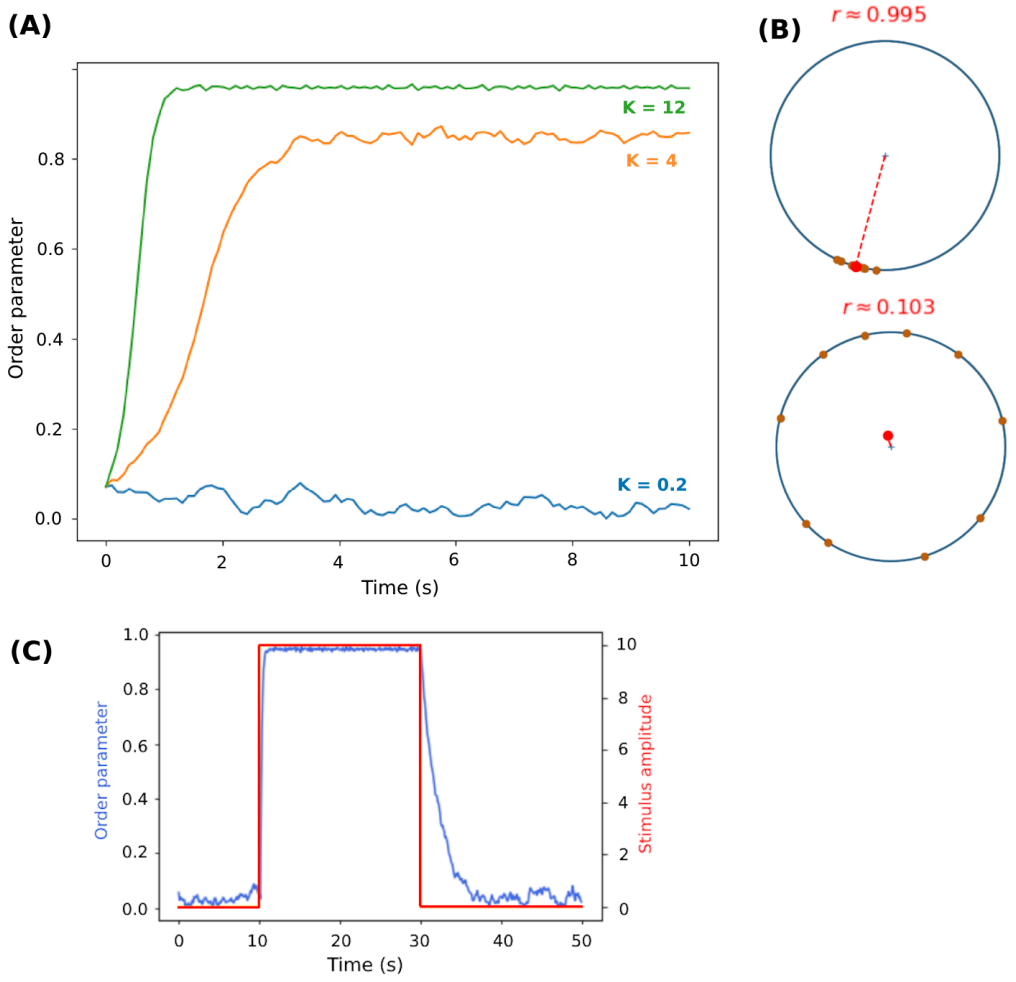

Figure II.2: **Synchronization of coupled Kuramoto oscillators.** **(A)** Order parameter time-series of fully-connected networks of $N = 500$ oscillators, with different global coupling strengths. High coupling systems exhibit spontaneous synchronization. **(B)** Representation of a coherent (top) and unsynchronized (bottom) population of $N = 10$ fully-connected network of oscillators around a unit circle. The red dot represents the mean phase of the network. **(C)** Order parameter time-series of a fully-connected network of $N = 500$ oscillators with low coupling $K = 0.2$. A stimulus is applied between 10 and 30s, entraining synchronization.

Figure II.2 (C) shows the time-series of the order parameter of a fully-connected network of oscillators with low global coupling $K = 0.2$. A stimulus of frequency $\Omega = 3$Hz and amplitude $F = 10$ is applied on a time window between 10 and 30s. During this period, the population rapidly reaches a synchronized state, then slowly goes back to its baseline unsynchronous regime.

1.2.4 Numerical integration

In this chapter, we set the time-step at 0.01s and we integrate the system with an Euler scheme. No noise is considered.

Due to the presence of strong fluctuations, all r time-series shown in the next sections are determined using a moving average on r, on time windows of length 2s sliding each 0.1s. The final states of a population, r_f, are computed by averaging these moving-averaged r time-series over a 15s time-window where the system has reached its stable state.

2 How Different Structural Network Properties Affect the Global Synchronization of Coupled Kuramoto Oscillators

2.1 Network modulation

2.1.1 Exploration of the stimulus parameter space

In order to adequately tune the stimulus' amplitude and frequency values such that they can lead the system into a synchronous state, we first perform a systematic analysis in the parameter space (F, Ω). Hence, we begin by applying external stimulus to all the nodes for each pair of parameters and measure the final order parameter r_f. Such a parameter map reveals the presence of the well-known Arnold tongues (Pikovsky *et al.* 2001), namely regions in the plane (F, Ω) for which the system gets synchronized.

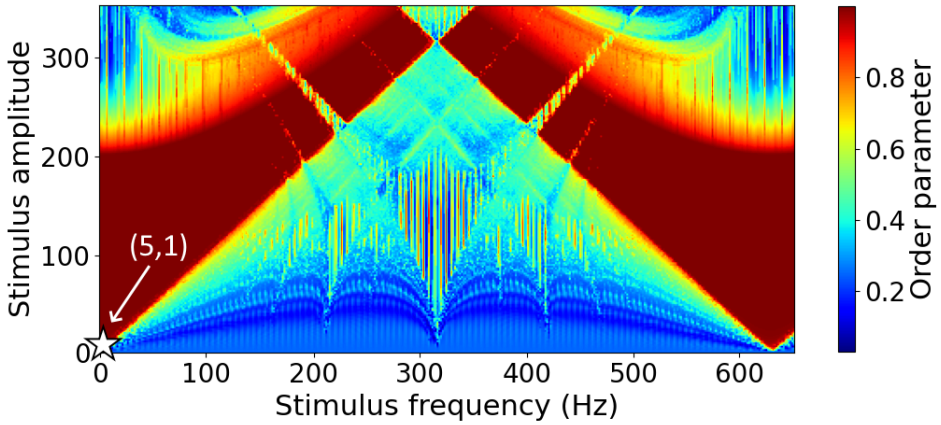

Figure II.3: **Synchronization regions in the stimulation frequency-amplitude parameter space for a Regular network.** Final order parameter reached for a Regular network of size $N = 20$, and degree $k = 4$ where all nodes are stimulated, for different pairs of stimulus intensity (F) and frequency (Ω) values in Eq. (II.5). Each data point corresponds to a single simulation over 30s, the final order parameter being averaged over the last 15s. The color map shows large main synchronization regions, as well as small higher-order synchronization areas. The white star symbol at the bottom-left part of the figure indicates the chosen parameters $(F, \Omega) = (5, 1)$ for the forthcoming simulations.

In **Figure** II.3, we present the different synchronization regions (presence of several Arnold tongues) for a Regular network of a relatively small size $N = 20$ and mean neighborhood $k = 4$. For every other studied network, the maps depicts

similar features.

2.1.2 Phase-locking, partial phase-locking

Constrained Kuramoto oscillator networks exhibit large synchronization regions at relatively small amplitudes of the external current, $F < 200$. These tongues get thinner with higher values of F. Inside the main Arnold tongues, the oscillators are phase-locked at the forcing frequency Ω and $r_f \approx 1$. Inside zones of weaker degree of synchrony $r_f < 1$, some oscillators are phase-locked, while the oscillators of higher natural frequencies keep rotating independently. The white star symbol in the bottom-left part of the figure indicates the chosen parameters $(F, \Omega) = (5, 1)$ for our forthcoming simulations, resulting in a partial phase-locking of the network. Note that we have performed similar analysis with larger sizes but smaller parameter grid size and the overall picture turns out to be consistent.

2.2 Stimulation of selective subsets of nodes

2.2.1 Simulation protocol

We set the values $F = 5$, $\Omega = 1$Hz for the stimulus intensity and frequency in Eq. (II.5), so that the network is weakly entrained without being completely phase-locked. We then measure the degree of synchronization (with the order parameter) in different networks described in section. II.1.1.1. The system starts evolving for 4s without any external input before we start applying the stimulation to a subset of nodes until 30s. More precisely, we stimulate different fractions of nodes, i.e., 25%, 50% and 75% in each given network. These nodes can be either chosen randomly, or depending on particular connectivity properties (as described in section II.1.1.1). For the latter case, we first sort the nodes according to their connectivity relative measurements (from higher to lower), i.e. the eigenvector centrality, average shortest path length and clustering coefficient. The resulting time series are smoothed with a moving average, and their r_f is averaged over the last 15s. In order to obtain a statistically relevant value of the final value of the order parameter r_f, we performed 20 simulations for each different network-setup (randomizing the initialization/generation of the networks, the natural frequencies and the initial conditions for each simulation).

2.2.2 Representative time-series

In **Figure** II.4, we show representative time-series for various stimulation setups for Scale-Free networks of size $N = 500$ and initial size $m_0 = 5$. Each panel corresponds to a different initialization, from which the order parameter evolution is computed depending on the amount of stimulated nodes and the way they are selected. Thin solid lines correspond to randomly selected nodes. In that case, a first subset containing 25% of the nodes is created. Then for the stimulation of

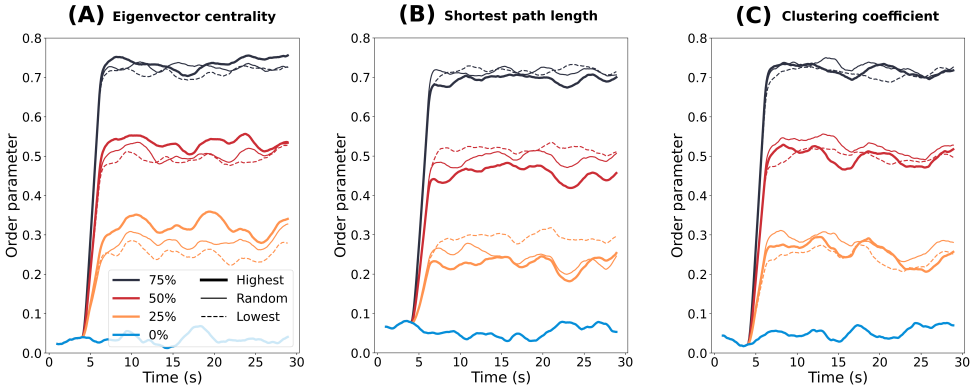

Figure II.4: **Representative r time-series for different stimulation setups of Scale-Free networks.** The order parameter as a function of time, for $N = 500$ oscillators, when stimulating 0% (blue), 25% (orange), 50% (red) and 75% (black) of the nodes. The stimulated nodes are chosen randomly, then based on their **(A)** eigenvector centrality **(B)** average shortest path length and **(C)** clustering coefficient values. Bold solid lines (resp. dashed lines) correspond to the stimulation of nodes with the highest (resp. lowest) values, while thin solid lines correspond to the stimulation of randomly chosen nodes.

larger in size subsets, another 25% of nodes is successively added, so that larger subsets of random nodes always contains the smaller one. The bold solid lines (resp. dashed lines) show the time-series when the stimulated nodes are the ones with the highest (resp. lowest) eigenvector centrality (panel **(A)**), average shortest path length (panel **(B)**) and clustering coefficient (panel **(C)**). Note that higher values of the connectivity measurement do not necessarily lead to stronger synchrony. In particular, lower values for the nodes' average shortest path length depicts shorter connections to the rest of the network, and therefore a more efficient synchronization.

2.3 Optimization of global synchronization

In **Figure** II.5, we present the main finding of our work, namely a systematic comparison of the synchronization efficiency when applying identical stimulus in different types of graph networks. Each panel is split into 3 columns showing the statistical summary for the ensembles of different realizations and choosing to stimulate different subsets of nodes, i.e. randomly (middle-orange boxplots in the legends) or with highest (upper-red boxplots in legends) or lower (lower-blue boxplots in the legends) connectivity measurement. Panel **(A)** refers to a Small-World network of size $N = 500$, initial degree $k = 4$ and rewiring probability $p = 0.2$, **(B)** to a Random network of size $N = 500$, initial degree $k = 4$ and rewiring probability $p = 1$ and **(C)** to a Scale-Free network of size $N = 500$ and initial size $m_0 = 5$ respectively. Note this analysis is not performed on Regular and Fully-Connected networks, since

all nodes of such networks have identical connectivity properties and does not allow any connectivity-based selection.

In Scale-Free networks, the global order parameter reaches higher values when the stimulus is applied to the nodes with higher eigenvector centrality or lower average shortest path length. In such networks, a small fraction of the nodes have significantly higher connectivity, and stimulating preferentially these nodes enables strong synchronization compared to stimulating random nodes.

In Random networks, selecting stimulated nodes according to their lowest average shortest path length instead of randomly enhances synchronization. However, there is no benefit in choosing more central nodes. Indeed, the high degree of randomness (induced by a rewiring probability $p = 1$, see section II.1.1.1) in these networks' connections causes disparity in the nodes' average shortest path length, without creating any node of way higher centrality.

In Small-World networks, the connections are distributed in a more homogeneous way, and hence the node selection as no substantial impact on the system's final synchrony.

For all three aforementioned networks and all stimulation subset sizes, the selection of the nodes according to their clustering coefficient does not show any advantage over a simple random choice. Note that, we also checked for a potential overlap of clustering coefficient values between the randomly chosen nodes and those chosen with higher respective values. It turns out that they differ significantly. Our working hypothesis is that, by picking nodes with higher clustering coefficient, we induce higher synchrony locally (member nodes of the sub-network) while we disfavour other nodes outside of it. However, by choosing nodes randomly, we end up stimulating simultaneously nodes within and outside clusters eventually providing a better global synchronization. Finally, for all networks and stimulation subset selection methods, although they overall achieve higher degree of synchrony, larger stimulated subsets containing 75% of the population do not allow to observe any clear advantage in particular selection of the nodes, since all three possible subsets largely overlap.

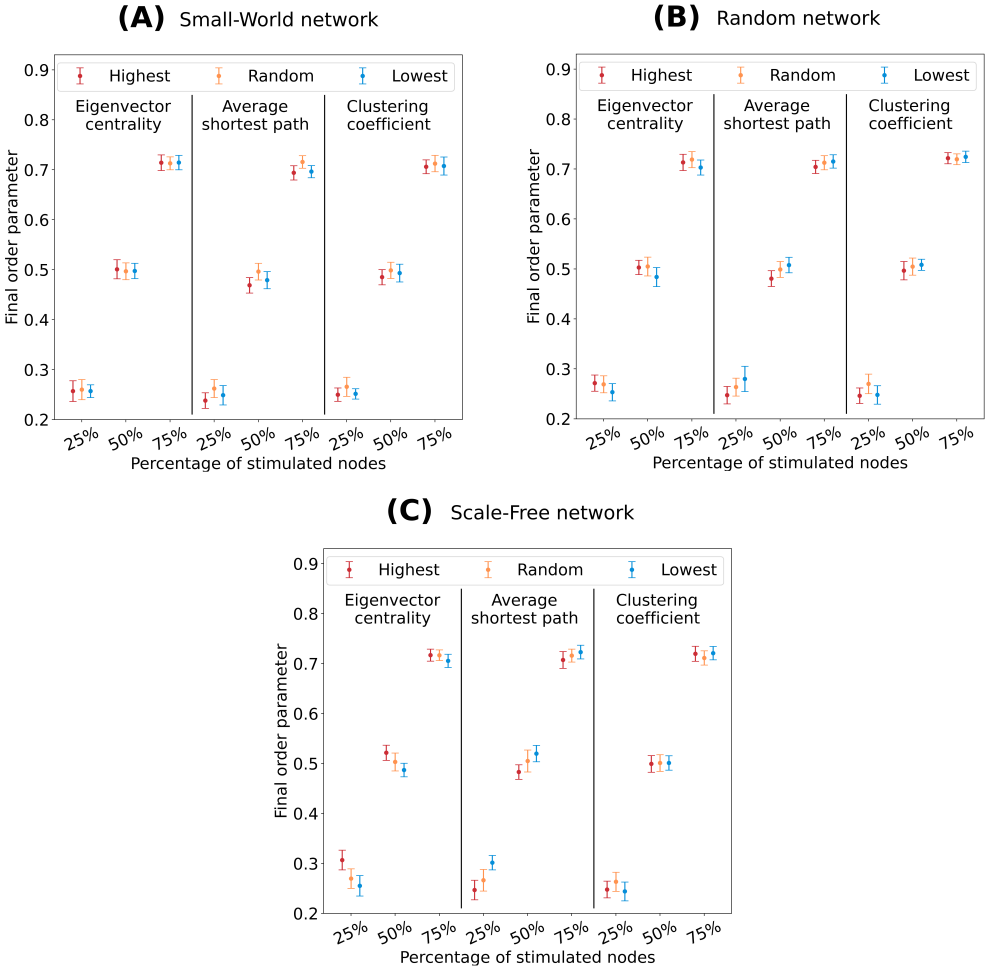

Figure II.5: **Synchronization efficiency comparison for different types of graph networks.** Final order parameter obtained, for **(A)** Small-World networks **(B)** Random networks **(C)** Scale-Free networks of size $N = 500$. The final value of the order parameter r_f is computed for different stimulation subset sizes, composed of randomly chosen nodes (middle-orange boxplots in the legends), nodes with the highest connectivity measurement (left-red boxplots) and nodes with the lowest connectivity measurement (right-blue boxplots). r_f shown are an average over 20 simulations. The analysis is performed with three different connectivity measurements: eigenvector centrality (left column in each panel), average shortest path length (central column in each panel) and clustering (right column in each panel).

Discussion

In this chapter, we investigated the impact of structure and connectivity properties in a modulated network. We sought out to identify efficient ways to synchronize a population of Kuramoto phase oscillators using nodes' stimulation with fixed small amplitude and frequency. To this end, we first performed a parameter sweep exploration for stimulus amplitude and frequency parameters to identify settings that allow the system to synchronize. Then, we computed the evolution of characteristic networks of Kuramoto oscillators, where external stimulation is applied to different subpopulations with identical fixed low amplitude and frequency. In order to measure the system's synchrony of each network-type and stimulation configuration, we calculated the global order parameter for ensembles of different random system initializations.

We showed that by choosing this subpopulations based on their respective network connectivity properties (i.e. high eigenvector centrality and lower short-path length), we were able to enhance the networks' global degree of synchronization in comparison to the one achieved by randomly choosing them. This is not the case when using the clustering coefficient as a selection criterion. However, this direction deserves further investigation, e.g. detect different network communities, measure their local synchronization and study its impact on the global synchrony when such nodes are chosen to be stimulated.

From a neuroscience point of view Scale-Free networks play an important role in the structure and function of mammal brains, see for example (Ribeiro *et al.* 2021) (a study on the scale-free dynamics and the emergence of collective organisation occurs in rodents) or (Grosu *et al.* 2023) (investigating the fractal structure of the human brain and its dynamics). Furthermore, in Alzheimer patients' brain, the functional connectivity structure is found to exhibit properties similar to Random network graphs (see e.g. (Stam *et al.* 2009; Kang & Petrasek 2014) and references therein). Thus, understanding how to optimally synchronize systems with similar network structures can improve the overall expected performance of a given external simulation protocol.

Part III

Propagation prediction and control of widespread epileptic seizures in mice brain

Adapted from:

Juliette Courson, Mathias Quoy, Yulia Timofeeva and Thanos Manos (2024). *An exploratory computational analysis in mice brain networks of widespread epileptic seizure onset locations along with potential strategies for effective intervention and propagation control.* Frontiers in Computational Neuroscience, vol. 18. DOI: 10.3389/fncom.2024.1360009.

Introduction

Over the past years there has been an increasing integration of neuroimaging data to enhance the accuracy and predictive capacity of mathematical models (Popovych *et al.* 2019; Popovych *et al.* 2021; Manos *et al.* 2023). This integration occurs within a virtual (computational) environment where simulations enable the exploration and derivation of parameters that could eventually facilitate the prediction of micro- and macro-scale brain activity states (Shusterman & Troy 2008; Jirsa *et al.* 2017; Chizhov & Sanin 2020). Personalized models of epileptic brain using patient-specific data provide a better understanding of seizure propagation patterns and allow us to test various resection options before surgery (see e.g., (Jirsa *et al.* 2016; Gerster *et al.* 2021)). These studies highlight the relevance of preferentially removing connections based on their location in the modular brain structure (see e.g. (Olmi *et al.* 2019; Nissen *et al.* 2021)). In (An *et al.* 2019) the authors used mathematical models and brain network simulations, coupled with modularity analysis based on individual structural brain connectivity to pinpoint optimal surgical target areas. Subsequent to this investigation, in (Hashemi *et al.* 2020) the authors introduced a probabilistic framework capable of inferring the spatial distribution of epileptogenicity within a personalized, large-scale brain model of epilepsy propagation. In (Makhalova *et al.* 2022), the authors used such computational approaches to compare the regions identified as epileptogenic by the so-called Virtual epileptic patient brain model to those defined by clinical analysis (see also (Jirsa *et al.* 2023)).

A viable alternative is to use virtual mice models. Indeed, rodent species are often regarded as suitable analogs for humans due to the significant similarities in brain structure and connectivity between the two (Grone & Baraban 2015; Marshall *et al.* 2021). Scientists frequently opt for laboratory mice as research subjects because these creatures also bear genetic resemblance to humans and have shorter lifespans, enabling multi-generational studies. Furthermore, advancements in imaging technology are rapidly enhancing the precision and detail of experimental data. The latest iterations of MRI machines, for instance, provide intricate insights into the anatomical, structural, and functional aspects of the entire rodent brain (Stafford *et al.* 2014). The primary objective of mouse-based research is to deepen our comprehension of brain function and malfunction. The ultimate goal is to acquire new knowledge of the mechanisms controlling and intervening in the brain dynamics which can be later utilised in human brain's therapies, like for example in the treatment of Epilepsy.

A better understanding of the role of neural network's topological properties in the spatiotemporal propagation of epileptic activity would open the path for more effective EZ identification, and better resection strategies. In (Toyoda *et al.* 2013), the authors used recording electrodes to assess the propagation of seizures in rats experiencing spontaneous seizures. They observed that the initial seizure activity was most frequently detected in the hippocampal formation, followed by sequential spreading to the subiculum, entorhinal cortex, olfactory cortex, neocortex, and striatum. In (Melozzi *et al.* 2017), the authors numerically simulated the dynamical

behavior of a mouse brain to replicate certain aspects of the anatomical reorganization observed in medial temporal lobe epilepsy reported in (Toyoda *et al.* 2013). To this end, they focused on the loss of neuronal connections in the hippocampal regions (CA1 and CA3) [see also experimental findings in (Esclapez *et al.* 1999)] and they eliminated (in silico) all incoming and outgoing connections of CA1 and CA3 brain areas in the hippocampus to prevent widespread epileptic seizure propagation.

Epileptic seizures arise from an imbalance in the regulation of stimulation and inhibition. Cellular-level processes involve ion transporters, pumps, and channels that govern the entry and exit of positively or negatively charged ions within neurons. These mechanisms are further modulated by factors such as voltage or ligands, either binding directly or through G protein receptors, which exert control over these pumps and ion channels (see (Bakhtiarzadeh *et al.* 2023) and references therein). There are several anti-seizure drugs that have been reported to suppress epileptiform spikes and improve synaptic and cognitive function (see (Kanner & Bicchi 2022) for a recent review). In parallel, neuromodulation techniques have emerged as promising strategies for influencing brain activity and have gained considerable attention in the context of managing seizure propagation. One of the key players in this field is transcranial magnetic stimulation (TMS), which non-invasively modulates neuronal excitability by generating magnetic field that induce electrical currents in targeted brain regions. Studies have shown that repetitive TMS (rTMS) can alter cortical excitability and disrupt abnormal synchronization of neuronal networks, thereby attenuating seizure propagation, see e.g., (Tsuboyama *et al.* 2020) and references therein. Additionally, vagus nerve stimulation (VNS) has demonstrated effectiveness in reducing seizure frequency and severity by modulating the autonomic nervous system and releasing neurotransmitters that promote inhibitory signaling, see e.g., (Toffa *et al.* 2020) and references therein. Moreover, recent advancements in closed-loop neuromodulation, such as responsive neurostimulation (RNS), offer real-time monitoring and adaptive delivery of electrical pulses to preemptively suppress abnormal neuronal activity and prevent seizure spread (Heck *et al.* 2014). These findings highlight the potential of neuromodulation techniques as adjunctive therapies for controlling seizure propagation and improving the quality of life for individuals with epilepsy.

In this chapter, we computationally study how the location of an EZ area and its connectivity relevance in the network are related to widespread seizure propagation in a mice brain and we search for strategies that can confine widespread seizures by either removing the minimum amount of brain tissue (by blocking certain connections in the network), or suppress the hyperexcitation (loosely mimicking a anti-seizure drug or neuromodulation effect). To this end, instead of (computationally) resecting the whole EZ tissue from both brain hemispheres as in (Melozzi *et al.* 2017) (via a graph edge removal), we sought out to systematically identify and remove (or block) the minimal amount of connections required to prevent a widespread seizure propagation. In addition, we followed an alternatively approach to computationally model (in a loose sense) the effect of a drug at a macroscopic scale (i.e., suppression of network hyperexcitability). To this objective, we altered locally the outgoing

weight connections in our structural connectome to account for the inhibitory effect of such a drug in the vicinity of a given EZ area. In both of our approaches, the ultimate goal is to minimize the surgical or medical intervention and preserve as much as possible the pre-surgical structural connectivity as well as the maximum possible amount of the brain functionality.

1 Epileptor, epileptogenic zone and mouse brain structure

1.1 Dynamical system

1.1.1 Tuning of the Epileptor model

In our study, we consider a network of N Epileptors, coupled via an adjacency matrix $A = (c_{ij})$ while we do not include any delays using track length data. The epileptic seizure-like events are produced by the model described in section 4.2.3. Following the work of (Melozzi *et al.* 2017) and tuning our system in a similar state, we set $I_1 = 3.1$, $I_2 = 0.45$, $r = 3.5.10^{-4}$, $K = 0.2$, $\tau = 10$ s. Additive Gaussian white noise with standard deviation $\sigma = 0.0025$ is added to Eqs. (I.53) and (I.54). Our simulations were performed with The Virtual Brain (TVB) platform (Sanz Leon *et al.* 2013; Sanz-Leon *et al.* 2015).

1.1.2 The Epileptogenic Zone

In our work, and for each brain node, we focus only on the epileptogenicity parameter ($x_{0,i}$) and we adjust its value according to healthy or epileptic condition of each node. The critical epileptogenicity parameter for the transition from one state to the other is found to be $x_0^c \approx -2.06$ (see (Houssaini *et al.* 2020)). An EZ node (Jehi 2018) is selected to produce spontaneous epileptic seizures, while the rest of the brain nodes form the healthy Propagation Zone (PZ). We set the values of the epileptogenicity in these brain nodes as $x_0 = -1.6$ for the EZ and $x_0 = -2.1$ for the PZ nodes.

1.1.3 Seizure onset detection

In order to systematically detect the seizure onset for each brain area and its widespread (or not) evolution to other regions, we use the evolution of the slow permittivity z. First, we allow the system to evolve for approximately 15 seconds (this also depends on the onset of a first seizure) to eliminate temporary effects. At this stage all PZ nodes are in a stable state (i.e., the z variable value is approximately constant), and the EZ does not produce a seizure yet. Therefore, we define seizure onset time $T_{\text{onset},i}$ in each brain area i, as the time when the slow permittivity (z) starts increasing. To track the propagation of the seizure among brain areas, we define the time distance from seizure onset in each network node i:

$$T_i = \begin{cases} 0 & \text{if node } i \text{ is the EZ,} \\ T_{\text{onset},i} - T_{\text{onset,EZ}} & \text{otherwise.} \end{cases} \tag{III.1}$$

with $T_{\text{onset,EZ}}$ the onset time of the seizure in the EZ.

In **Figure** III.1, we show examples of an epileptogenic (in red) and healthy (in blue) nodes activity produced by the Epileptor model. The time evolution of the fast variable $x_2 - x_1$ is depicted in blue (non EZ) and red (initially an EZ). The

slow permittivity variable z is in black. Non-epileptogenic brain areas can either be recruited in the seizure, or maintain a healthy activity. Some examples detecting the time stamps of seizure onset in each node using the slow variable z are also depicted in **Figure** III.1.

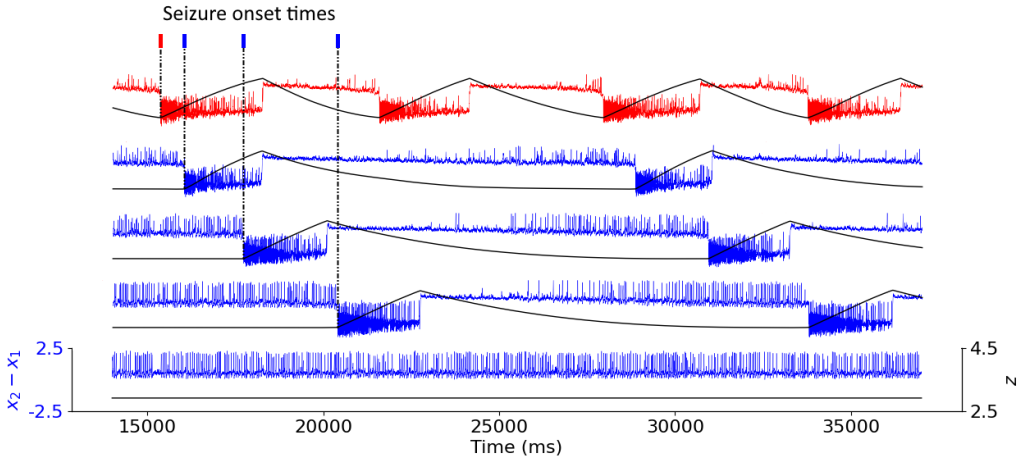

Figure III.1: **Coupled Epileptor model time-series.** Time series of the fast variable $x_2 - x_1$ of the Epileptor model (in color) depicting the neural activity of the nodes, and of the slow variable z (in black). The epileptogenic Epileptor (in red) produces spontaneous seizures, with $x_0 = -1.6$. The non-epileptogenic Epileptors (in blue), with $x_0 = -2.1$, can either be recruited in the seizure or maintain healthy activity. For all recruited areas, time stamps indicate seizure onset.

1.2 Structural connectivity

1.2.1 Original mice brain connectome

Our mouse brain network consists of $N = 98$ Epileptors (Melozzi *et al.* 2017) coupled with a structural connectivity (SC) weight matrix adopted by the Allen Institute that was presented in (Oh *et al.* 2014) and used in (Melozzi *et al.* 2017). In the coupling term of Eq. (I.52), we do not consider self-connections (i.e. $c_{ii} = 0$). The SC matrix SC$= (c_{ij})$ is shown in **Figure** III.2, where c_{ij} denotes the weight of the connection going from area i to area j in base-ten logarithmic scale for better visualisation. The Allen Institute neuroimaging analysis consistently involves source regions exclusively situated in the right hemisphere. The SC matrix used here the left hemisphere's counterpart constructed by mirroring the right hemisphere. Originally, the strength of connections between a given region and another was computed as the average across several experiments utilizing those specific brain areas as source and target regions (see (Melozzi *et al.* 2017) for more details). The SC matrix is divided into four blocks, i.e., R-R, R-L, L-R, and L-L (in a clockwise order from the upper left), symmetries emerge where R-R equals L-L and R-L equals L-R. This as-

sumption is grounded in the notable lateral symmetry observed in the mouse brain, as reported in (Calabrese *et al.* 2015). The dynamics of Epileptors coupled through this connectome adequately reproduces the seizure recruitment order (in the hippocampus, Subiculum, Enthorinal cortex, Olfactory cortex, Isocortex and Striatum, with epileptogenic left CA1, CA3 and Dentate Gyrus) (Melozzi *et al.* 2017) that is also experimentally observed by (Toyoda *et al.* 2013).

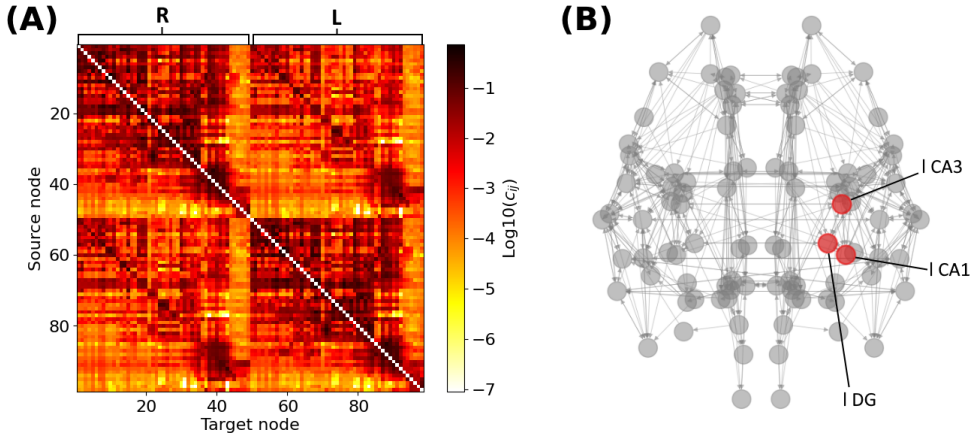

Figure III.2: **Structural connectivity matrix and mouse brain network. (A)** Allen Structural Connectivity matrix. The elements of the matrix show the logarithm of the weight for the connections between any pair of brain areas. Node indices ranging from 1 to 49 form the right hemisphere (R), node indices ranging from 50 to 98 form the left one (L). **(B)** Mouse brain network graph. Only connections of weight higher than 0.1 are shown for visibility reasons. The red nodes indicate the areas composing the left hippocampus. Note that the left brain hemisphere appears on the right hand side of our template.

1.2.2 Connectome randomization

For statistical relevance of our computational findings, we also produced a set of 20 connectomes derived from the original SC. Namely, each new weight c'_{ij} value of the connection between areas i and j is randomly generated from a normal distribution with mean c_{ij} and standard deviation $0.1c_{ij}$. In the case where a new weight is negative, we set $c'_{ij} = c_{ij}$. Note that the most prominent modifications occur in the relatively strong connections and that these modifications induced a minor loss of the original SC's symmetry between left and right hemisphere. The randomized SC are shown in the Appendix, see **Figures** A.1 and A.2.

1.2.3 Network graph measurements

We characterize each node of the network with different connectivity measurements introduced in III.2.1.2, namely their in and out-degree, their eigenvector centrality

and their average shortest path length. To compute path lengths, the length of each connection is artificially defined as:

$$l_{ij} = c_m - c_{ij}, \tag{III.2}$$

with c_m the largest weight value of a connection in the network, so that strong connections account for short distance. Note that l_{ij} is always defined as the mice brain graph is complete, i.e., each pair of graph vertices in the graph is connected by an edge. Therefore there is always a way connecting node i to node j. The lower the shortest path length, the fastest the information goes from one node to another.

To study the relative importance of various nodes within a brain network, these connectivity measurements are normalized. With m_i is the initial connectivity measurement value for node i and $m^{\max}$ the maximal value of the measurement among the brain nodes, we define the normalized value as $\frac{m_i}{m^{\max}}$.

2 Simulation of seizure propagation

2.1 Seizure initiation in the Hippocampus

The location of the Epileptogenic Zone in a given mice brain network determines the propagation (i.e. generalized seizure - occurring in both hemispheres of the brain) or non-propagation (i.e., focal - occurring in one area of the brain or hemisphere in the brain that remains localized) of the epileptic seizure. We start by computationally initiating epileptic seizures within different areas of the hippocampus, namely the CA1, CA3 and DG separately and not all three simultaneously (nor combinations of pairs of them). Our rationale in doing so is to begin by investigating whether there is an systematic association between the seizure onset at a certain sub-region (CA1, CA3 and DG) and the type of seizure, e.g. widespread vs localized. **Figure** III.3 displays the time distance from the initiation time of a seizure at a EZ node to reach different brain areas in a template of a mice brain slice. **Figure** III.3(A) shows an example of a widespread seizure, starting in left-field CA1 and spreading to almost all brain areas (nodes). **Figure** III.3(B) shows an example of a focal-localized seizure, starting in left-field CA3. Note that in the latter case, the epileptiform activity remains confined in the vicinity of the EZ. This preliminary finding provides a first hint that an epileptic seizure occurring in CA1 or CA3 may have a rather different propagation in the other brain areas.

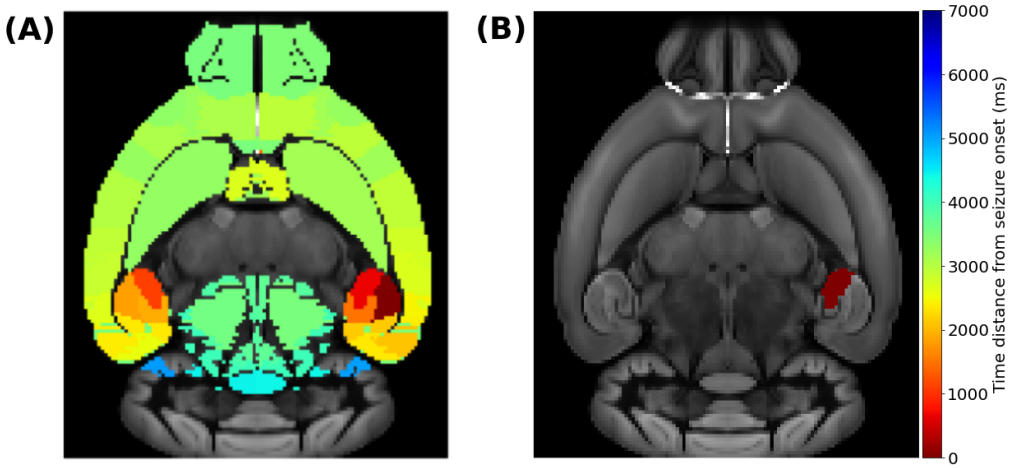

Figure III.3: **Simulating widespread and localized epileptic seizures on the mouse brain. (A)** A widespread (generalized) seizure that starts in left-field CA1. **(B)** A local seizure that starts in left-field CA3. The colorbar indicates the time-distance from seizure initiation in each respective brain area during its propagation.

2.2 Identification of widespread seizure onset locations

2.2.1 Widespread and localized seizures

Next, we performed similar simulations by initiating seizures at all available brain areas of the Allen atlas. Our motivation, at this stage, was mainly computational, i.e., to identify other brain areas where the onset of a seizure will result to either a widespread or a localized one. Moreover, and for statistical significance, we repeated the simulation for 20 additional different (but similar) SC matrices that we generated as explained in the Materials and Methods section. These SC matrices can be found in the Supplementary Material (**Figures** A.1 and A.2). Note that, as the original connectome has symmetrical connections between left and right hemispheres, the simulations were only performed for EZ within the left hemisphere and were duplicated for the right hemisphere EZ. Regarding the randomly modified SC connectomes, we ran simulations considering EZ regions in both hemispheres separately as the matrix symmetry between the two hemispheres is lost.

Figure III.4 shows the percentage of seizure-recruited brain areas for each EZ brain area in the original mice brain connectome, labelled as Allen SC in the first row of each panel, and in the 20 SC randomly generated, labelled by their cardinal number (20 rows above the original Allen SC row separated by the while horizontal line). The resulting epileptic seizures allow a clear binary distinction between widespread and local seizures. Namely, our model and the available SC mice connectomes resulted in generating either localized seizures (no widespread propagation at all or limited up to only two regions) or widespread seizures (reaching almost all brain areas). **Figures** III.4(A) and (B) summarize the simulations for left and right brain hemispheres respectively. Mild modification in the SC matrices can lead to different types of seizure propagation that are initiated at different EZ areas. Some nodes generate exclusively localized seizures (e.g. areas 1 or 45 in dark blue of the right hemisphere) whereas others generate widespread ones (e.g. areas 7 or 13 in dark red of the right hemisphere). However, there are also EZ regions where the type of the seizure depends on the particular SC matrix (e.g. area 75 in the left hemisphere). The hippocampus area is considered to be among the most common source of epileptic seizures. The yellow frame indicates the three nodes comprising the left hippocampus, namely left-field CA1 (l CA1, node 73), left-field CA3 (l CA3, node 74) and left Dentate Gyrus (l DG, node 75). For all randomized connectomes, left-field CA1 produces widespread seizures, while left-field CA3 produces localized seizures with no propagation. left Dentate Gyrus can either produce local or widespread seizures, depending on the SC matrix.

2.2.2 Connectivity of nodes producing widespread vs local seizures

We sought to explore plausible associations between a chosen EZ region's influence in the network (quantified by a graph connectivity measurement) and the resulted type of seizure (localized vs widespread). **Figure** III.5 shows different types of

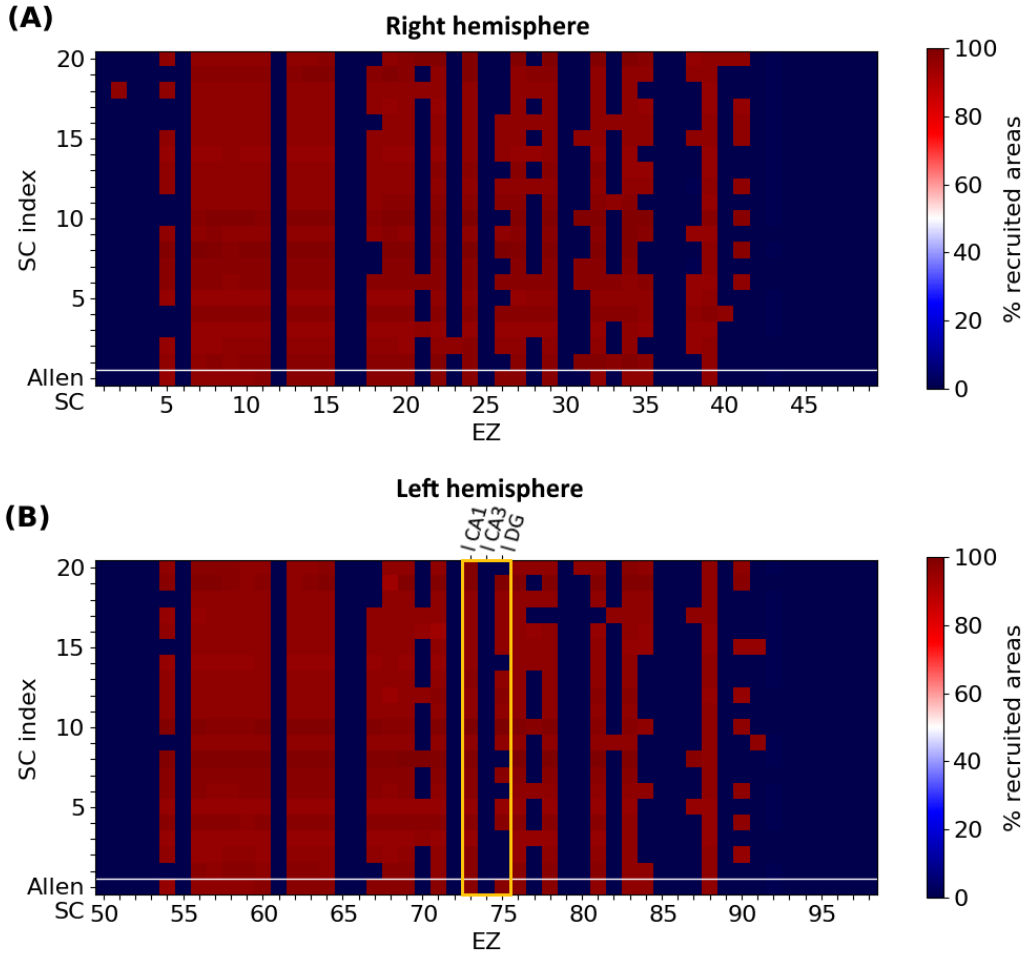

Figure III.4: **Localized and widespread epileptic seizure for different structural connectomes.** We simulated epileptic seizures for the original mice brain connectome (Allen SC, first row of each panel) and for different randomly generated SC matrices (separated by the white horizontal line). **(A)** Right hemisphere and **(B)** left hemisphere. Certain nodes generate exclusively localized or widespread while for some EZ areas the type of the seizure depends on the SC matrix. The yellow frame in panel **(B)** highlights the three nodes comprising the left hippocampal network. Note that our simulations generated either localized seizures (no widespread propagation at all or limited up to only two regions) or widespread seizures (reaching almost all brain areas).

seizure propagation using different SC matrices (initiated at different EZ regions of the Allen atlas). Each panel depicts different combinations of their respective graph connectivity measurements, namely their normalized eigenvector centrality, out-degree, average shortest path length, and the strongest outgoing connection weights. Each point in these plots displays the connectivity properties of a single EZ, and the percentage of brain areas affected during the seizure propagation initiated at this particular EZ. By means of these graph connectivity measurements, we were able to identify three distinct regions delineated by the following thresholds: all EZ whose strongest outgoing connection has a weight value larger than $w_{\text{upper}} = 0.31$ produced widespread seizures, while all EZ whose strongest outgoing connection has a weight value lower than $w_{\text{lower}} = 0.22$ only produced localized seizures. EZ nodes with values in-between these two values resulted to either localized or widespread seizures (see **Figures** III.5 (A)-(D)).

The eigenvector centrality, out-degree and average shortest path length might also be relevant properties to infer on the node's (in-)ability to produce a widespread seizure. Clusters of nodes with relatively low average shortest path length value and high eigenvector centrality value ($L_i < 0.97$, $x_i > 0.30$) can systematically produce widespread seizures. On the other hand EZ areas with relatively high average shortest path length value and low eigenvector centrality value result to localized seizures (see cluster near the area with $L_i > 0.98$, $x_i < 0.20$ in **Figure** III.5(D)).

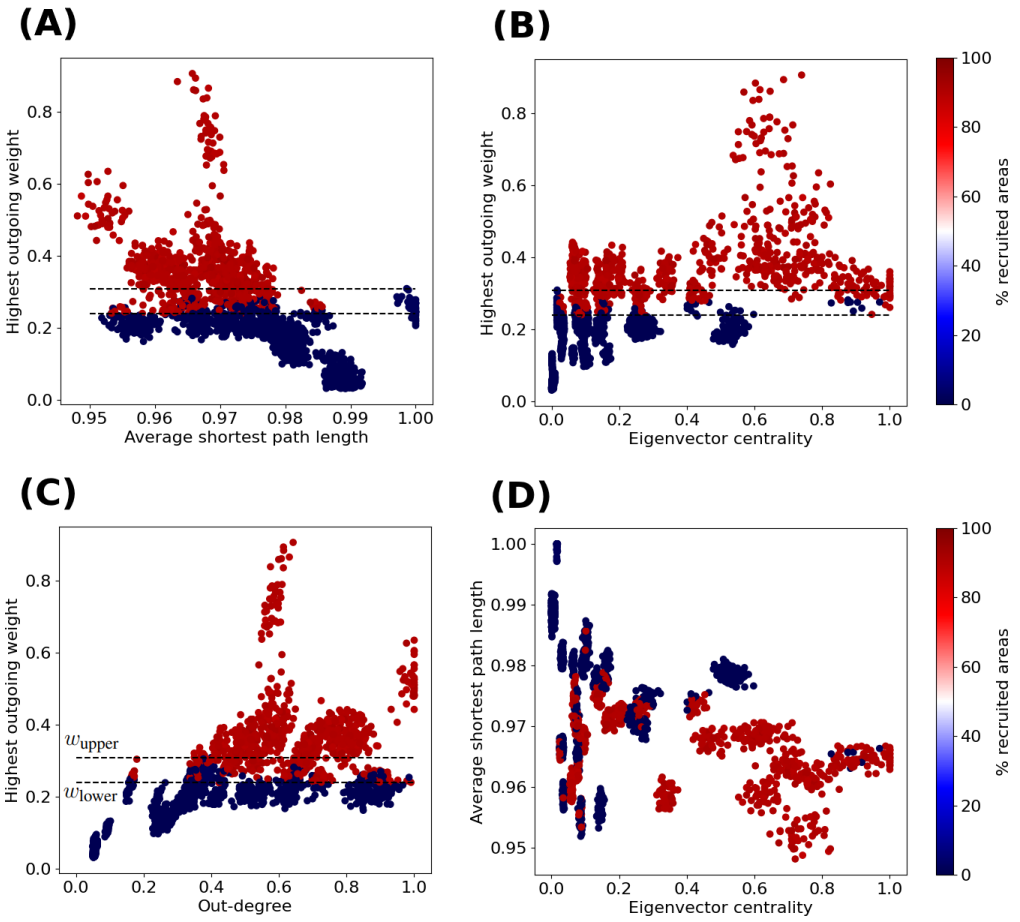

Figure III.5: **Widespread vs localized epileptic seizures and EZ graph network connectivity measurements.** We calculated the normalized average shortest path length, eigenvector centrality and out-degree for each node of the original Allen SC and the 20 additional randomized connectomes (98 nodes per SC matrix). The colormap indicates the fraction of brain areas of a seizure propagation when it is initiated at the respective EZ region (i.e., the points depicted in the plots). Each panel depicts different combinations of their respective graph connectivity measurements, namely the normalized average shortest path length vs the strongest outgoing connection weights **(A)** the eigenvector centrality vs the strongest outgoing connection weight **(B)**, the out-degree vs he strongest outgoing connection weight **C)** and the normalized eigenvector centrality vs the average shortest path length **(D)**. The upper (resp. lower) horizontal dashed line shows the aforementioned thresholds w_{upper} (resp. w_{lower}) of the larger outgoing edge weight (see text for more details).

3 Propagation control of Hippocampus-initiated widespread epileptic seizures

3.1 Connectivity of the hippocampal subnetwork

The hippocampus is a well-known EZ in Temporal Lobe Epilepsy (Toyoda *et al.* 2013; Buckmaster *et al.* 2022). In this chapter, we investigate seizure propagation and confinement when seizure initiation occurs in the different areas of the hippocampus. In the Allen mice brain atlas, the hippocampal subnetwork is composed of three nodes, namely the CA1, CA3 and Dentate Gyrus areas (see **Figure** III.2 and the discussion earlier of **Figure** III.4). In **Figure** III.6(A), we show the hippocampal subgraph. The color of each connection indicates its weight. The hippocampal subnetwork exhibits strong connections within left (resp. right) hippocampus itself, and between left and right hippocampus. The weights of the strong outgoing connection of the left-field CA1 ($w_{\text{l CA1}} = 0.36$), left-field CA3 ($w_{\text{l CA3}} = 0.18$) and left Dentate Gyrus ($w_{\text{l DG}} = 0.25$) strongest outgoing connection are such that $w_{\text{l CA1}} > w_{\text{upper}} > w_{\text{l DG}} > w_{\text{lower}} > w_{\text{l CA3}}$. More precisely, the left-field CA1 lies within the connectivity area of widespread seizure production as presented in **Figure** III.5. Left DG also lies within the region of potential widespread seizure production, while left-field CA3 is in the region of local seizure production. Note that moreover, CA3 has no strong outgoing connection (with weight higher than 0.1) outside the hippocampus, contrary to left-field CA1 and left Dentate Gyrus. In particular, both left-field CA1 and left Dentate Gyrus present edges leading to left Entorhinal Cortex, lateral part (l ENTl) and left Subiculum (l SUB).

3.2 Widespread prevention by edge removal

In order to control wide spread brain seizure propagation, we experimented with two different interventions on the structural connectome to computationally simulate the effects of two clinical approaches for epilepsy. First, we applied *graph edge removal* from relevant EZ nodes to (loosely) simulate a resection-like surgery intervention. Our ultimate goal here is to suppress the communication pathways between certain brain areas which are involved in a widespread seizure by blocking the minimum amount of edges potentially relevant to the propagation. When we remove a given connection from node i to node j, we set its new weight value in the adjacency matrix to zero and we re-normalize all weights' values to one (Melozzi *et al.* 2017; Jehi 2018; Rubio *et al.* 2019; Alexandratou *et al.* 2021). We use the notation $i \nrightarrow j$. We use the latter analysis to computationally test the effect of different edge resection options in the original mice brain network on seizure propagation.

3.2.1 Left-field CA1

Figure III.6 shows the impact of several connections' removal on the propagation (widespread vs localized) of focal seizures starting in left-field CA1 area. Each upper left panel depicts the modified brain network and the hippocampal subnetwork, with crosses (when present) indicating the removed connections between two or more nodes. Note that for better visualization, we only show connections of weight higher than 0.1. The color of the connections indicates their respective weight values (see also the SC matrix in **Figure** III.2). Each lower left panel in **Figure** III.6(A), illustrates the hippocampus subnetwork and more particularly the left extra-hippocampal connections and their weights values are given in the left colorbar. Each right panel shows the time distance from seizure initiation in each node of the brain network on the Allen mice brain template. The seizure onset takes place at the dark red region while the end of its propagation at the regions in dark blue. **Figure** III.6(A) shows the reference focal seizure initiated in the left hippocampal region and its propagation in the original Allen mice brain connectome. After initiating in left-field CA1, the seizure reaches left-field CA3, then right-field CA3, and propagates rapidly (almost simultaneously) in both hemispheres. The seizure spreads in the left and right hemispheres due to the strong inter-hemispheric hippocampal connections. In **Figure** III.6(B), we remove the strongest connection leading from the EZ to the right hemisphere, that is l CA1 $\nrightarrow$ r CA3. Hence, we prevent direct seizure propagation from left to right hippocampus. However, even by doing so, the seizure still spreads eventually into the entire brain network via the left hemisphere following a different evolutionary path and brain areas recruitment sequence. Next, we proceed by following an alternative approach, i.e. we remove a strong connection leading from the EZ to another area of the left hippocampus, namely left Dentate Gyrus. This approach results to a seizure which resembles the activity observed in **Figure** III.6(A), namely it reaches both hemispheres. However the propagation turns out to be relatively delayed, longer localized within the left hemisphere before spreading to the right one. In **Figure** III.6(D), we present a resection strategy (*Case I*) where we block both inter-hemispheric and intra-hemispheric communication pathways, namely l CA1 $\nrightarrow$ r CA3 and l CA1 $\nrightarrow$ l DG. This approach results to a localized seizure in the vicinity of the EZ area. In **Figure** III.6(E), we remove the left intra-hippocampal pathway l CA1 $\nrightarrow$ l DG and search for removal options within the right hippocampus instead of removing inter-hemispheric edges. We find one candidate connection that prevents widespread seizure propagation when being removed, namely the r CA3 $\nrightarrow$ r CA1 (*Case II*). In **Figure** III.6(F), we show that the resection of the strongest connection l CA1 $\nrightarrow$ l CA3 (*Case III*) is sufficient to prevent the seizure from spreading to any other area. Note that this is the single EZ outgoing connection with weight higher than the threshold w_{upper} identified in **Figure** III.5.

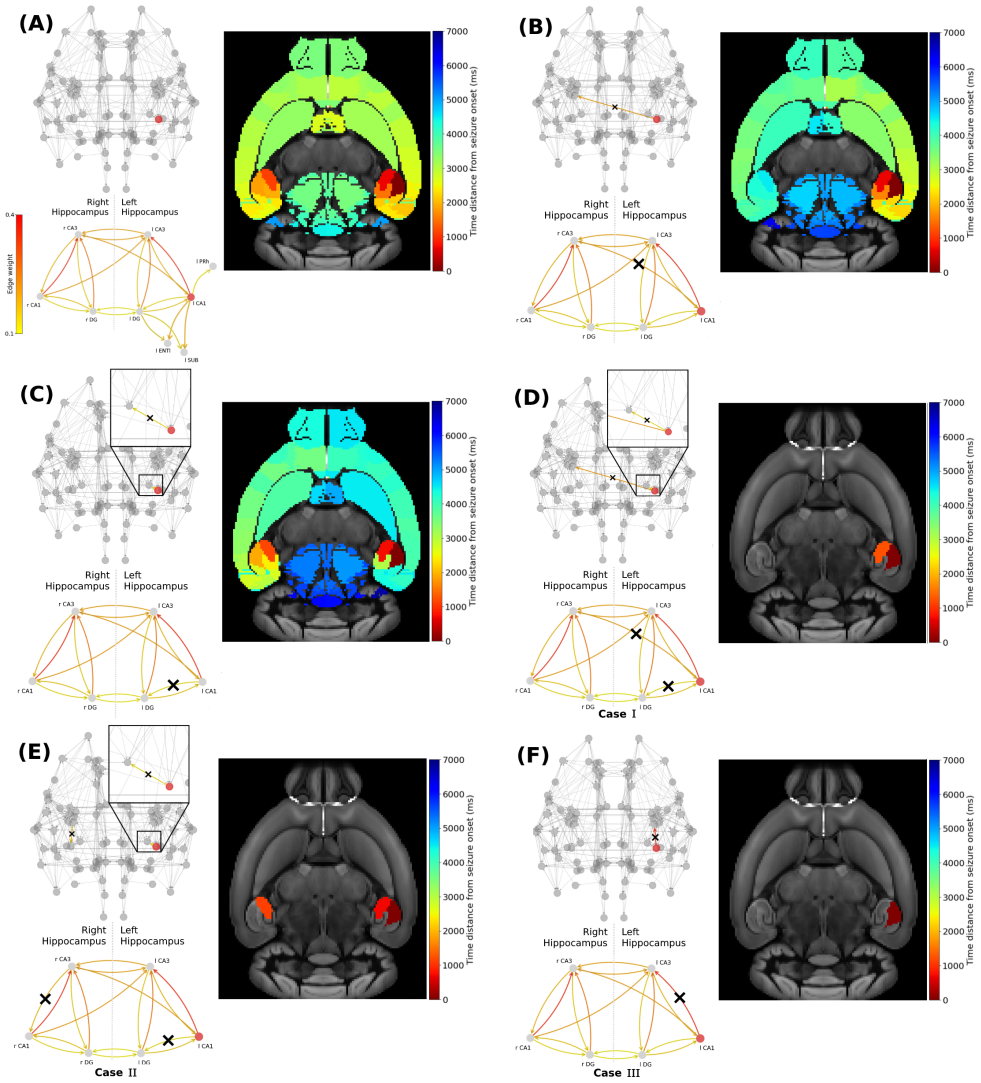

Figure III.6: **Widespread seizure prevention by edge removal in the left-field CA1.** The upper left panels show the whole brain network the hippocampal subnetwork. Crosses indicate the removed connections, and the edges' color shows their respective weight. The lower left panels illustrate the left extra-hippocampal connections and their weights values are given in the left colorbar. The right panels show the time distance between seizure initiation in the EZ (left-field CA1) and its onset in each brain area. Panel **(A)** shows an example of a widespread focal seizure propagation in the original Allen connectome, then after removing the inter-hemisphere strong connection **(B)** l CA1 $\nrightarrow$ r CA3, a strong connection within the left hippocampus **(C)** l CA1 $\nrightarrow$ l DG, the inter-hemisphere strong connection and within the left hippocampus **(D)** l CA1 $\nrightarrow$ r CA3 and l CA1 $\nrightarrow$ l DG, allowing inter-hemisphere communication but blocking a strong within the left and right hippocampus **(E)** l CA1 $\nrightarrow$ l DG and r CA3 $\nrightarrow$ r CA1 and blocking the strongest connection and within the left hippocampus **(F)** l CA1 $\nrightarrow$ l CA3.

3.2.2 Left Dentate Gyrus

Next, we conduct a similar analysis with epileptogenic left Dentate Gyrus and show the results in **Figure** III.7. After initiating a seizure in left Dentate Gyrus, it spreads to the left hemisphere via left-field CA3 then left-field CA1, and to the right hemisphere via right-field CA3 (see **Figure** III.7(A)). In **Figure** III.7(B), we show that the removal of a strong pathway between the EZ and the right hemisphere hippocampus l DG $\nrightarrow$ r DG has a weak impact on the seizure widespread propagation. In **Figure** III.7(C), we show that the removal of a strong connection leading from the EZ to other within the left-hippocampal areas l DG $\nrightarrow$ l CA1 results in a delayed widespread seizure propagation indicated by the blue color on the template. Then, we present three examples that yield to seizure localization. Namely, in **Figure** III.7(D) we removed strong connections between the EZ and another left-hippocampus area, and between left and right hippocampus. l DG $\nrightarrow$ l CA1 and l DG $\nrightarrow$ r DG (*Case I'*). In **Figure** III.7(E) we removed strong connections leading from the EZ to other parts of the left hippocampus and from right-field CA3 to other parts of the right hippocampus l DG $\nrightarrow$ l CA1 and either r CA3 $\nrightarrow$ r DG or r CA3 $\nrightarrow$ r CA1 (*Case II'*). And finally in **Figure** III.7(F) we removed the strongest connection l DG $\nrightarrow$ l CA3 (*Case III'*). We have also experimented with other similar effective strategies for focal epilepsy localization that can be found in the Supplementary Material (**Figure** A.3).

3.2.3 Percentage of recruited brain areas

In **Figures** III.6 and III.7, we illustrated the result of the aforementioned edge removal approaches using the original Allen mouse brain connectome. In order to further validate our findings, we also ran simulations with the additional SC matrices generated by the original Allen SC matrix as describe on the Materials and Methods section. By doing this, we aimed to improve the statistical significance of our results. **Figure** III.8 shows the percentage of recruited areas when applying the latter resection options to the different connectomes, where the left-field CA1 (**Figure** III.8(A)) and left DG (**Figure** III.8(B)) is the EZ respectively. In both cases, the single resection of EZ $\nrightarrow$ l CA3 (*Case III* and *III'*) is sufficient to achieve seizure confinement in the EZ in all connectomes. Starting with the left-field CA1 as an EZ, in **Figure** III.8(A), we show that removal edge *Case I* (second column, l CA1 $\nrightarrow$ r CA3 and l CA1 $\nrightarrow$ l DG, see **Figure** III.6(D)) and *Case III* (forth column, l CA1 $\nrightarrow$ r CA3 and l CA1 $\nrightarrow$ l DG, see **Figure** III.6(F)) approaches systematically prevent seizure widespread propagation for all SC matrices. Removal edge *Case II* (third column, l CA1 $\nrightarrow$ l DG and r CA3 $\nrightarrow$ r CA1, see **Figure** III.6(E)) effectively prevents widespread seizure propagation for 18 out of the 20 SC matrices. In **Figure** III.8(B), we present a similar analysis when the EZ is now the left Dentate Gyrus area and when implementing the edge removal *Case I'* (**Figure** III.6(D)), *Case II'* (**Figure** III.6(E)) and *Case III'* (**Figure** III.6(F)). The first two resulted in widespread seizure propagation for 18 out of the 20 SC matrices while the latter one

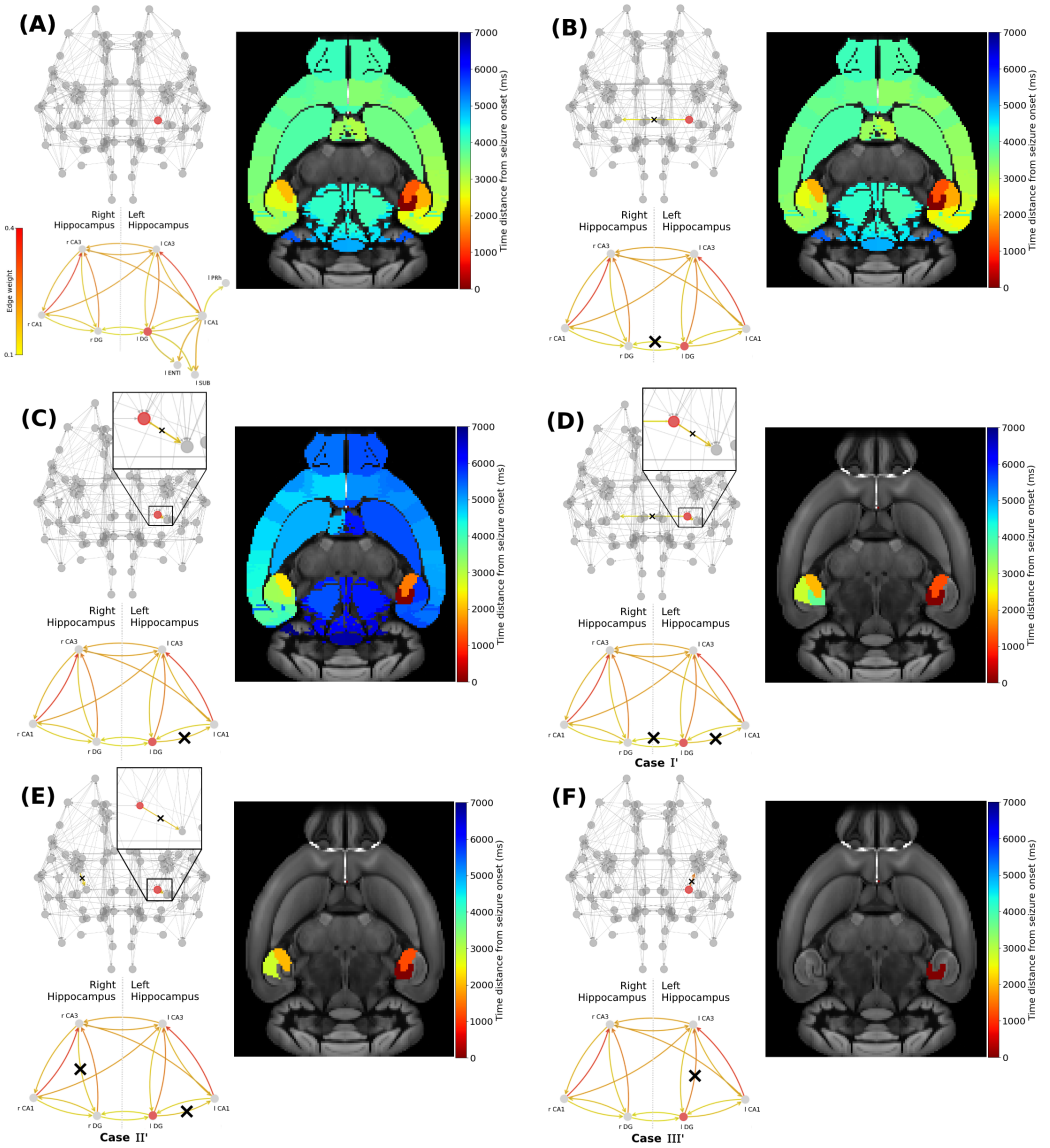

Figure III.7: **Widespread seizure prevention by edge removal in the left DG.** The upper left panels show the whole brain network the hippocampal subnetwork. Crosses indicate the removed connections, and the edges' color shows their respective weight. The lower left panels illustrate the left extra-hippocampal connections and their weights values are given in the left colorbar. The right panels show the time distance between seizure initiation in the EZ (left-field CA1) and its onset in each brain area. Panel **(A)** shows an seizure propagation in the original Allen connectome. Following a similar approach in removing graph edges (inter-hemisphere and/or within the left/right hippocampus) we gradually proceed by removing **(B)** l DG $\nrightarrow$ r DG, **(C)** l DG $\nrightarrow$ l CA1, **(D)** l DG $\nrightarrow$ r DG and l DG $\nrightarrow$ l CA1, **(E)** l DG $\nrightarrow$ l CA1 and r CA3 $\nrightarrow$ l DG and **(F)** l DG $\nrightarrow$ l CA3.

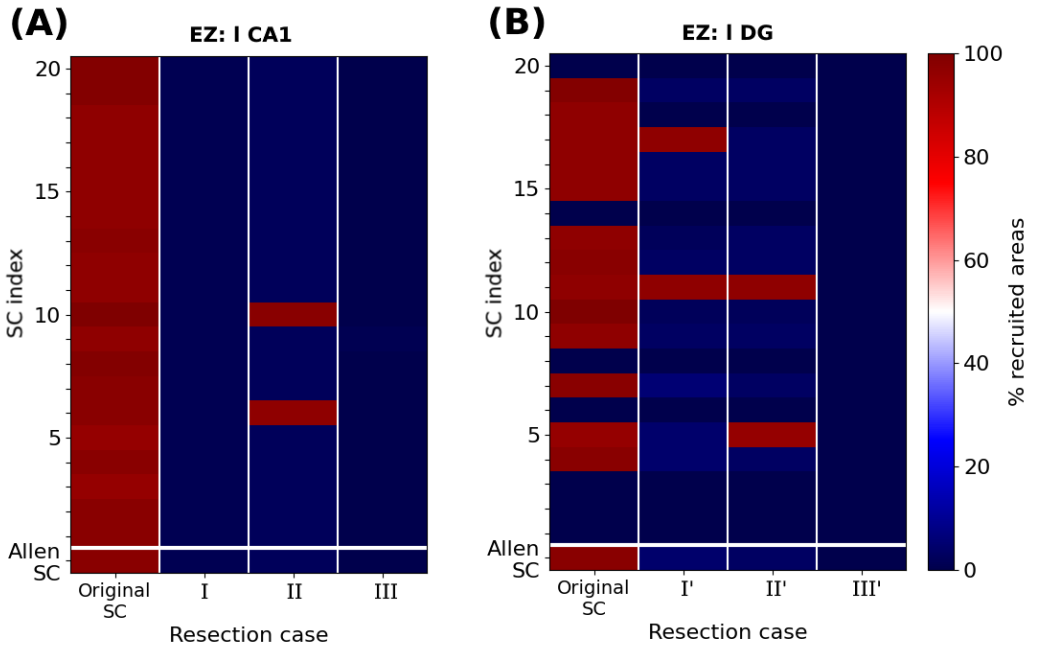

Figure III.8: **Percentage of recruited areas after edge removal for different mice connectomes. (A)** Simulations of a focal epileptic seizure initiated in the left-field CA1 area for the original SC Allen weight matrix (first row) and 20 additional SC ones (see text for more details), The first column (dark red) shows the robustness of the finding presented in **Figure** III.6 (A), i.e. that the left-field CA1 area generates systematically widespread seizures. Removal edge *Case I* and *III* approaches both systematically yield seizure localization (dark blue) while in *Case II* two connectomes (red color) yield to widespread seizure propagation and the rest to localized (blue color). **(B)** Simulations of a focal epileptic seizure initiated in the left DG area for the original SC Allen weight matrix and 20 additional SC ones and the edge removal *Case I', II'* and *III'* approaches (see **Figure** III.7).

to localized seizure for all connectomes.

3.3 Widespread prevention by outgoing edge weight reduction

3.3.1 EZ outgoing edge weight reduction

We focus on an EZ node and we perform a *global outgoing weight reduction* (by some percentage of the initial weight). This (rather simple) approach aims at loosely modeling a suppression of the hyperexcitability of the diseased brain area using for example neuromodulation techniques (Heck *et al.* 2014; Tsuboyama *et al.* 2020; Toffa *et al.* 2020) or the local effect a drug administered in the vicinity of the EZ area (Kanner & Bicchi 2022). To this end, we decreased the weight values of all outgoing connections from the EZ. Hence, the new weights are:

$$c'_{ij} = (1 - p).c_{ij}, \tag{III.3}$$

p being the percentage of reduction applied. After each of such weight modification, the structural connectivity is re-scaled to preserve its initial total connective strength. We restricted our analysis to the sole EZs left-field CA1 and left Dentate Gyrus regions as the left-field CA3 does not produces widespread seizures (see **Figure** III.4(B)).

Drugs and stimulation techniques are currently used (see the discussion in the Introduction section) to suppress neural hyperexcitability (locally or globally). Such interventions can alter the (short-term) synaptic and (long-term) structural connectivity and hence the weights in a given SC matrix which in turn affects functional activity, i.e. the FC matrix. Recently, a new hybrid connectome has been introduced (Ajilore *et al.* 2013), the so-called "resting-state informed structural connectome" (rsSC). These connectomes encode the standard SC (weight) matrices and the BOLD signal, i.e., the SC is "informed" by its respective FC. This approach implements an optimization algorithm whose maximum pseudolikelihood is constrained (via a penalty function) by the weight values of the SC matrix. The resulting rsSC incorporates co-activation (excitatory) or silencing (inhibitory) effects that ultimately allow to infer the excitation-inhibition between brain areas, see (Fortel *et al.* 2019; Fortel *et al.* 2020; Fortel *et al.* 2022; Fortel *et al.* 2023; Manos *et al.* 2023). Hence, a modification in (outgoing) weights in the SC is expected to affect the resting-state FC and therefore the rsSC, i.e. the excitability between certain brain regions (more details can be found in the Discussion section).

3.3.2 Percentage of recruited brain

The alternative procedure to prevent widespread seizure propagation aims to mimic the reduction of EZ hyperexitability with a global decrease of its outgoing weight, the extreme case of which would be the suppression of any EZ output. In terms of

connectivity measurements, outgoing weight reduction has a direct impact on the EZ's out-degree and the weight of its strongest outgoing edge, and by extension on its eigenvector centrality. To identify a minimal level of reduction one should apply to prevent seizure propagation, we perform simulations of an epileptic seizure starting in left-field CA1, then in left Dentate Gyrus, before any reduction and after the reduction of 10%, 20%, 30%, 40% and 50% of the EZ's outgoing edges weights.

Figure III.9 shows the percentage of recruited areas when applying the latter reductions on the different randomized connectomes. For a seizure starting in left-field CA1, the control gets efficient in most of the cases when reducing the EZ's outgoing weights of 30%. We achieve seizure confinement in all connectomes by reducing the EZ's outgoing weights of at least 40%. For a seizure starting in left Dentate Gyrus, confinement is achieved in all connectomes with a reduction of 10%.

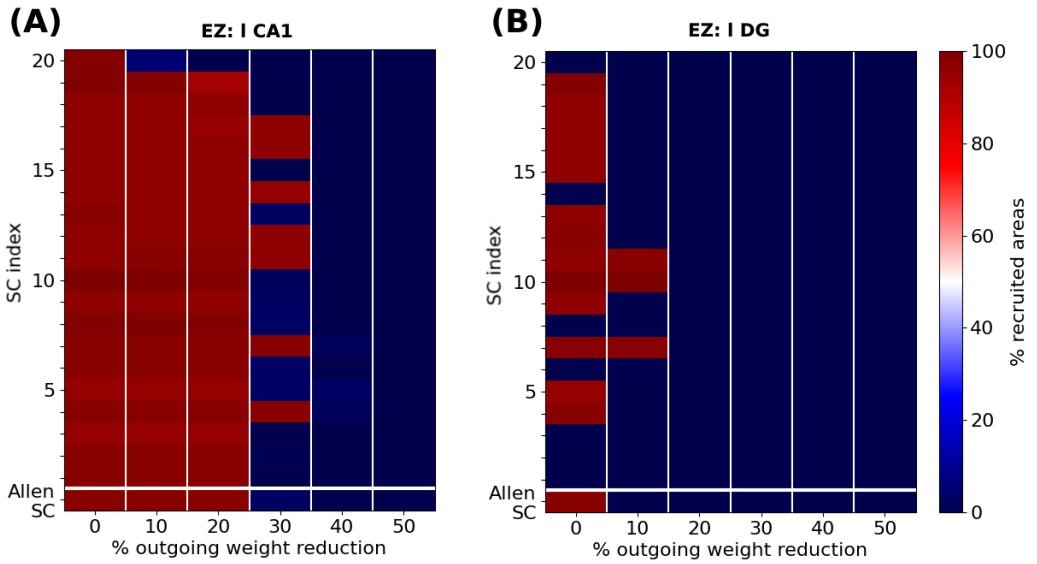

Figure III.9: **Percentage of recruited areas for different levels of outgoing weight reduction.** Simulations of a focal epileptic seizure initiated in **(A)** the left-field CA1 area for the original SC Allen weight matrix (first row) and 20 additional SC ones (see text for more details). Outgoing weight reduction of at least 40% systematically yields seizure localization (dark blue). **(B)** Simulations of a focal epileptic seizure initiated in the left DG area for the original SC Allen weight matrix and 20 additional SC ones. Outgoing weight reduction of at least 20% systematically yields seizure localization.

4 Impact of seizure control strategies on the brain structure

4.1 Connectivity of Hippocampal EZ

Finally, we show the effect of the latter resection and outgoing weight reduction strategies on the EZ's connectivity. **Figure** III.10 shows the eigenvector centrality and larger outgoing weight value of **(A)** left-field CA1 and **(B)** left Dentate Gyrus in the Allen connectome, before and after performing structural modifications. The horizontal dashed lines indicate the upper and lower threshold values for the larger outgoing weight ω_{upper} and ω_{lower} defining regions of widespread and local seizure production (see **Figure** III.5). The color of the nodes indicate the percentage of seizure-recruited areas in each scenario. Along the long diagonal arrow, we show from top to bottom the effect of the EZ outgoing weight reduction of: 0% (Original SC), 10%, 20%, 30%, 40% and 50%.

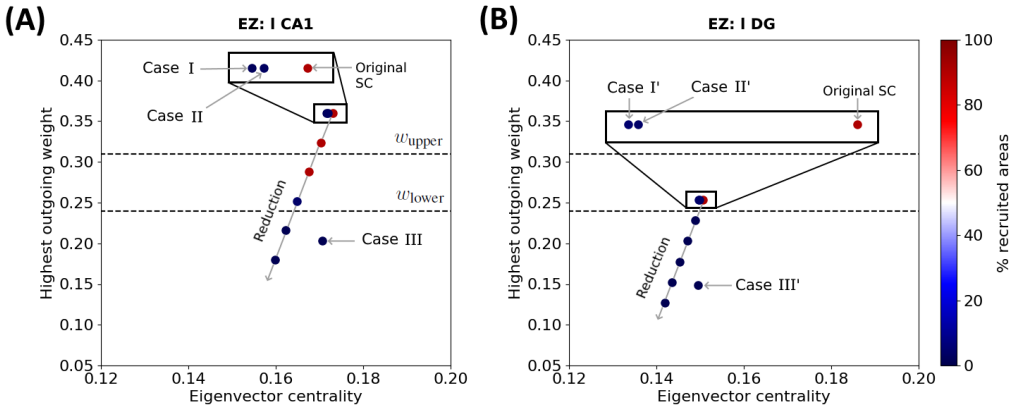

Figure III.10: **EZ connectivity and percentage of seizure-recruited areas after outgoing weight reduction and edge resection.** Each point shows the eigenvector centrality and the largest outgoing weight value in the Allen connectivity of **(A)** left-field CA1 and **(B)** left Dentate Gyrus, before and after applying outgoing weight reduction and edge removal strategies *Case I, II* and *III* (resp. *Case I', II'* and *III'*) as labelled in **Figure** III.6 and **Figure** III.7. The points aligned on the diagonal arrow represent, from top to bottom, an outgoing weight reduction of 0% (Original SC), 10%, 20%, 30%, 40% and 50%. The color of each point shows the percentage of recruited brain areas when the seizure starts in the corresponding node. The two dashed lines show the upper (resp. lower) threshold of the largest outgoing weight from separating the widespread from localized seizures.

4.1.1 Left-field CA1

In **Figure** III.10(A), we present the effects of edge removal approaches *Case I* (l CA1 $\nrightarrow$ r CA3 and l CA1 $\nrightarrow$ l DG), *Case II* (l CA1 $\nrightarrow$ l DG and r CA3 $\nrightarrow$ r CA1)

and *Case III* (l CA1 $\nrightarrow$ l CA3) for the left-field CA1 area and only for the original Allen SC Matrix. When applying outgoing weight reduction, the progressive decrease of the EZ's outgoing connective strength leads its connectivity towards lower eigenvector centrality values, and especially lower strongest outgoing weight values. The approach *Case III* also results in reducing the EZ's strongest outgoing weight to value below ω_{lower} threshold. Note that EZ nodes with outgoing weight values lower than ω_{lower} yield to seizure localization. The edge removal approaches *Case I* and *II* also mildly reduce the EZ's eigenvector centrality, and lead to seizure localization without any modification of its strongest outgoing connection.

4.1.2 Left Dentate Gyrus

In **Figure** III.10(B), we present the effects of the edge removal approaches *Case I'* (l DG $\nrightarrow$ r DG and l DG $\nrightarrow$ l CA1), *Case II'* (l DG $\nrightarrow$ l CA1 and r CA3 $\nrightarrow$ r DG) and *Case III'* (l DG $\nrightarrow$ l CA3) for the left Dentate Gyrus and same connectome. The overall trend is again similar, namely focal seizures remain localized as the outgoing weight value of the node decreases after our intervention and crosses the lower threshold (lower dashed line). Note that *Case III'* has a strong impact in reducing the strongest outgoing connection weight in left Dentate Gyrus while resections *Cases I'* and *II'* cause an eigenvector centrality value reduction. A similar Figure with all SC matrices and analysis can be found in the Appendix section (**Figure** A.4).

4.2 Resting-state Functional Connectivity

We used functional analysis to evaluate time correlation between spatially distant brain areas' activity. We do not manage to observe notable difference between the FC produced by the original SC matrix and the FC matrices produced with the different intervention procedures introduced in sections III.3.2 and III.3.3. The detailed procedure and results are presented in the Appendix section, see **Figure** A.5.

Discussion

In this chapter we employed the Epileptor model to simulate widespread and localized epileptic seizures (**Figures** III.1 and III.3) and investigate the relationship between the location of an EZ, its connectivity graph significance in the network (**Figures** III.4 and III.5), and the widespread propagation of such seizures in a mouse brain structural connectome (**Figure** III.2). When initiating focal seizures within the three hippocampal sub-regions (from the Allen atlas) we observed that the left-field CA1 area systematically generates widespread seizures, the left-field CA3 systematically generates localized seizures, and left Dentate Gyrus can generate both widespread and localized seizures, depending on the SC weight matrix (**Figures** III.4).

Our next objective was to identify plausible and effective strategies that are able to prevent widespread seizures. To achieve that, our first approach (**Figures** III.6 and III.8) was to selectively remove a minimal amount of EZ node edges (targeted disruption of specific network connections). Instead of adopting the approach of computationally "resecting' the entire EZ tissue from both brain hemispheres and as performed in surgical settings (see e.g., (Jirsa *et al.* 2016; Melozzi *et al.* 2017; An *et al.* 2019; Olmi *et al.* 2019; Nissen *et al.* 2021)), here we aimed to systematically identify and eliminate (or block) the minimal set of connections necessary to prevent generalised seizures. In our second approach (**Figures** III.7 and III.9), we attempted to computationally (and somewhat loosely) model the impact of a drug (Kanner & Bicchi 2022) or a neuromodulation approach (suppression of network hyperexcitability) in the vicinity of an EZ region (see e.g. (Tsuboyama *et al.* 2020)). Therefore, we adjusted the outgoing weight connections of an EZ node in our structural connectome to emulate the inhibitory effect of such a drug or external stimulation in the proximity of the targeted area around the EZ. In both approaches, our ultimate goal is to minimize the surgical or medical intervention while preserving as much as possible the pre-surgical original structural connectivity and brain functionality. Our findings indicate that strong inter and intra-hippocampal nodes' communication is important for the widespread seizure propagation. The successful (or not) outcome in preventing widespread seizure propagation can be computationally associated with a threshold value crossing of the larger weight outgoing of the EZ (left-field CA1 or left Dentate Gyrus) area caused by our interventions (in silico) as shown in **Figure** III.10 (see also **Figure** A.4 in the Appendix, where we show the results from SC matrices used for each approach).

The research into the structural organization of the brain has enhanced our understanding of the processing and integration of information through specialized neural circuits distributed across the brain. The application of current network theory to brain connectomes has played a crucial role in this advancement, revealing a set of universal organizational principles that govern brain connectivity. These principles seem to be consistent across different species and scales (see e.g., (van den Heuvel & Sporns 2019). In (Coletta *et al.* 2020), the authors used high-resolution mapping of the mouse axonal connectome to uncover novel foundational wiring principles in the mammalian brain, providing a detailed understanding of

how neural information is processed and transmitted across different spatial scales. They employed a voxel-level description which revealed organizational principles such as the directional separation of hub regions into neural sink and sources. In a next step, these findings could be taken into account for the graph analysis.

Computational studies have emerged as a powerful approach to advancing our understanding of seizure suppression mechanisms (Taylor *et al.* 2014), offering insights that bridge the gap between theoretical modeling and clinical intervention. A multitude of recent scientific articles have contributed to this burgeoning field. For instance, researchers have explored the potential of robust control strategies for deep brain stimulation in childhood absence epilepsy, as demonstrated in the work by (Rouhani *et al.* 2023). Utilizing real-world data, (Brogin *et al.* 2023) presented a computational framework for the identification and control of epileptic seizures, showcasing the applicability of computational methodologies to real-life scenarios. Furthermore, the prediction of seizure suppression effects through computational modeling has been exemplified by (Ahn *et al.* 2017), underlining the potential of simulation-based approaches in assessing treatment outcomes. Our work is a step forward into the understanding on how to optimize the impact of such stimulation.

Intricate dynamics of seizure termination and postictal EEG suppression have been uncovered through computational investigations, as highlighted by (Bauer *et al.* 2017), shedding light on the mechanisms governing convulsive seizures. The design of patient-specific neurostimulation patterns for seizure suppression has also been a subject of study, as evidenced by (Sandler *et al.* 2018), offering tailored solutions to individual patients. Additionally, the interplay between neural activity and ion concentration changes in localized seizures has been elucidated by (Gentiletti *et al.* 2022), stressing the critical role of computational methods in deciphering complex neurophysiological processes. Nowadays there are already several devices (approved by the U.S. Food and Drug Administration) aiming to reduce the frequency of seizures, namely Vagus Nerve Stimulation (VNS), Responsive Neurostimulation (RNS), and Deep Brain Stimulation (DBS) (see (Skrehot *et al.* 2023) and references therein for a recent review). Here again the weight decrease may give a hint on the location of the stimulation efficiency.

The clinical significance of epileptic seizure propagation lies primarily in the fact that the epileptic manifestations cannot be solely attributed to the activity within the seizure focus itself; rather, they result from the spread of epileptic activity to other brain structures. Propagation, particularly when leading to secondary generalizations, poses a significant risk to patients, including recurrent falls, traumatic injuries, and unfavorable neurological outcomes. Anti-seizure medications (ASMs) exert diverse effects on propagation with varying potencies. Notably, for individuals resistant to drugs, targeting seizure propagation may enhance quality of life even without a substantial reduction in simple focal events (see e.g. (Brodie *et al.* 2016; Khateb *et al.* 2021).

Network hyperexcitability is a potential contributor to cognitive dysfunction in individuals also with Alzheimer's disease (AD). In AD patients, hyperexcitability and epileptiform activity are frequently observed and have been linked to impaired

cognitive function. Studies conducted on transgenic mouse models of AD in preclinical settings have shown that suppressing epileptiform activity with anti-seizure drugs is associated with improved behavior and a reduction in histopathological indicators of chronic network hyperexcitability in the hippocampus. Drugs such as Levetiracetam (LEV) are commonly used as anti-seizure medication and have been reported to effectively suppress epileptiform spikes and enhance synaptic and cognitive function in mouse models of AD. Moreover, LEV is currently undergoing human trials (in both adults and children) for the treatment of seizures and long-term epilepsy, as indicated by research studies such as (Vossel *et al.* 2021) and (Onos *et al.* 2022).

The intricate interplay between excitation and inhibition is fundamental to the proper functioning of neural circuits within the brain. The excitation-inhibition balance, characterized by the equilibrium between excitatory and inhibitory inputs onto neurons, plays a crucial role in shaping the structural connectivity between different brain areas (Bergoin *et al.* 2023). Changes in this balance have been linked to alterations in the strength of synaptic connections affecting the synaptic and structural plasticity, thereby influencing the overall network architecture and information processing capabilities of the brain. For instance, studies have demonstrated that an excessive excitation-inhibition ratio can lead to aberrant plasticity and altered synaptic weights, potentially contributing to conditions such as epilepsy (see e.g., (Huberfeld *et al.* 2007). Conversely, a decrease in excitation-inhibition balance has been associated with disrupted neural synchrony and impaired cognitive functions, highlighting the delicate nature of this equilibrium (Roopun 2008; Yizhar *et al.* 2011).

Recent research has focused extensively on understanding brain activity at a large scale using resting-state functional MRI (rs-fMRI). The conventional approach typically considers SC and FC separately. However, this oversimplification ignores the dynamic engagement of white matter tracts during specific tasks. A more refined concept, termed “resting-state informed structural connectivity" (rsSC), has been introduced to incorporate information from rs-fMRI and infer the dynamic white matter engagement specific to the brain’s state. The resulting rsSC, or resting-state informed structural connectome, reveals the structural network underlying observed rs-fMRI correlations. This approach detects alterations in rsSC community structure in diseased subjects compared to controls. Notably, the original setup does not infer the “directionality" of white matter tracts as either “excitatory" or “inhibitory." The incorporation of the co-activation (excitatory) or silencing (inhibitory) effects into a hybrid rsSC framework that can allow to infer the brain’s E-I balance can be found in (Ajilore *et al.* 2013; Fortel *et al.* 2019; Fortel *et al.* 2020; Fortel *et al.* 2022; Fortel *et al.* 2023) (see also (Manos *et al.* 2023) for a recent study demonstrating the advantages of using rsSC in modeling time series in whole brain dynamics).

The insights accumulated from computational studies pave the way for more targeted and effective approaches to managing epilepsy. From investigating the impact of spiking timing stimulation on frequency-specific oscillations (Quinarez *et al.* 2023) to exploring the potential of linear delayed feedback con-

trol in thalamocortical models (Zhou *et al.* 2020), these studies collectively contribute to an expanding body of knowledge that spans from the cellular level (Lu *et al.* 2017) to network dynamics (Depannemaecker *et al.* 2021). Moreover, the translation of computational findings into clinical practice has been deliberated upon by (Brinkmann *et al.* 2021), emphasizing the promising trajectory of computational seizure forecasting. As the field continues to grow, collaboration between computational neuroscientists and medical practitioners holds the potential to revolutionize our ability to suppress seizures and improve the quality of life for individuals living with epilepsy.

Moreover, similar simulations are already being used in computational studies as a tool during pre-surgical stages in the identification of epileptic zones for patients who undergo surgery, In (Makhalova *et al.* 2022; Jirsa *et al.* 2023), the authors employed a computational brain modeling method, the so-called Virtual Epileptic Patient (VEP), informed by stereoelectroencephalography (SEEG), and anatomical personalized data to simulate seizures in drug-resistant epilepsy patients. The retrospective analysis of 53 patients revealed that VEP demonstrated higher precision in detecting the EZ compared to clinical analysis and the overall prediction of seizure-free outcomes. However, these procedures are still in the early stages of clinical studies, have certain limitations and therefore require further follow-up investigation.

Our study has of course some limitations: First, our analysis was based on the Epileptor model and the Allen mouse atlas with a fixed granularity. To partially mitigate this we incorporated the generation of additional SC matrices to account for some variability and to enhance the statistical significance of our results. Moreover, we did not consider delays in our simulations and we kept all the model parameters and the external noise term fixed throughout our study. However, before choosing the epileptogenicity parameter value x_0 for the EZ regions, we carried out several simulations with other values relatively close to the chosen value and we found rather similar global seizure (widespread or localized) propagation effects to those reported in our manuscript. Nonetheless, in general, time delays can play a crucial role in the overall dynamics of the brain and its synchronous activity, as reported in the literature. For example, in (Petkoski & Jirsa 2019), the authors demonstrated that spatial heterogeneity of time delays is a crucial mechanism shaping the functional brain architecture. A similar analysis can be extended for a human connectome in the future. That is to investigate whether similar seizure onset conditions lead to similar types of seizure evolution and whether the intervention approaches we tested here are also effective to a human connectome (network). In this chapter we aimed to investigate how certain network graph properties (e.g. degree, eigenvector centrality and average shortest path length) were associated with a fixed brain structural connectome and different types of seizure propagation (focal versus generalized). We focused on computationally controlling the widespread propagation of seizures to improve the management of severe generalized epileptic seizures which affect both hemispheres and cause symptoms on both sides of the body. However, focal seizures are also important as they may cause motor, sen-

sory and cognitive problems for the patient (see e.g. the recent review articles by (Novak *et al.* 2022; Ghulaxe *et al.* 2023) and their study still requires further investigation.

Let us also stress that in this chapter we employed the phenomenological Epileptor model with a sole purpose to generate local seizure signals rather than to investigate detailed plausible physiological mechanisms related to seizure onset. We used these epileptic signals to computationally study their propagation in the other brain areas. There is currently an ongoing research activity in the improvement of such dynamical models. For example, recently in (Depannemaecker *et al.* 2022) the authors introduced a new model for epileptic seizures whose parameters can be associated with detailed cellular electrophysiological dynamics. The type of seizure propagation (local versus generalized) is mainly defined by the tractography, e.g. the weight connections between nodes and tract lengths associated with the delays in communication between nodes. Mild changes in the graph of the structural connectome can explain the differences in seizure type propagation (using the exact same model and parameters) or they can alter the overall dynamical activity and synchronization properties (see e.g. (Courson *et al.* 2023)). It is important to highlight that, at this point, our objective did not include comparing our simulated time series (or FC matrices) with experimental neuroimaging mouse signals. A relevant study addressing this aspect can be found in (Courtiol *et al.* 2020), where the authors employed the Epileptor model and appropriate parameters (such as global coupling and the bifurcation parameter) to characterize the resting state activity in both healthy and epileptic human subjects. Our work is largely computationally driven and, at this stage at least, may not immediately provide a direct therapeutic protocol for clinical implementations. However, we believe that it can shed some light on the subject and with follow-up studies help in gaining a better understanding of the underlying mechanisms leading to the onset of different types of seizures and their prevention.

Part IV

Multiscale simulation of seizures

Adapted from:

Thorsten Hater*, Juliette Courson, Han Lu*, Sandra Diaz Pier*, Thanos Manos.
Arbor-TVB: A Novel Multi-Scale Co-Simulation Framework with a Case Study on Neural-Level Seizure Generation and Whole-Brain Propagation.
DOI: https://doi.org/10.48550/arXiv.2505.16861. Under review.

A collaborative work with

* Jülich Supercomputing Centre, Forschungszentrum Jülich

Introduction

The human brain consists of billions of neurons and an equally vast population of non-neuronal cells, intricately organized into layers and regions (Herculano-Houzel 2009; Herculano-Houzel 2012). Each neuron operates as a highly sophisticated biochemical machinery (West *et al.* 2002; Augustine *et al.* 2003; Darnell 2013; Lu *et al.* 2025), coordinating signal transmission within an extensive network in health (Reyes 2003; Barral *et al.* 2019; Dicks 2022) and disease [see e.g., (Tetzlaff *et al.* 2025)]. Ever since the Hodgkin-Huxley model was introduced to describe membrane potential dynamics (Hodgkin & Huxley 1952a), computational neuroscience has played a pivotal role in enhancing our understanding of brain function. Yet, due to the immense complexity of the brain and computational constraints, most modeling studies focus on a single scale simulator or rely on standalone simulation codes.

Simulations incorporating biophysical properties and neural morphology typically concentrate on individual neurons using simulators such as the NEURON simulator (Carnevale & Hines 2006). At the microscopic level, studies have explored questions such as how the ion channel kinetics influence neural excitability [see e.g., (Gurkiewicz *et al.* 2011; Suma *et al.* 2024)], how proteins, enzymes, and calcium concentration are distributed among neighboring spines to impact plasticity [see e.g., (Luboeinski & Tetzlaff 2021; Chater *et al.* 2024)], and how signal propagation along axonal fibers relates to neuropathic pain [see e.g., (Tigerholm *et al.* 2014; Tigerholm *et al.* 2015)]. Some studies examine how neural morphology—such as dendritic tree growth [see e.g., (Yasumatsu *et al.* 2008)] and morphology-dependent plastic interactions [see e.g., (Hananeia *et al.* 2024)]—affects function. These studies, while often limited to small patches of the neural membrane, a few dendritic segments, or a small local network, provide valuable approximations of broader neural phenomena.

At the mesoscopic level, researchers simplify neuronal representations using point leaky-integrate-and-fire neurons (based on simulators such as NEST (Gewaltig & Diesmann 2007) or Brian/Brian2 (Stimberg *et al.* 2019)), enabling studies on larger networks without explicit neuronal morphology or with some degree of self-customized morphology, using e.g., NESTML (Linssen *et al.* 2024). This approach has advanced our understanding of neural heterogeneity (Demirtaş *et al.* 2019; Nayebi *et al.* 2021; Gast *et al.* 2024), self-organization (Zheng *et al.* 2013; Diaz-Pier *et al.* 2016; Miner & Triesch 2016), neural capacity (Emina & Kropff 2022), energy efficiency (Sacramento *et al.* 2015), and neural plasticity in disease and health (Manos *et al.* 2021; Lu *et al.* 2024). Most microscopic and mesoscopic models remain theory-driven, using mathematical approximations to infer neural behavior rather than directly establishing model based on large datasets [see e.g., (Popovych *et al.* 2019) for a recent review].

Data-driven modeling has gained traction at the macroscopic level with the rise of open-source brain imaging databases (such as OpenfMRI (Poldrack & Gorgolewski 2017)). High-resolution structural and functional data from magnetic resonance imaging and diffusion tensor imaging (DTI) enable whole-

brain modeling based on real anatomical features. Such type of models help to elucidate state transitions in brain activity and optimize external interventions to control brain states. The Virtual Brain (TVB) platform (Sanz-Leon *et al.* 2015; Sanz Leon *et al.* 2013; Ritter *et al.* 2013), for instance, integrates functional MRI and DTI datasets to build individualized models, using coupled oscillators to represent regional activity. TVB has contributed significantly to the understanding of neurological disorders and serves as a testing ground for therapeutic interventions [see e.g., (Stefanovski *et al.* 2021; Monteverdi *et al.* 2023; Courson *et al.* 2024) and references therein].

With advancements in computing resources and simulation technologies, integrating models across different scales has become both feasible and essential to strike a balance between retaining detailed information and achieving a broad-scale understanding. Recently, a co-simulation framework was introduced that employs NEST (a widely used simulator for point neurons and large neural networks) and TVB (broadly used and optimized for macroscale modeling of brain activity). This work has pioneered cross-scale modeling (Kusch *et al.* 2024) and has demonstrated the benefits of integrating models across spatial levels. Recently, (Schirner *et al.* 2022) provided a comprehensive overview of similar software tools available within the European digital neuroscience platform, EBRAINS. A notable application of TVB-Multiscale is the virtual deep brain stimulation model (Meier *et al.* 2022; Shaheen *et al.* 2022), demonstrating its utility in multiscale simulations.

However, integrating microscopic and macroscopic models remains technically challenging, especially when one is interested in modeling morphological details and large-scale brain dynamics at the same time, possibly in addition to creation/deletion of synaptic elements associated with neural plasticity mechanisms. At the core lies the vast amount of information being processed, billions of cells with thousands of connections each, and the immense gap in timescales, from microseconds in ion channel dynamics to minutes for plastic changes of the connectome. The holistic understanding on how such neural biophysical processes affect the whole-brain dynamics, could be leveraged, among other applications, in optimized development of pharmacological treatments and the assessment of neuromodulation or surgical interventions. By employing different temporal and spatial resolutions for independent parts of the simulation, it is possible to reduce the computational requirements. We employ the Arbor simulator (Akar *et al.* 2019) and more specifically its most recent next-generation version (Cumming *et al.* 2024). Designed for single-neuron and large-scale network simulations, Arbor leverages GPU resources to enhance computational speed and energy efficiency. A spike-based interface for co-simulation of biophysically detailed neuronal networks is provided.

In this chapter, we present a novel co-simulation framework integrating Arbor with TVB. In this first Arbor-TVB co-simulator implementation, our goal is twofold: first, to successfully establish efficient communication between the two simulators that respects their different operational time scales and, second, to provide a use case example of the combined neural activity. To this end, we use a mouse brain

connectome—a graph of arbitrarily sized brain regions interconnected by weights and tract-length values—where each region represents the mean mass neural activity of a brain area modeled by a macroscopic model. Both the connectome matrices and the region models are provided by TVB. Then, using the co-simulation interface we replaced one TVB node with a detailed neural network with detailed neurons using Arbor. This neural population allows the user to choose an available model or easily develop a new one in Arbor and to define the details in the local connectivity of the population. We generate locally activity similar to epileptiform seizures in the network of detailed cells and monitor their propagation in the brain connectome with TVB. In this proof-of-concept study, we use a Hodgkin-Huxley-based model (Depannemaecker *et al.* 2022) placed on a single compartment which allows us to simulate different types of neural activity (e.g., spiking, bursting, seizure-like, etc.) by controlling a single parameter value.

1 Co-simulation framework

1.1 Macro and micro-scale models

1.1.1 Single neuron and network models in Arbor

Arbor is an open-source library for building simulations of biophysically detailed neuron models (Akar *et al.* 2019). It provides an alternative to software like NEURON (Carnevale & Hines 2006), but with a strong emphasis on modern hardware and scalability to large-scale systems (Hines 1984). Its overall set of capabilities allows Arbor to model neural networks at a level of resolution beyond point models to explore phenomena like dendritic computation. Thus, support for bulk-synchronous parallelism via MPI, shared memory parallelism by utilizing a thread-pool and job system is central to Arbor, and certain cell types—primarily cable cells—can further leverage SIMD and GPU hardware. Arbor is written in $C{+}{+}$, though most users interface with it through an intuitive, high-level Python interface built on top of the lower level implementation. The underlying numerical model of Arbor is the cable equation:

$$c_{\mathrm{m}} V t = x\,(\sigma V x) + i_{\mathrm{m}} \tag{IV.1}$$

where the membrane potential V is computed over the morphological structure of the neural tree; the spatial coordinate x and derivative are to be understood within this structure (Von Helmholz 1850; Thompson & Kelvin 1855; Hodgkin *et al.* 1952; Hodgkin & Huxley 1952c; Hodgkin & Huxley 1952b; Loligo 1952; Hodgkin & Huxley 1952a; Scott 1975). The parameters c_{m} and σ define the membrane capacitance and longitudinal resistance. The transmembrane current density i_{m} models the entirety of ionic and non-ionic currents. In both NEURON and Arbor, these are calculated from user-specified sets of differential equations, potentially varying along the morphology. The equations for i_{m} and V are solved in alternation (Lie-Trotter splitting) using a first-order implicit method.

We begin by selecting a dynamical model that allows for relatively easy yet realistic simulation of a broad spectrum of neural activity at the single-neuron level, governed by a small set of biophysical parameters, see section I.4.3. The neural model from (Depannemaecker *et al.* 2022) was formulated for Arbor in the Neuron MODeling Language (NMODL). The following equations form the slow part of the system, describing the evolution of ion concentrations due to voltage-gated channels, active pumps, and buffering by an external bath see **Figure** IV.1(A) for a schematic of the dynamics. It describes the ionic exchanges between the intracellular and extracellular spaces (ICS, ECS) of a neuron immersed within an external bath, acting as a potassium buffer of concentration $\mathrm{K}_{\mathrm{bath}}$. Ions flow between the ICS and ECS through a sodium-potassium pump and the sodium, potassium and chloride voltage-gated channels, driving changes in the internal (K_i, Na_i, Cl_i) and external (K_o, Na_o, Cl_o) ionic concentrations. By gradually increasing the external bath concentration

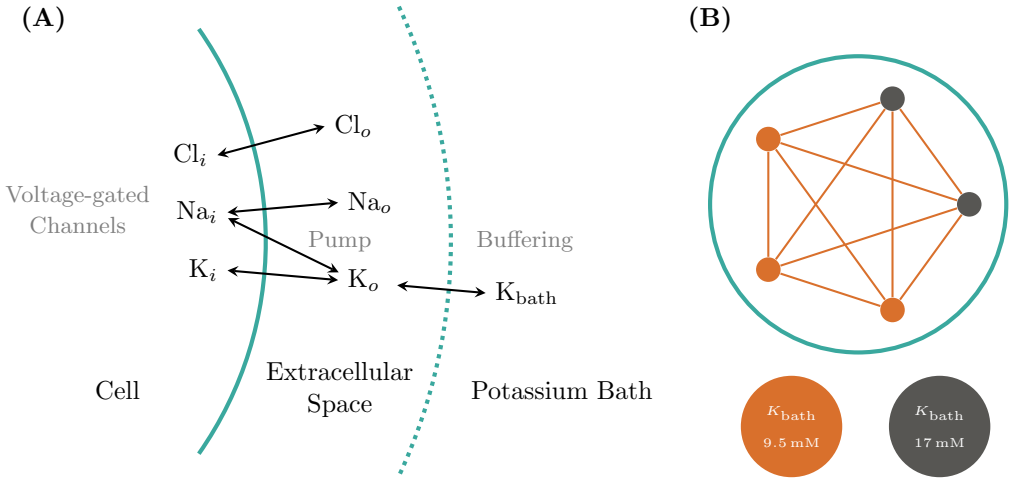

Figure IV.1: **Biophysical neuron model and Arbor network. (A)** For single cell dynamics three ion concentrations (K, Na, and Cl) are modeled in the cell's interior and a thin shell of its extracellular medium. The latter is, in turn, surrounded by a bath of a fixed Potassium concentration K_{bath}. The model simulates changes to the concentration in addition to the current contributions based on three voltage-gated ion channels, an active pump between Potassium and Sodium, and the buffering effect of the surrounding Potassium bath. **(B)** We choose typical values of K_{bath} for the single models to generate the tonic spiking (healthy) and seizure-like event (pathological) behaviors. In most cases, a fully connected network using exponential synapses with weight $w = 0.5$ is used. As an example, we show here the network instantiation for $N = 5$ and $f = 0.2$.

of potassium ions $\mathrm{K}_{\mathrm{bath}}$, the model sequentially presents these patterns: resting state (RS), spike train (ST), tonic spiking (TS), bursting, seizure-like events (SLE), sustained ictal activity (SIA) and depolarization block (DB), see **Figure** IV.2. The fast dynamics of the membrane potential V are modeled in Arbor via the cable equations, see above, which require computing the ion current densities i_{X} used in the simulator update as:

$$\begin{aligned} i_{\mathrm{X}} &= g_{\mathrm{X}}(V - E_{\mathrm{X}}) \\ E_{\mathrm{X}} &= C \cdot \log\left(\frac{\mathrm{X}_o}{\mathrm{X}_i}\right) \end{aligned}$$

with the ion species $\mathrm{X} = \{\mathrm{K}, \mathrm{Na}, \mathrm{Cl}\}$ and a non-ion current density:

$$i_{\mathrm{pump}} = \frac{\rho}{(1 + \exp(10.5 - 0.5\mathrm{Na}_i))(1 + \exp(5.5 - \mathrm{K}_o))}.$$

Following the Hodgkin-Huxley model, conductivities g_{X} are written as:

$$g_{\mathrm{K}} = g_{0,\mathrm{K}} n + g_{l,\mathrm{K}} \qquad g_{\mathrm{Na}} = g_{0,\mathrm{Na}} mh + g_{l,\mathrm{Na}} \qquad g_{\mathrm{Cl}} = g_{0,\mathrm{Cl}}$$

The — internal i and external o — ion concentrations are modeled as:

$$\begin{aligned} \mathrm{K}_i &= \mathrm{K}_{0,i} + \Delta\mathrm{K}_i & \mathrm{Na}_i &= \mathrm{Na}_{0,i} - \Delta\mathrm{K}_i & \mathrm{Cl}_i &= \mathrm{Cl}_{0,i} \\ \mathrm{K}_o &= \mathrm{K}_{0,o} - \beta\Delta\mathrm{K}_i + \mathrm{K}_g & \mathrm{Na}_o &= \mathrm{Na}_{0,o} + \beta\Delta\mathrm{K}_i & \mathrm{Cl}_o &= \mathrm{Cl}_{0,o} \end{aligned}$$

The variables $\{\Delta\mathrm{K}_i, \mathrm{K}_g\}$ evolve as:

$$\frac{d\Delta\mathrm{K}_i}{dt} = -\gamma\,(i_{\mathrm{K}} - i_{\mathrm{pump}}) \tag{IV.2}$$

$$\frac{d\mathrm{K}_g}{dt} = \varepsilon\,(\mathrm{K}_{\mathrm{bath}} - \mathrm{K}_o) \tag{IV.3}$$

where γ converts current density i_{X} to molar flux, summarizing the effect of the ion pump in **Figure** IV.1(A) and external buffer. Finally, fast dynamics were reduced and adjusted to mammalian neurons:

$$\begin{aligned} \frac{dn}{dt} &= \frac{1}{\tau}\,(n - n_\infty(V)) \\ n_\infty(V) &= \frac{1}{1 + \exp(-(19 + V)/18)} \\ m = m_\infty(V) &= \frac{1}{1 + \exp(-(2 + V/12))} \\ h = h(n) &= 1.1 - \frac{1}{1 + \exp(3.2 - 0.8n)} \end{aligned}$$

based on the observations that the reaction of the Sodium gating variable to changes in V is nigh instantaneous and $h(t) + n(t) = \text{const}$. The resulting ion channel was added to a basic, spherical, single-compartment neuron. After implementing this

biophysical model, we reproduced the firing patterns using the parameters of the reported model [**Figure** IV.2 (A-F)], see also (Depannemaecker *et al.* 2022) for more details and motivation for model parameter choices. Note that despite the values given in the original publication, neither the Arbor nor the published reference implementation produces the depolarization block pattern at $K_{\text{bath}} = 20\,\text{mM}$ but only at around $K_{\text{bath}} = 22.5\,\text{mM}$. From here, a simple model network was developed, comprising N total cells, with a mixture of healthy $f \cdot N$ and pathological $(1-f) \cdot N$ cells, where both sub-populations are assigned individual values for K_{bath}, sketched in Fig IV.1. Cells are connected using exponential synapses with an internal weight of $w = 0.5$ chosen to produce an activity similar to (Rabuffo *et al.* 2024) which uses delta synapses.

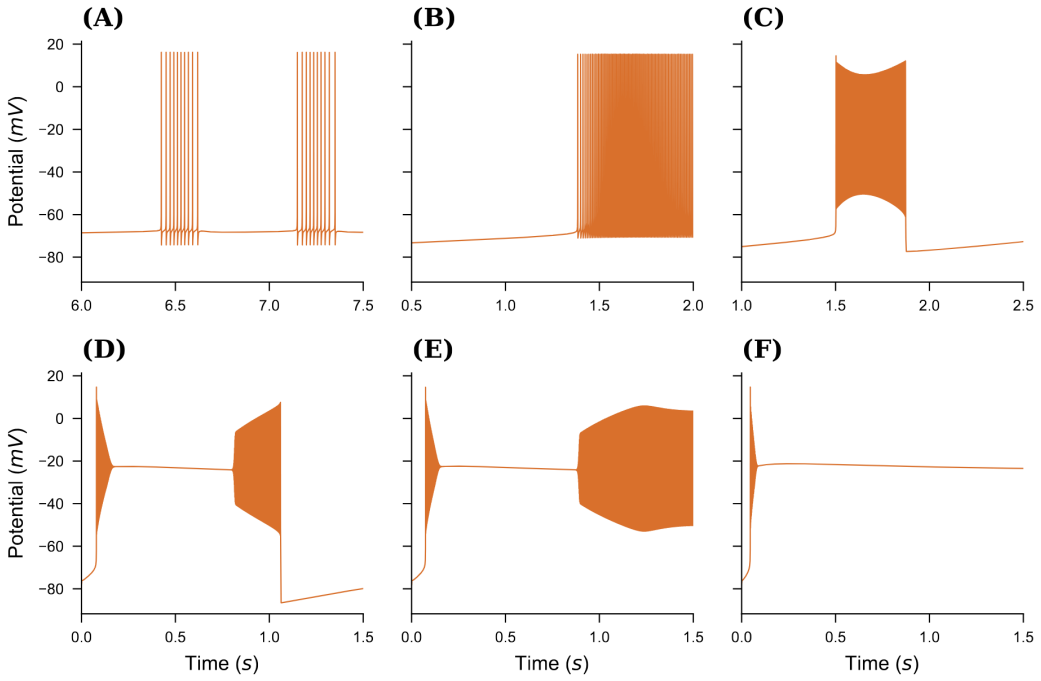

Figure IV.2: **Different neural spiking patterns.** **(A)** Spike Train, $\text{K}_{\text{bath}} = 7.5\,\text{mM}$, **(B)** Tonic Spikes, $\text{K}_{\text{bath}} = 9.5\,\text{mM}$, **(C)** Bursting, $\text{K}_{\text{bath}} = 12.5\,\text{mM}$, **(D)** Seizure Like Event (SLE). $\text{K}_{\text{bath}} = 17.0\,\text{mM}$, **(E)** Sustained Ictal Activity (SIA), $\text{K}_{\text{bath}} = 17.5\,\text{mM}$, and **(F)** Deolarization Block, $\text{K}_{\text{bath}} = 22.5\,\text{mM}$. Note that by setting $\text{K}_{\text{bath}} = 4\,\text{mM}$, one can obtain Resting State (RS) activity too (result not shown here).

1.1.2 TVB network model

Following (Deco *et al.* 2013), we used the reduced Wong-Wang model (Wang 2002) to simulate resting-state activity and to investigate the dynamics of local brain regions embedded within a large-scale brain network, see section I.4.1.3. The mean

firing rate $H(x_I)$ and mean synaptic gating variable S_I of region I are described by:

$$\frac{dS_I}{dt} = -\frac{S_I}{\tau_s} + (1 - S_I)\gamma H(x_I) \tag{IV.4}$$

$$H(x_I) = \frac{ax_I - b}{1 - \exp(-d(ax_I - b))} \tag{IV.5}$$

$$x_I = \omega J_N S_I + G J_N \sum_K c_{IK} S_K + I_0, \tag{IV.6}$$

with $\omega = 1$

the local excitatory recurrence, c_{IK} the strength of the structural connection from the local area I to K, and G a global coupling strength. The parameters are set to the same values used in the TVB implementation. $J_N = 0.2609\,\text{nA}$ is the synaptic coupling of NMDA receptors and $I_0 = 0.33\,\text{nA}$ is the baseline external input. The kinetic parameters are $\tau_s = 100\,\text{ms}$ and $\gamma = 0.641$. The parameters of the input-output function H are $a = 0.27\,\text{nC}^{-1}$, $b = 0.108\,\text{kHz}$, and $d = 154\,\text{ms}$. Depending on the tuning of G, the system exhibits a multi-stable regime, with steady states of high and low spiking activity. Here, we set $G = 0.096$.

1.2 Establishing the co-simulation framework

Both Arbor and TVB offer support for attaching a second simulator to perform co-simulation, potentially at different scales.

1.2.1 Co-simulation from TVB's point of view

Co-simulation from the TVB's viewpoint is the simpler technology of the two frameworks, since TVB is designed to execute as a single process. TVB allows for exchange of any variable relevant to the region models and any number of variables. The co-simulation partner is encapsulated in one or more TVB regions, called proxy nodes, see **Figure** IV.3(A). These proxies present a conforming interface to TVB; exchanging the salient variables as a table, one row per time-step, one column per variable. As TVB advances in lockstep on a global time-step, this is almost identical to normal operation. However, co-simulation introduces the concept of an *'epoch'* to TVB, i.e., the length of time that conforms to the smallest delay τ_{min} in the set of inter-region connections delays τ_{IJ}. These delays are part of the connectome data used to construct a TVB simulation. (In the case that a connectome contains vanishing delays these must be replaced with a finite value. Further, it is required that the time-step evenly divides τ_{min}.) Co-simulation thus can advance all nodes, including the proxy, for one epoch τ_{min} without exchanging data. This is correct as an event emanating from any region I at time t influences any other region J at time $t + \tau_{IJ} \geq t + \tau_{\text{min}}$. Only after an epoch, data need to be exchanged between the proxy and the rest of the TVB regions. A TVB–NEST demonstration has been published to showcase the interaction between a local network of spiking neurons

and the whole-brain network dynamics (Kusch *et al.* 2024).

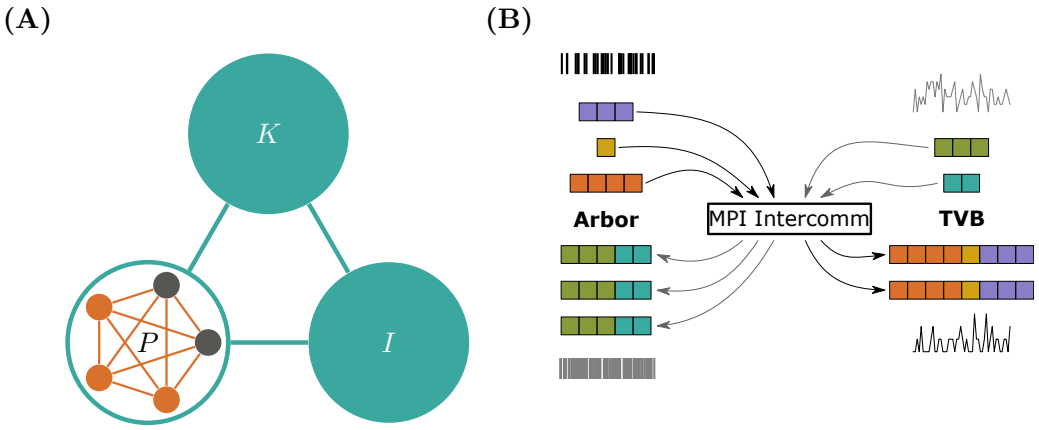

Figure IV.3: **Arbor-TVB co-simulation schematic and communication pattern. (A)** In a TVB simulation of regions I, K, and P; one region P will be replaced by a proxy containing a network of detailed cells simulated in Arbor. Regions are connected via the weights of the connectome and produce an activity values based on the chosen region model. When crossing the boundary between TVB and Arbor models, care needs to be taken to convert between discrete action potentials in Arbor to contiguous, region-model-specific variables in TVB. **(B)** Spikes generated by Arbor and TVB – converted from activity values interpreted as mean spiking rates – are exchanged using an MPI intercommunicator and the All-gather primitive. This is equivalent to concatenating all contributions from all Arbor MPI ranks and sending the result to all TVB ranks and vice-versa.

1.2.2 Co-simulation from Arbor's point of view

Arbor has a fundamentally different design in terms of connectivity. Interaction between physically separate cells is mediated by action potentials, which are triggered by dedicated sources, e.g., when the membrane potential crosses a configurable threshold. Cells are connected by wiring these sources to corresponding sinks like synapses via an abstract connection object comprising a delay and weight, modeling transmission and attenuation via an axon. In contrast to TVB, Arbor is fundamentally a distributed system and internally employs the same approach to decoupling via the minimum network delay as explained above. To initiate co-simulation, Arbor exposes an additional interface comprising the external connections, i.e., those terminating at cells managed by Arbor, but originating outside, and functionality to exchange spikes with Arbor. On the technical side, the latter part leverages `MPI_Allgatherv` through an inter-communicator and effects that the concatenation of all spikes sent from all MPI ranks running TVB arrive on all ranks running Arbor and vice versa [**Figure** IV.3(B)]. This allows co-simulation in conjunction with arbitrary numbers of ranks on both sides and even in compounds with more than two simulators.

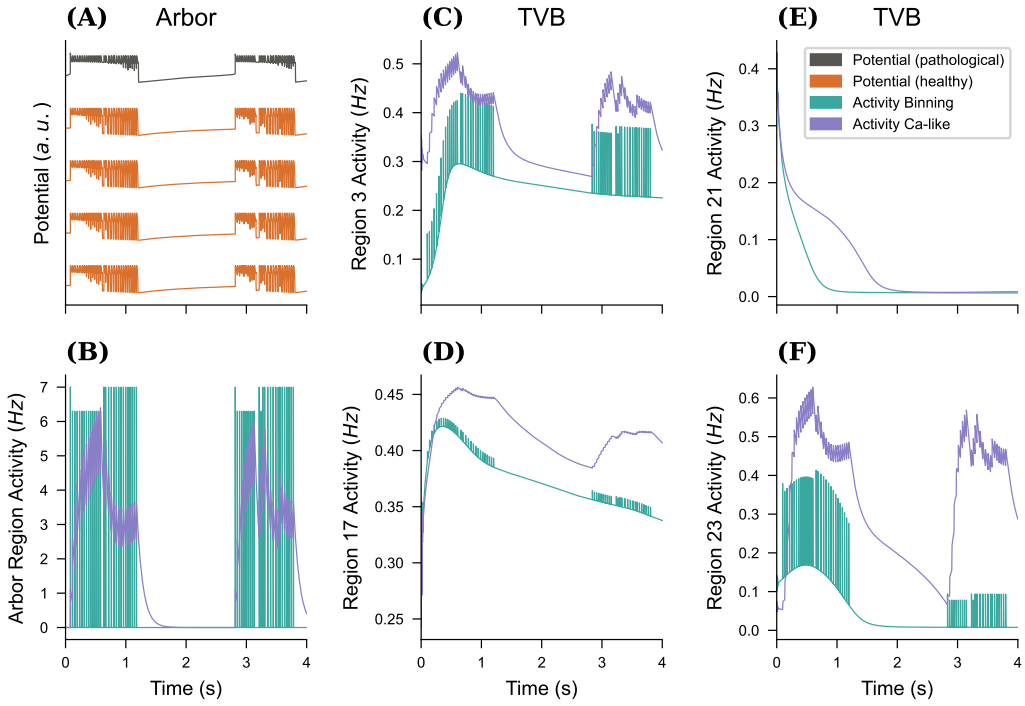

Figure IV.4: **Impact of conversion method on activity exchange.** For an all-to-all connected network of a mixture of 10 pathological cells ($K_{\text{bath}} = 17.5\,\text{mM}$) and 90 healthy ($K_{\text{bath}} = 9.5\,\text{mM}$) neurons we plot the membrane potential traces **(A)** for four healthy and one pathological cell in **(A)**. This simulation is repeated for two choices of generating the activity of the detailed network, either spikes were binned into buckets of width Δt to extract instantaneous rates, or the differential equation IV.7 emulating the change in Calcium concentration of a biological cell after spiking was used (with $\tau = 100\,\text{ms}$ and $\beta = \frac{0.1}{N}$). The resulting activity traces for the Arbor **(B)** network and selected TVB nodes (**(C)**–**(F)**, out of 98 regions).

1.2.3 Bringing Arbor and TVB together

Finally, bi-directional translation between TVB's variable concept and Arbor's representation of action potentials is required. As the former depends on the region models used, we chose to bundle this with the remaining TVB functionality as part of the Arbor proxy node. For the TVB models used in this chapter, the main variable is the per-region mean activity rate ν_I which is conceptually compatible with the concept of spike generation. For each region I connected to the proxy node P, i.e., with connectome weight $c_{IP} > 0$, a set of synthetic events needs to be generated such that the mean activity conforms to ν_I. This is an ambiguous process, even if we prescribe a population (list of cell identifiers) and a per-cell distribution, e.g., a Poisson point process, from which to draw events, which likely must be resolved by ensembles of simulations. In general, this is both model dependent and mathematically intractable, so we leave the general case as a customization point in the framework. For our running example, however, we make the following choice: Event timings for the current step k will be drawn from a uniform distribution and dispatched to all cells in the Arbor network, Note that while these events are created at given time a per-connection delay is applied and thus delivery occurs at a later time.

The inverse direction, converting spike events to mean rates, while being well-defined, is still subject to customization. We explore two options here. First, simple running averages, i.e. all spike originating within the Arbor network during the current epoch are collected and sorted into bins of width Δt. This list is then normalized to the cell count and time step and sent to TVB as the mean activities as a function of time. Although straightforward, this can lead to unrealistically rough activity traces, especially if cell populations are small. Second, as inspired by high-speed calcium imaging experiments (Grewe *et al.* 2010), a mechanism of tracking cell activity via calcium level is implemented as:

$$\frac{dC_p}{dt} = -\frac{C_p(t)}{\tau} + \beta \sum_{t_{\text{spike},p}} \delta(t - t_{\text{spike},p}), \qquad C_p(0) = 0 \tag{IV.7}$$

with per cell p with decay parameter τ and weight β. Computing the activity becomes the average:

$$\nu_P(t) = \langle C_p(t) \rangle_{p \in P}\,, \tag{IV.8}$$

yielding a smooth trace. This method of converting discrete spiking events into a continuous interval variable is also used in a few plasticity models recruiting a negative feedback control mechanism such as synaptic scaling (Van Rossum *et al.* 2000) and homeostatic structural plasticity (Butz & Van Ooyen 2013; Diaz-Pier *et al.* 2016; Lu *et al.* 2024) models. **Figure** IV.4 compares the impact of this choice on the macro-scale network. In small networks and over short timescales defined by the epoch length as shown in the example, spiking activity occur in noncontiguous bursts, which is dubious in con-

junction with the smooth dynamics of the chosen TVB model. **Figure** IV.4(A) shows the propagation of this noncontiguous activity into the TVB regions, while using the Ca-like model (B) provides smooth dynamics in both the Arbor and TVB models. We thus will use the latter in all simulations from here on out. In general, both methods require scaling by the number of cells in the proxy region to arrive at a scale-free activity measure. A local scaling factor G_{A} is used to convert between the activity detailed network and the region model specific TVB activity measure. In general, G_{A} needs to be adjusted to the choice of connectome and TVB model, similar to the choice of the global coupling strength G in the RWW model, here $G_{\mathrm{A}} = 100$ proved to produce acceptable results.

2 Co-simulation to generate seizure-like propagation activity

So far, we have described the components of the co-simulation framework, that is the model of individual detailed cells, the prototypical network used for detailed cells, and the neural mass model used in TVB, and the manner of establishing a bi-directional connection between Arbor and TVB, as well as the methods of converting between spikes and rates. In summary, an Arbor–TVB co-simulation model consists of the following key components:

- A TVB model based on the connectome and node dynamics.
- One or more internally connected network models in Arbor.
- A specified set of TVB nodes where the Arbor models will be placed.
- A defined mechanism for routing events from TVB to individual cells in Arbor.
- A method for translating Arbor-generated events into TVB variables.
- A translation process for converting TVB variables into events originating from synthetic cells.

Each of these components serves as a customization point for the user. While reasonable default configurations can be provided for some, others require user-defined specifications to suit specific modeling needs.

The single cell model has been demonstrated to exhibit the necessary range of healthy and pathological behaviors. We have also motivated our choice for converting spikes to rates of using a biologically-inspired exponential smoothing filter via a Ca-like activity over simple binning and fix parameters to $\tau = 100\,\text{ms}$ and $\beta = \frac{0.1}{N}$. This normalization is important as it yields results that invariant under changes in the number of cell N in the detailed network.

2.1 Seizure propagation in Arbor-TVB

2.1.1 Propagation of pathological states in a network of detailed cells

As a first step, we consider a network of detailed cells without embedding into a co-simulation and study the impact of a small population of pathological cells on the network dynamics. For this, a simulation of 80% healthy cells ($K_{\text{bath}} = 9.5\,\text{mM}$, tonic spiking) and 20% pathological cells ($K_{\text{bath}} = 17.0\,\text{mM}$, SLE) was set up without any internal connectivity. This simulation was run forward in time for $T = 5\,\text{s}$ and the resulting membrane potentials are shown in **Figure** IV.5. During this phase, all cells follow their inherent behavior independently as in **Figure** IV.2. After this

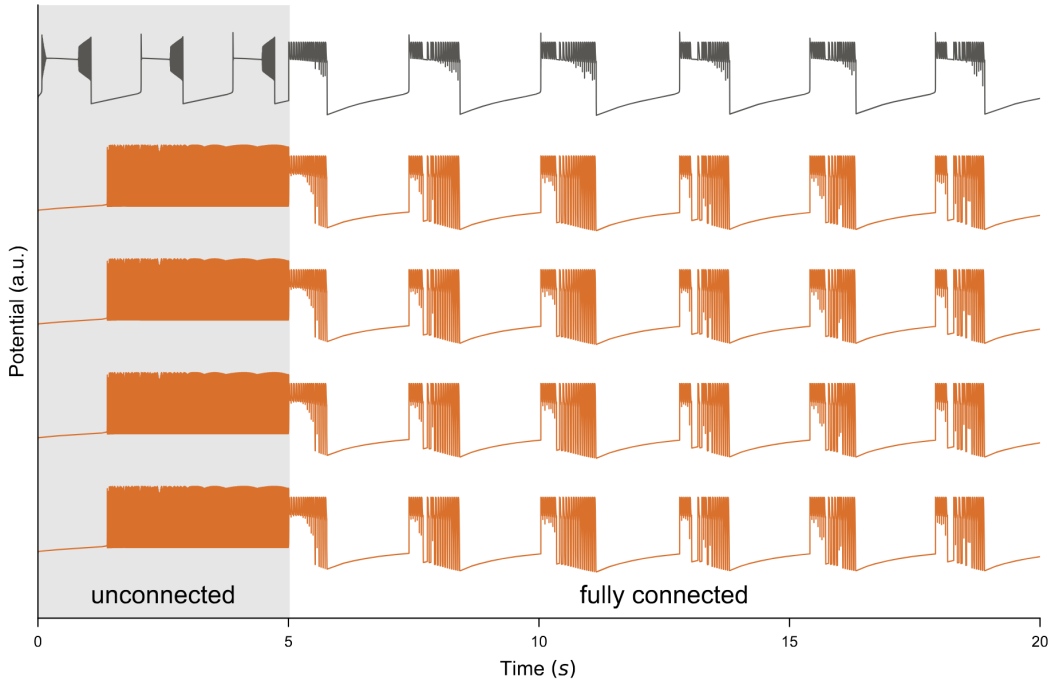

Figure IV.5: **Effect of pathological patterns on the network.** A network simulation of detailed cells comprising 80 % healthy cells ($K_{\text{bath}} = 9.5\,\text{mM}$ tonic spiking) and 20 % pathological cells ($K_{\text{bath}} = 17.0\,\text{mM}$, SLE). Shown are membrane potentials for each cell. The simulation was integrated for 5 s (shaded area) without internal connections during which cells follow their individual patterns as in Fig IV.2. After this initial period the network was switched to a fully connected graph and settles into a new equilibrium state driven by the single pathological cell.

initial undisturbed simulation, integration was halted, the network was transitioned to fully connected, and simulation resumed. The effect of this switch on all cells is immediate and the network now follows the general pace of the pathological neurons modulated by tonic spiking, see **Figure** IV.5, $T \geq 5\,\mathrm{s}$.

2.1.2 Arbor-TVB simulation setup

To induce seizure propagation in mice brain, we use the structural connectivity derived from the Allen mouse brain atlas (Oh *et al.* 2014), also used in (Melozzi *et al.* 2017), to embed the TVB nodes. Following the work presented in (Courson *et al.* 2024), the proxy node modeling the Arbor population of healthy and diseased neurons is set within left Hippocampus, i.e., either left-field CA1 (l CA1), left-field (l CA3), or left Dentate Gyrus (l DG). The proxy node consists in a fully connected network of N neurons. The connections are facilitated using exponential synapses whose weight is tuned to produce sustained network activity. All neurons produce SLE with $K_{\mathrm{bath}} = 17.0\,\mathrm{mM}$. The activity of the spiking neural network is smoothed following Eq. IV.7, with $\tau = 100\,\mathrm{ms}$. **Figure** IV.6 (A) shows the evolution of the membrane potential for the individual neurons in the Arbor network, all neuron exhibiting the same dynamics. As discussed earlier, the initial shape of the SLE is altered by the coupling of the neurons. The neurons are synchronously recruited into seizure patterns of activity. The threshold used for spikes detections was tuned to $-25\,\mathrm{mV}$ to capture the seizure dynamics.

We run simulations over 20 s s, and investigate the effect of SLE emergence in the diseased network once all brain areas have reached their steady state.

2.1.3 Seizure detection

The production of SLE patterns in the diseased Arbor node generates changes in the mean firing rates of TVB local brain areas. Even though changes in the activity occur in most of the brain areas, these fluctuations are generally small, therefore we use region-specific thresholds to detect the seizures. In this section, we characterize a seizure as an SLE activity pattern causing the mean activity to increase at least by 5 % of its baseline resting value. A seizure is then detected at the first peak of increased firing activity.

2.2 Seizure propagation patterns

In **Figure** IV.6(B), we show the time-series of some TVB nodes' mean firing rate over the entire simulation, here with $N = 100$ in the detailed network. A large transient period is necessary before all nodes reach their steady-state. The emergence of recurrent SLE patterns in the Arbor node triggers SLE patterns in the dynamics of the TVB nodes. In the zoomed-in sections, we show a seizure in more detail. The red trajectories highlight the brain areas where the seizure is detected. Note that

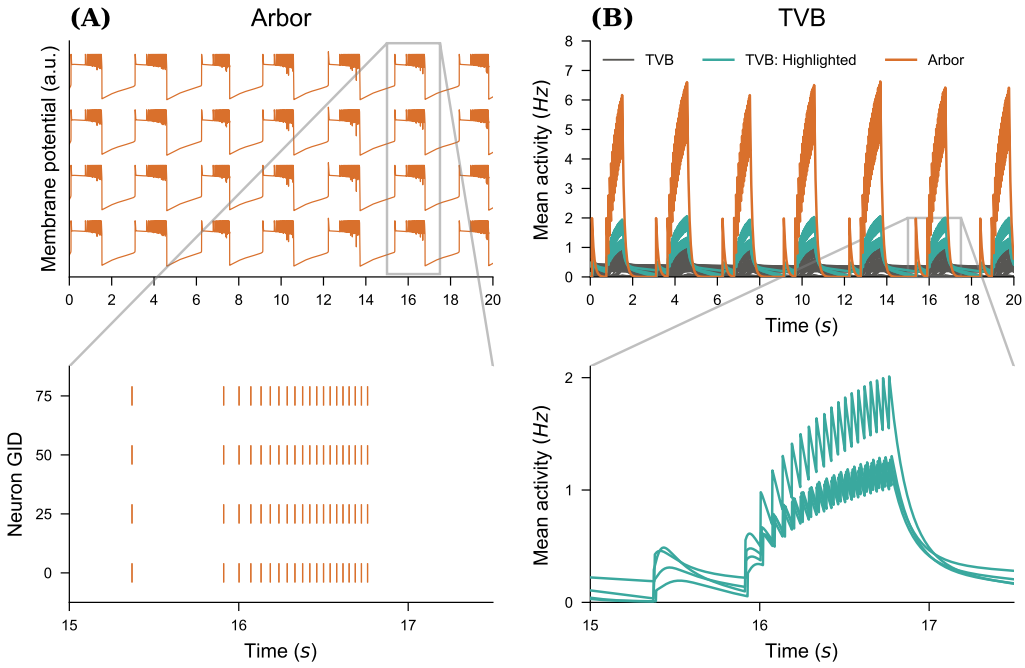

Figure IV.6: **Multiscale seizure propagation.** **(A)** Membrane potential and raster plot for four neurons in the detailed fully-connected Arbor neural network. Note that the membrane potential time-series are similar across all neurons. **(B)** Mean firing rate of various TVB local brain areas versus the Arbor activity. We track a seizure after a transient period, so that all brain areas have reached their baseline activity. The zoomed-in sections show the propagation of the seizure. We highlight and show detail the four timeseries with the largest deviation in activity.

even non-recruited areas leave their steady-state, but the activity remains relatively weak for a seizure to be detected with this criterion.

In **Figure** IV.7, we present the propagation of SLE originating in l CA1 (star marker), represented as a fully connected network of $N = 10\,000$ neurons. Colors on the brain template show the time distance between seizure emergence in the diseased area and seizure arrival in the different brain regions. Following the detection procedure described above within 25 ms a SLE is detected in brain areas inside and outside the hippocampal formations (HFs). Furthermore, we show the activity time-series of four healthy nodes of the brain network being recruited in the seizure, namely the ventral part of left Lateral Septal Nucleus (l LSv), l CA3, l ENTCl and r ENTCl. Note that both the baseline activity and the mean activity reached during the seizure differ depending on the brain area. In particular, since the Allen Mouse Brain SC has symmetrical connections between left and right hemispheres, l ENTCl and r ENTCl have the same baseline activity. However, as the SLE pattern emerges in left Hippocampus, l ENTCl reaches higher spiking rates.

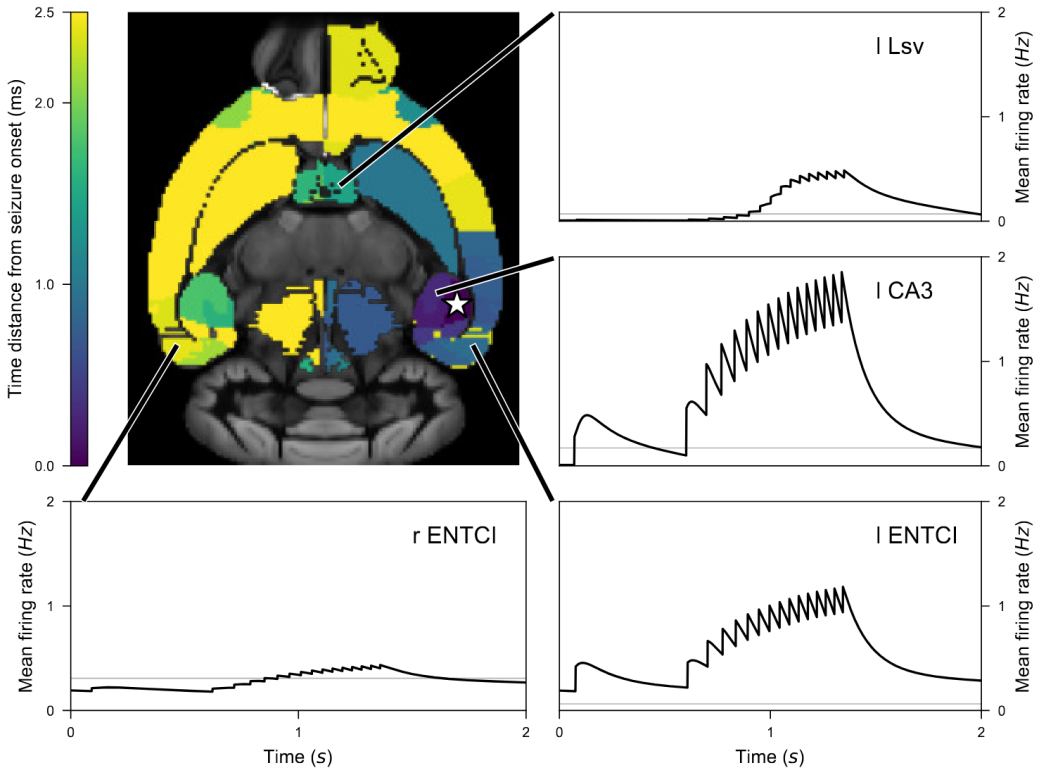

Figure IV.7: **Propagation or a seizure originating in left-field l CA3 area of the mouse brain model.** Time distance between seizure emergence in l CA3 (star marker) and spiking rate increase in each brain area. Time series of selected brain areas are displayed, starting at the detected onset of the seizure. For comparison we also show the baseline activities for these node, the activity in the absence of the Arbor node.

3 Performance of the Arbor-TVB co-Simulation Framework

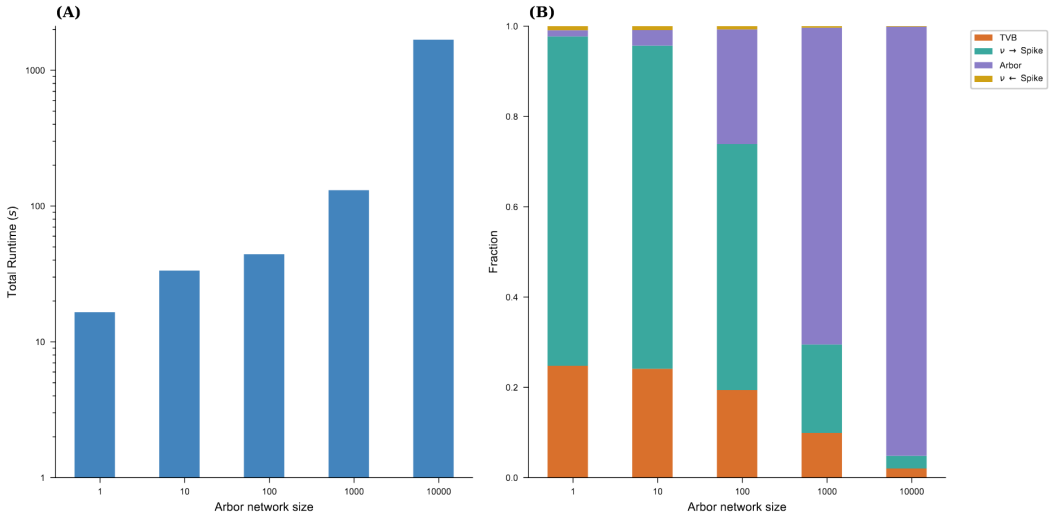

Figure IV.8: **Performance of the running example.**We graph the overall runtime **(A)** of the full co-simulation over the number of cells in the Arbor network as well as the fraction of the main contributions **(B)**: time spent in both simulation engines and in converting between rates and spikes. TVB and rate to spike conversion are the most relevant cost center in the limit of vanishing Arbor network sizes while at large sizes, Arbor compute time dominates.

Next, we briefly analyzed the performance of the running example on a single Apple M1 (2021) laptop. Arbor was built with support for MPI and SIMD (Arm Neon/SVE), and cells were bundled into groups of ten to leverage SIMD units. The overall runtime consists of four main components:

- Arbor model update,
- conversion from spikes to rates,
- TVB model update,
- conversion from rates to spikes.

The Arbor update runs in parallel with the conversions between rates and spikes, as well as the TVB update. During spike exchange, both simulations synchronize, meaning the slower part must wait in the MPI collective, which accounts for the primary time spent in the collective call. **Figure** IV.8 illustrates the total runtime of a 10 s simulation for the entire model described above, along with the relative contributions, for system sizes ranging from one to 10 000 cells. Notably, at 10 000 cells, nearly all computational time is spent within the Arbor network model. In future experiments, we plan to leverage additional hardware, including GPUs, to accelerate

the Arbor side of the simulation. At this scale, TVB and the spike/rate conversions are potential bottlenecks that will require optimization, potentially through TVB's JIT compilation and GPU acceleration. Additionally, further parallelization and porting of the conversion steps to a more performant programming environment remain promising avenues for improvement.

Discussion

In this work, we presented a co-simulation framework that offers a novel approach to bridging the gap between microscopic (spiking neuron) and macroscopic (mean-field) models. This framework integrates Arbor and TVB within a parallelized MPI environment, enabling a detailed yet computationally feasible representation of neural dynamics across scales. To model large-scale brain network dynamics, we used the mean-field reduced Wong-Wang model to reproduce resting-state dynamics. Simultaneously, a detailed spiking neural network was simulated with Arbor, employing a physiological model of seizures at the neuron level (**Figure** IV.2). The spiking activity of the population was then converted into a smooth trace for the proxy node, which was communicated with TVB [**Figure** IV.3(B)]. This co-simulation approach successfully captured the interplay between spiking activity and large-scale brain dynamics, where local neuron dynamics generate global activity wave-fronts. At the microscopic scale, we demonstrated that the structure of the detailed neural network influences its activity patterns, thereby affecting the shape of the activity wavefront (**Figure** IV.4).

As a proof of concept, we simulated the emergence of seizure-like activity patterns (SLE) in the mouse hippocampus, using the Allen Mouse Brain Structural Connectivity data. We modeled the diseased brain area with a small, fully-connected network of neurons SLE, which produces scale-free activity patterns. This approach offers a well-understood and easily controlled model, which is essential for demonstrating the usability of the technical substrate. However, it leaves significant potential for more complex cell models untapped. We would like to stress that this is not a limitation of the framework or its components, and it is possible build upon the model used here in future works.

Arbor has embarked on many types of computational studies as a new-generation simulator. It enables seamless conversion and simulation of single-neuron models from the NEURON simulator and supports simulations of both individual neurons and large-scale networks. Arbor accommodates various plasticity models, including spike-timing dependent plasticity, calcium-based synaptic tagging and capture, and structural plasticity. It has been used to study synaptic tagging and capture via the built-in diffusion functionality [(Luboeinski *et al.* 2024), under review]. Recent developments focus on co-simulation with membrane dynamics and external kernels, enabling dynamic connectivity modifications in a distance-dependent manner. With its high flexibility and scalability, Arbor stands out as a promising platform developed within the EBRAINS initiative to advance cross-scale simulations in computational neuroscience. Arbor is available as part of EBRAINS software distribution (ESD) on connected HPC centres and the EBRAINS collab via Jupyter Lab. Providing a bridge between morphologically detailed neurons and neural mass models encompassing the full brain spans a gap of scale from sub-micrometer to decimeter. It allows for placing the resolution — using Arbor and detailed models — where needed and using realistic, data driven environments everywhere else via TVB.

Despite its successes, the Arbor-TVB framework has some limitations. The co-simulation requires careful exploration and calibration of coupling parameters to

ensure meaningful interactions between Arbor and TVB, which remains a challenge when generalizing to diverse neural models. Specifically, computational costs for large neural networks may necessitate further optimization in model parallelization and data handling. A near-term goal would be to incorporate new features, such as synaptic plasticity, which could offer valuable insights into how brain networks adapt and reorganize in response to disrupted activity.

From an epilepsy-seizure perspective, while the framework provides insights into seizure propagation, additional validation against empirical data would enhance its applicability to clinical settings. This co-simulation framework could enable a detailed investigation of the physiological sources of seizures. Understanding the impact of the structure of the diseased area on seizure patterns and propagation would be of great interest [see e.g., (Netoff *et al.* 2004; Garcia-Ramos *et al.* 2016)]. Specifically, we expect the inhibition and excitation ratios in the detailed neural network to play a critical role in seizure patterns [see e.g., (Liu *et al.* 2020; Engel 1996)].

Conclusions

In this thesis, we explored the interplay between brain network structures, nonlinear dynamics and epilepsy modeling. By integrating graph analyses, dynamical systems modeling and biophysically detailed neural simulations, we have provided insights into the mechanisms governic coherent neural activity, and seizure patterns across spatial and temporal scales.

Key Contributions

- **Network modulation** From a theoretical point of view, we employed the Kuramoto model to investigate how different structural properties modulate global synchronization in coupled neural oscillators. These findings extend previous work by demonstrating how local connectivity disruptions may lead to large-scale network effects.
- **Brain network topology and seizure propagation.** We examined how structural brain networks influence seizure dynamics using phenomenological and physiological models. By characterizing epilepsy within the framework of complex networks, we highlighted the importance of connectivity topology in shaping pathological activity. We showed that local connectivity structures influence global seizure propagation, suggesting that targeted interventions at specific network nodes could mitigate seizure spread.
- **Seizure propagation control.** With a clinical perspective, we explored computational methods for seizure propagation prediction and potential propagation control strategies. By identifying critical network regions, we proposed novel approaches for confining epileptic activity through localized network-based interventions.
- **Arbor-TVB co-simulation framework.** A more engineering-driven contribution to computational neuroscience lies in the development of a multi-scale co-simulation framework handling spiking neural networks with Arbor and mean-field models with TVB. This approach allowed to bridge the gap between microscopic and macroscopic descriptions of neural activity.

Perspectives

Our work still presents room for improvement, and opens up numerous opportunities for a deeper study of epilepsy, and neurological pathologies in general.

- **Empirical assessment of the computational findings.** To date, our work remains mainly computational and theoretical. Comparing our findings on Epileptogenic Zone structures, seizure propagation patterns and propagation control methods with neurological experiments would be of great interest to validate or constraint the computational models and strategies.

- **Study of the mechanisms underlying seizure emergence.** The Arbor-TVB framework opens an avenue to study numerous structural and physiological parameters of diseased brain regions, and their role in seizure production. From an epilepsy perspective, such investigation would aim to identify the mechanisms underlying epileptogenicity, and search for correlation between neural mechanisms and specific propagation patterns.

- **Arbor-TVB.** The Arbor-TVB co-simulation framework seeks to extend its role in computational neuroscience beyond seizure-related studies. Expanding the multiscale co-simulation framework to include even more detailed cellular models, or incorporating additional ones, would enhance the framework's applicability in studying a larger repertoire of brain dynamics and more complex neurological phenomena.

A Appendix

Additional structural connectivity matrices generated from the Allen connectome

In **Figure** A.1, we show in a logarithmic scale the SC of the 20 generated SC. We preserve the structural properties of the Allen connectome (see **Figure** III.2). In **Figure** A.2, we display the difference between the original weight c_{ij} and the new weight c'_{ij} of their connections. Red elements indicate strengthened connections. Blue elements indicate weakened connections. While conserving the overall structure of the SC, there is a significant change in some of the strongest edges weight.

Network edge removal

In **Figure** A.3, we show two resection procedures for the localization of epileptic seizures initiating in l CA1. In **Figure** A.3(A), we remove the inter-hemispheric pathway l CA1 $\nrightarrow$ r CA3 and the pathways leading from the EZ to extra-hippocampal left areas, namely left Entorhinal Cortex (l ENTl) and left Subiculum (l SUB). In **Figure** A.3(B), we remove the inter-hemispheric pathway l CA1 $\nrightarrow$ r CA3 and the pathways leading from l ENTl, l SUB to high-centrality nodes of the brain network, namely the left Ectorhinal Cortex (l ECT), Perirhinal Cortex (l PRh) and Temporal Association (l TEa) areas. With these two procedures, we achieve seizure localization in a reduced number of brain areas, which suggests that network hubs are important for epileptic seizure propagation.

In **Figure** A.4(A), we present the effects of outgoing weight reduction and edge removal approaches *Case I* (l CA1 $\nrightarrow$ r CA3 and l CA1 $\nrightarrow$ l DG), *Case II* (l CA1 $\nrightarrow$ l DG and r CA3 $\nrightarrow$ r CA1) and *Case III* (l CA1 $\nrightarrow$ l CA3) for the left-field CA1 area in the 20 generated randomization of the Allen connectome. In **Figure** A.4(B), we present the effects of outgoing weight reduction and edge removal approaches *Case I'* (l DG $\nrightarrow$ r DG and l DG $\nrightarrow$ l CA1), *Case II'* (l DG $\nrightarrow$ l CA1 and r CA3 $\nrightarrow$ r DG) and *Case III'* (l DG $\nrightarrow$ l CA3) for the left Dentate Gyrus area in the 20 generated randomization of the Allen connectome. The two dashed lines show the upper (resp. lower) threshold of the largest outgoing weight separating the widespread from localized seizures (see **Figure** III.10 and relevant discussion for more details). When applying outgoing weight reduction, the progressive decrease of the EZ's outgoing connective strength leads its connectivity towards lower eigenvector centrality values, and especially lower strongest outgoing weight values. In all 20 generated SC matrices, seizure localization is achieved when the EZ passes below the ω_{lower} threshold. The approach *Case III* also results in reducing the EZ's strongest outgoing weight to value below ω_{lower} threshold. The edge removal approaches *Case I* and *II* (resp. *Case I'* and *Case II'* mildly also reduce the EZ's eigenvector centrality, and most of the time leads to seizure localization without any modification of its strongest outgoing connection.

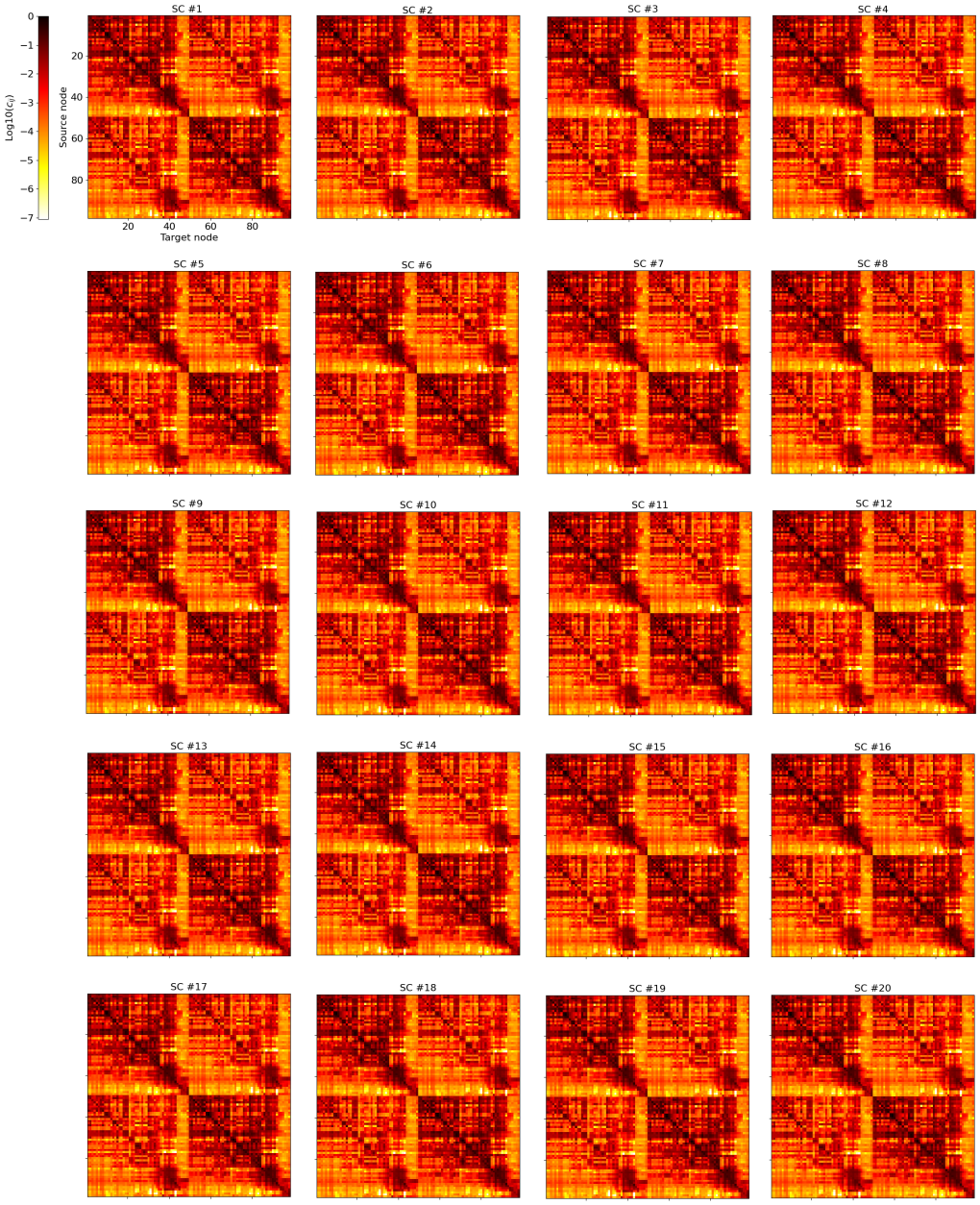

Figure A.1: **Allen SC matrices used for statistical analysis.** For the 20 generated SC, we display the new weight matrix. We show the logarithm of the weight of each connection.

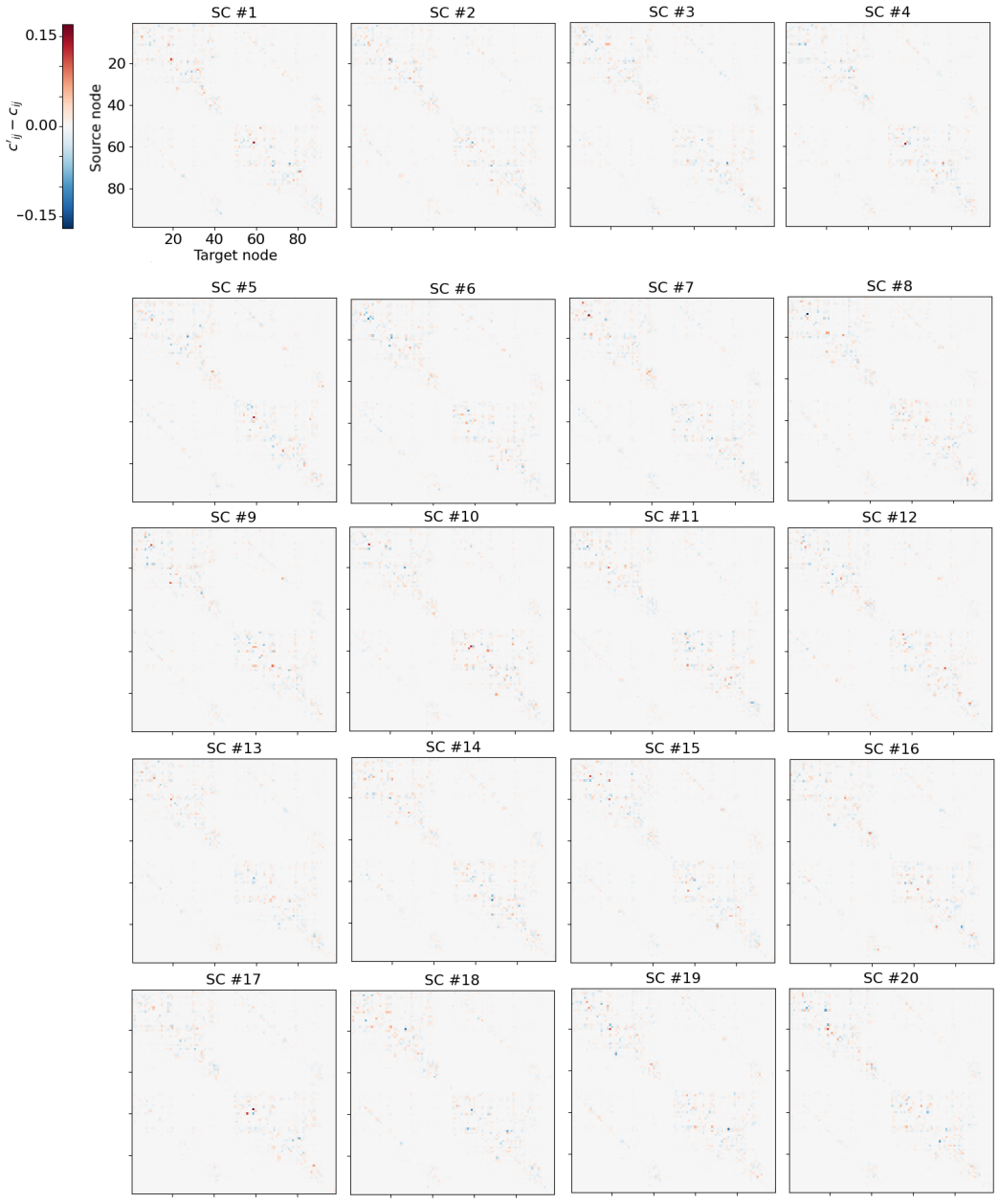

Figure A.2: **Weight value difference between the additional SC matrices and the original Allen connectome.** For the 20 generated SC $SC' = (c'_{ij})$, we display the weight difference $c'_{ij} - c_{ij}$ between each respective matrix entry value.

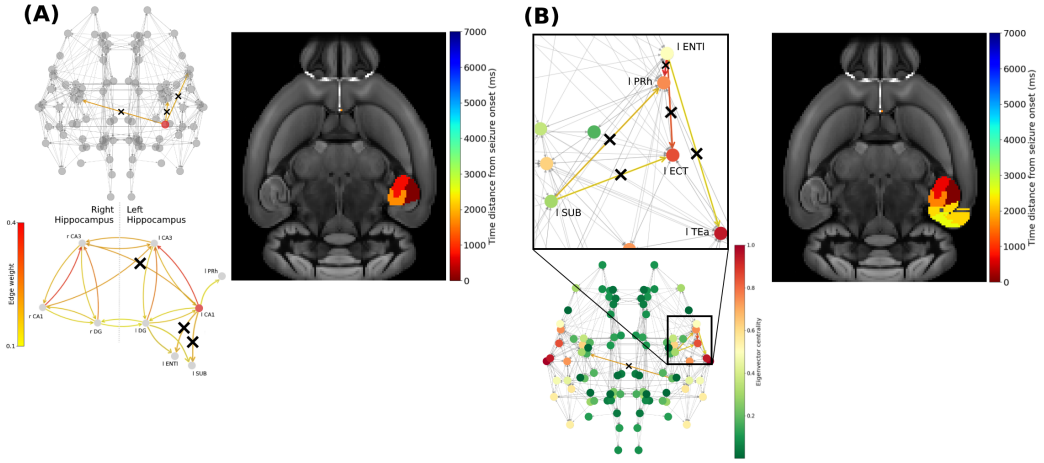

Figure A.3: **Widespread seizure prevention by edge removal in the left-field CA1.** The upper left panels show the brain network. Crosses indicate the removed connections, and the edges' color shows their respective weight. The right panels show the time distance between seizure initiation in the EZ and its onset in each brain area. **(A)** Seizure propagation in the Allen connectome after removing the inter-hemispheric strong connection l CA1 $\nrightarrow$ r CA3, and the two strong connections leading from the EZ to outside of left Hippocampus (namely the lateral part of the Entorhinal Cortex ENTl and the Subiculum (SUB)). The lower left panel illustrates the left extra-hippocampal connections and their weights values are given in the left colorbar. **(B)** Seizure propagation after removing the inter-hemispheric strong connection l CA1 $\nrightarrow$ r CA3, and all strong connections ($c_{ij} > 0.1$) leading from l ENTl, l SUB to networks hubs, namely the left Ectorhinal Cortex (ECT), Perirhinal Cortex (PRh) and Temporal Association (TEa) areas. The color of the nodes show their normalized eigenvector centrality.

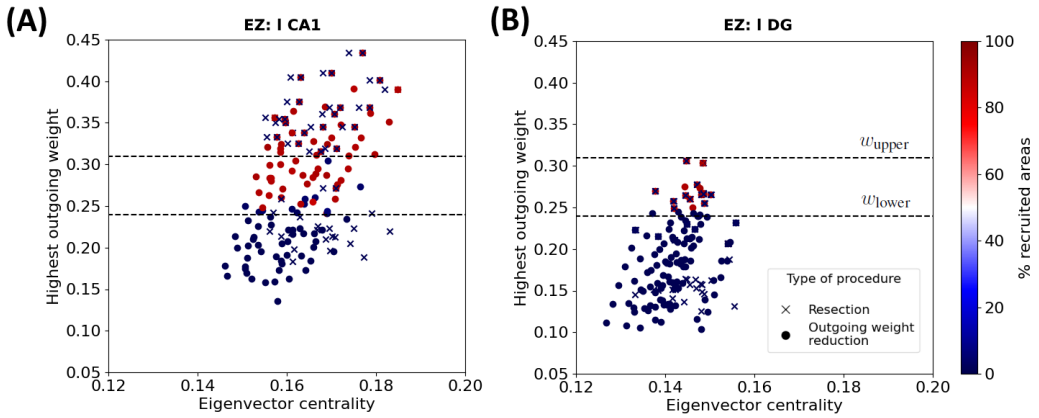

Figure A.4: **EZ connectivity and percentage of seizure-recruited areas after outgoing weight reduction and edge resection in the 20 generated connectomes.** Each point shows the eigenvector centrality and the largest outgoing weight value in one of the 20 randomized connectomes of **(A)** left-field CA1 and **(B)** left Dentate Gyrus, before and after applying outgoing weight reduction (circles) and edge removal strategies presented in **Figure** (6) and **Figure** (7) (crosses). The color of each point shows the percentage of recruited brain areas when the seizure starts in the corresponding node. The two dashed lines show the upper (resp. lower) threshold of the largest outgoing weight from separating the widespread from localized seizures.

Functional Connectivity before and after structural interventions

We also use functional analysis to evaluate time correlation between spatially distant brain areas' activity. To simulate functional connectivity, we compute 10 minute-long time-series of exclusively non-epileptogenic Epileptors coupled through the SC, to reproduce normal brain activity. The first 10 seconds of these time-series are removed to discard the initial bursting due to random initial conditions (the system requires some time to reach its stable state due to transient effects). The Epileptor activity is converted into simulated BOLD activity time-series using hemodynamic response functions implemented in TVB (Friston *et al.* 2000).

The Functional Connectivity (FC) matrix FC_{ij} is measured by the Pearson Correlation Coefficient r, i.e. by correlating simulated BOLD time series data between every pair of nodes in our network graph (Stephan & Friston 2009; Ladwig *et al.* 2022):

$$r_{ij} = r(x_i, x_j). \tag{A.1}$$

In **Figure** A.5, we show the original Allen SC matrix (panel (A)) together with modified ones, following effective seizure localization strategies. Panel (B) shows the SC after applying a standard resection technique presented in (Melozzi *et al.* 2017). This approach consists in the removal of the CA1 and CA3 areas in both hemi-

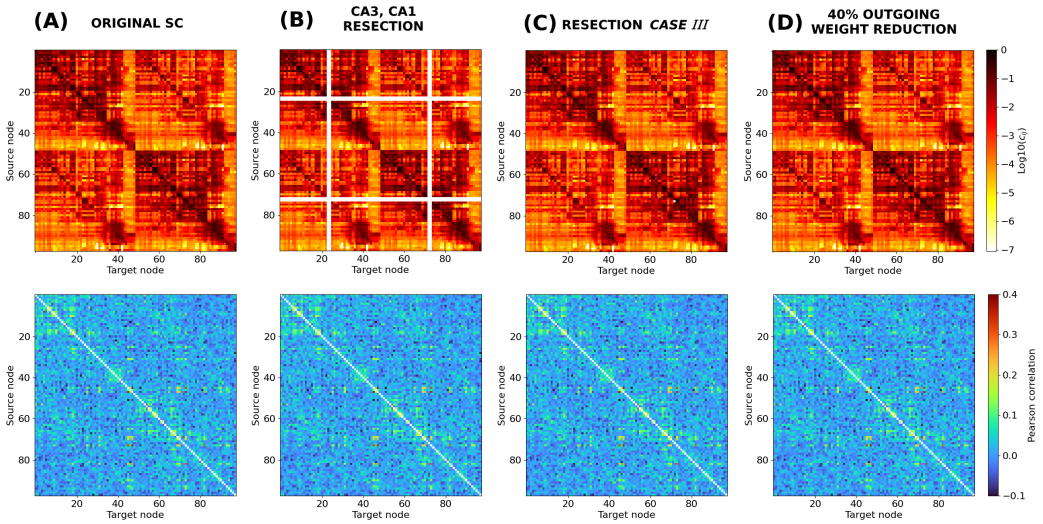

Figure A.5: **Connectome structure and functionality after resection and outgoing weight reduction procedures.** We show the network structural connectivity (top) and functional connectivity (bottom) matrices. **(A)** Original connectome, **(B)** after the resection of left and right CA1 and CA3 areas, following the procedure presented in (Melozzi *et al.* 2017), **(C)** after applying resection *Case III* and **(D)** after applying l CA1 outgoing weight reduction of 40%.

spheres. Panel (C) shows the SC after applying resection *Case II I*, e.g. the resection of a single connection l CA1 $\nrightarrow$ l CA3, and panel (D) shows the SC after applying a 40% outgoing weight reduction on l CA1. With the latter two options, we minimize the structural modifications compared to the CA1, CA3 resection procedure (Melozzi *et al.* 2017). By setting our system at a "healthy" (i.e., modeling all network nodes as non EZ), we do not manage to observe notable difference between the FC produced by the original SC matrix and the FC matrices produced with the different intervention procedures introduced in our manuscript. Here we show only a few typical examples. Note that we have also attempted to estimate matrix distances, e.g. by calculating the Pearson correlation coefficient between different pairs of matrices (see e.g. (Popovych *et al.* 2021; Manos *et al.* 2023)), but we did not observe striking dissimilarities (results not shown here). It is also worth noting that at this stage we did not aim to compare our simulated time series (or FC matrices) to experimental neuroimaging mice signals.

Bibliography

[Acebrón *et al.* 2005] Juan A. Acebrón, L. L. Bonilla, Conrad J. Pérez Vicente, Félix Ritort and Renato Spigler. *The Kuramoto model: A simple paradigm for synchronization phenomena.* Reviews of Modern Physics, vol. 77, no. 1, page 137–185, 2005. (Cited on page 52.)

[Adamczyk *et al.* 2021] Bożena Adamczyk, Karolina Węgrzyn, Tomasz Wilczyński, Justyna Maciarz, Natalia Morawiec and Monika Adamczyk-Sowa. *The most common lesions detected by neuroimaging as causes of epilepsy.* Medicina, vol. 57, no. 3, page 294, 2021. (Cited on page 8.)

[Ahn *et al.* 2017] Sora Ahn, Sumin Jo, Sang Beom Jun, Hyang Woon Lee and Seungjun Lee. *Prediction of the seizure suppression effect by electrical stimulation via a computational modeling approach.* Frontiers in Computational Neuroscience, vol. 11, 2017. (Cited on page 88.)

[Ajilore *et al.* 2013] Olusola Ajilore, Liang Zhan, Johnson GadElkarim, Aifeng Zhang, Jamie Feusner, Shaolin Yang, Paul Thompson, Anand Kumar and Alex Leow. *Constructing the resting state structural connectome.* Frontiers in Neuroinformatics, vol. 7, 2013. (Cited on pages 83 and 89.)

[Akar *et al.* 2019] N. A. Akar, B. Cumming, V. Karakasis, A. Küsters, W. Klijn, A. Peyser and S. Yates. *Arbor — A Morphologically-Detailed Neural Network Simulation Library for Contemporary High-Performance Computing Architectures.* In 2019 27th Euromicro International Conference on Parallel, Distributed and Network-Based Processing (PDP), pages 274–282, 2019. (Cited on pages 49, 94 and 96.)

[Alexandratou *et al.* 2021] Ioanna Alexandratou, Panayiotis Patrikelis, Lambros Messinis, Athanasia Alexoudi, Anastasia Verentzioti, Maria Stefanatou, Grigorios Nasios, Vasileios Panagiotopoulos and Stylianos Gatzonis. *Long-term neuropsychological outcomes following temporal lobe epilepsy surgery: An update of the literature.* Healthcare, vol. 9, no. 9, page 1156, 2021. (Cited on page 77.)

[Amato *et al.* 2016] Stephen P. Amato, Feng Pan, Joel Schwartz and Timothy M. Ragan. *Whole Brain Imaging with Serial Two-Photon Tomography.* Frontiers in Neuroanatomy, vol. 10, 2016. (Cited on page 20.)

[An *et al.* 2019] Sora An, Fabrice Bartolomei, Maxime Guye and Viktor Jirsa. *Optimization of surgical intervention outside the epileptogenic zone in the virtual epileptic patient (VEP).* PLOS Computational Biology, vol. 15, no. 6, 2019. (Cited on pages 45, 65 and 87.)

[Augustine *et al.* 2003] George J Augustine, Fidel Santamaria and Keiko Tanaka. *Local calcium signaling in neurons.* Neuron, vol. 40, no. 2, pages 331–346, 2003. (Cited on page 93.)

[Bakhtiarzadeh *et al.* 2023] Fatemeh Bakhtiarzadeh, Meysam Zare, Zahra Ghasemi, Samaneh Dehghan, Azam Sadeghin, Mohammad Taghi Joghataei and Nooshin Ahmadirad. *Neurostimulation as a Putative Method for the Treatment of Drug-resistant Epilepsy in Patient and Animal Models of Epilepsy.* Basic Clin Neurosci, vol. 14, no. 1, pages 1–18, 2023. (Cited on page 66.)

[Barabási & Albert 1999] Albert-László Barabási and Réka Albert. *Emergence of Scaling in Random Networks.* Science, vol. 286, no. 5439, pages 509–512, 1999. (Cited on pages 19, 51 and 53.)

[Barral *et al.* 2019] Jeremie Barral, Xiao-Jing Wang and Alex D Reyes. *Propagation of temporal and rate signals in cultured multilayer networks.* Nature communications, vol. 10, no. 1, page 3969, 2019. (Cited on page 93.)

[Barrat *et al.* 2008] Alain Barrat, Marc Barthélemy and Alessandro Vespignani. Dynamical processes on complex networks. Cambridge University Press, 1 édition, 2008. (Cited on page 51.)

[Bassett & Bullmore 2016] Danielle S. Bassett and Edward T. Bullmore. *Small-world brain networks revisited.* The Neuroscientist, vol. 23, no. 5, page 499–516, 2016. (Cited on pages 17 and 51.)

[Bastos & Schoffelen 2016] André M. Bastos and Jan-Mathijs Schoffelen. *A Tutorial Review of Functional Connectivity Analysis Methods and Their Interpretational Pitfalls.* Frontiers in Systems Neuroscience, vol. 9, 2016. (Cited on page 24.)

[Bauer *et al.* 2017] Prisca R. Bauer, Roland D. Thijs, Robert J. Lamberts, Demetrios N. Velis, Gerhard H. Visser, Else A. Tolner, Josemir W. Sander, Fernando H. Lopes da Silva and Stiliyan N. Kalitzin. *Dynamics of convulsive seizure termination and postictal generalized EEG suppression.* Brain, 2017. (Cited on page 88.)

[Bergoin *et al.* 2023] Raphaël Bergoin, Alessandro Torcini, Gustavo Deco, Mathias Quoy and Gorka Zamora-López. *Inhibitory neurons control the consolidation of neural assemblies via adaptation to selective stimuli.* Scientific Reports, vol. 13, no. 1, 2023. (Cited on page 89.)

[Berry & Quoy 2006] Hugues Berry and Mathias Quoy. *Structure and dynamics of random recurrent neural networks.* Adaptive Behavior, vol. 14, no. 2, page 129–137, 2006. (Cited on page 51.)

[Brinkmann *et al.* 2021] Benjamin H. Brinkmann, Nicholas M. Gregg and Gregory A. Worrell. *Seizure forecasting in epilepsy: From computation to clinical practice.* Epilepsy, page 451–490, 2021. (Cited on page 90.)

[Brodie *et al.* 2016] Martin J Brodie, Frank Besag, Alan B Ettinger, Marco Mula, Gabriella Gobbi, Stefano Comai, Albert P Aldenkamp and Bernhard J Steinhoff. *Epilepsy, Antiepileptic Drugs, and Aggression: An Evidence-Based Review.* Pharmacol Rev, vol. 68, no. 3, pages 563–602, 2016. (Cited on page 88.)

[Brogin *et al.* 2023] João A. F. Brogin, Jean Faber, Selvin Z. Reyes-Garcia, Esper A. Cavalheiro and Douglas D. Bueno. *Epileptic seizure suppression: a computational approach for identification and control using real data.* bioRxiv, 2023. (Cited on page 88.)

[Broido & Clauset 2019] Anna D. Broido and Aaron Clauset. *Scale-free networks are rare.* Nature Communications, vol. 10, no. 1, 2019. (Cited on page 19.)

[Brown 2003] Peter Brown. *Oscillatory nature of human basal ganglia activity: Relationship to the pathophysiology of Parkinson's disease.* Movement Disorders, vol. 18, page 357–363, 2003. (Cited on page 51.)

[Buckmaster *et al.* 2022] Paul S. Buckmaster, Bianca Reyes, Tahsin Kahn and Megan Wyeth. *Ventral hippocampal formation is the primary epileptogenic zone in a rat model of Temporal Lobe epilepsy.* Journal of Neuroscience, vol. 42, no. 39, page 7482–7495, 2022. (Cited on page 77.)

[Butz & Van Ooyen 2013] Markus Butz and Arjen Van Ooyen. *A simple rule for dendritic spine and axonal bouton formation can account for cortical reorganization after focal retinal lesions.* PLoS computational biology, vol. 9, no. 10, page e1003259, 2013. (Cited on page 103.)

[Calabrese *et al.* 2015] Evan Calabrese, Alexandra Badea, Gary Cofer, Yi Qi and G Allan Johnson. *A Diffusion MRI Tractography Connectome of the Mouse Brain and Comparison with Neuronal Tracer Data.* Cereb Cortex, vol. 25, no. 11, pages 4628–4637, 2015. (Cited on pages 23 and 70.)

[Carnevale & Hines 2006] Nicholas T. Carnevale and Michael L. Hines. *The NEURON Book.* In Advances in Neural Information Processing Systems. Cambridge: Cambridge University Press, 2006. (Cited on pages 93 and 96.)

[Chaddad *et al.* 2023] Ahmad Chaddad, Yihang Wu, Reem Kateb and Ahmed Bouridane. *Electroencephalography Signal Processing: A Comprehensive Review and Analysis of Methods and Techniques.* Sensors, vol. 23, no. 14, page 6434, 2023. (Cited on page 20.)

[Chater *et al.* 2024] Thomas E Chater, Maximilian F Eggl, Yukiko Goda and Tatjana Tchumatchenko. *Competitive processes shape multi-synapse plasticity along dendritic segments.* Nature Communications, vol. 15, no. 1, page 7572, 2024. (Cited on page 93.)

[Chialvo 2010] Dante R. Chialvo. *Emergent Complex Neural Dynamics.* Nature Physics, vol. 6, no. 10, page 744–750, 2010. (Cited on pages 33 and 51.)

[Chiba *et al.* 2018] Hayato Chiba, Georgi S. Medvedev and Matthew S. Mizuhara. *Bifurcations in the Kuramoto model on graphs.* Chaos: An Interdisciplinary Journal of Nonlinear Science, vol. 28, no. 7, page 073109, 2018. (Cited on page 55.)

[Chizhov & Sanin 2020] Anton V. Chizhov and Aleksei E. Sanin. *A simple model of epileptic seizure propagation: Potassium diffusion versus axo-dendritic spread.* PLOS ONE, vol. 15, no. 4, 2020. (Cited on page 65.)

[Chowdhury *et al.* 2021] Fahmida A Chowdhury, Rui Silva, Benjamin Whatley and Matthew C Walker. *Localisation in focal epilepsy: A practical guide.* Practical Neurology, vol. 21, no. 6, page 481–491, 2021. (Cited on page 9.)

[Cohen *et al.* 2021] Nathan T. Cohen, J. Helen Cross, Alexis Arzimanoglou, Samuel F. Berkovic, John F. Kerrigan, Ilene Penn Miller, Erica Webster, Lisa Soeby, Arthur Cukiert, Dale K. Hesdorffer and et al. *Hypothalamic Hamartomas.* Neurology, vol. 97, no. 18, page 864–873, 2021. (Cited on page 8.)

[Coletta *et al.* 2020] Lovico Coletta, Marco Pagani, Jennifer D. Whitesell, Julie A. Harris, Boris Bernhardt and Alessandro Gozzi. *Network structure of the mouse brain connectome with voxel resolution.* Science Advances, vol. 6, no. 51, page eabb7187, 2020. (Cited on page 87.)

[Corinto & Torcini 2019] Fernando Corinto and Alessandro Torcini. Nonlinear dynamics in computational neuroscience. PoliTO Springer Series. Springer International Publishing, Cham, 2019. (Cited on page 26.)

[Courson *et al.* 2023] Juliette Courson, Thanos Manos and Mathias Quoy. *Networks' modulation: How different structural network properties affect the global synchronization of coupled Kuramoto oscillators.* In T. Bountis, F. Vallianatos, A. Provata, D. Kugiumtzis and Y. Kominis, editeurs, Chaos, Fractals and Complexity, Springer Proceedings in Complexity, pages 233–244, 2023. (Cited on page 91.)

[Courson *et al.* 2024] Juliette Courson, Mathias Quoy, Yulia Timofeeva and Thanos Manos. *An exploratory computational analysis in mice brain networks of widespread epileptic seizure onset locations along with potential strategies for effective intervention and propagation control.* Front. Comput. Neurosci., vol. 18, page 1360009, 2024. (Cited on pages 94 and 107.)

[Courtiol *et al.* 2020] Julie Courtiol, Maxime Guye, Fabrice Bartolomei, Spase Petkoski and Viktor K. Jirsa. *Dynamical mechanisms of interictal resting-state functional connectivity in epilepsy.* The Journal of Neuroscience, vol. 40, no. 29, page 5572–5588, 2020. (Cited on page 91.)

[Crawford 1991] John David Crawford. *Introduction to bifurcation theory.* Reviews of Modern Physics, vol. 63, no. 4, page 991–1037, 1991. (Cited on page 29.)

[Cumming *et al.* 2024] Benjamin Cumming, Stuart Yates, Thorsten Hater, Han Lu, Brent Huisman, Klijn Wouter, Fabian Bösch, Simon Frasch, Robin de Schepper and Jannik Luboeinski. *Arbor v0.10.0*, 2024. (Cited on page 94.)

[Darnell 2013] Robert B Darnell. *RNA protein interaction in neurons.* Annual review of neuroscience, vol. 36, no. 1, pages 243–270, 2013. (Cited on page 93.)

[Deco *et al.* 2013] G. Deco, A. Ponce-Alvarez, D. Mantini, G. L. Romani, P. Hagmann and M. Corbetta. *Resting-state functional connectivity emerges from structurally and dynamically shaped slow linear fluctuations.* Journal of Neuroscience, vol. 33, no. 27, page 11239–11252, 2013. (Cited on pages 36 and 99.)

[Demirtaş *et al.* 2019] Murat Demirtaş, Joshua B Burt, Markus Helmer, Jie Lisa Ji, Brendan D Adkinson, Matthew F Glasser, David C Van Essen, Stamatios N Sotiropoulos, Alan Anticevic and John D Murray. *Hierarchical heterogeneity across human cortex shapes large-scale neural dynamics.* Neuron, vol. 101, no. 6, pages 1181–1194, 2019. (Cited on page 93.)

[Depannemaecker *et al.* 2021] Damien Depannemaecker, Alain Destexhe, Viktor Jirsa and Christophe Bernard. *Modeling seizures: From single neurons to networks.* Seizure, vol. 90, pages 4–8, 2021. (Cited on page 90.)

[Depannemaecker *et al.* 2022] Damien Depannemaecker, Anton Ivanov, Davide Lillo, Len Spek, Christophe Bernard and Viktor Jirsa. *A unified physiological framework of transitions between seizures, sustained ictal activity and depolarization block at the single neuron level.* Journal of Computational Neuroscience, vol. 50, no. 1, page 33–49, 2022. (Cited on pages 45, 91, 95, 96 and 99.)

[Diaz-Pier *et al.* 2016] Sandra Diaz-Pier, Mikaël Naveau, Markus Butz-Ostendorf and Abigail Morrison. *Automatic generation of connectivity for large-scale neuronal network models through structural plasticity.* Frontiers in Neuroanatomy, vol. 10, page 57, 2016. (Cited on pages 93 and 103.)

[Dicks 2022] Leon MT Dicks. *Gut bacteria and neurotransmitters.* Microorganisms, vol. 10, no. 9, page 1838, 2022. (Cited on page 93.)

[Ding *et al.* 2020] Song-Lin Ding, Joshua J. Royall, Susan M. Sunkin, Benjamin A.C. Facer, Phil Lesnar, Amy Bernard, Lydia Ng and Ed S. Lein. *Allen Human Reference Atlas – 3D, 2020.* Research Resource Identifier (RRID): SCR_017764, 2020. Available from: https://www.brain-map.org/. (Cited on page 21.)

[Dorogovtsev & Mendes 2003] S.N. Dorogovtsev and J.F.F. Mendes. Evolution of networks. Oxford University Press, 2003. (Cited on page 51.)

[Eggermont & Tass 2015] Jos J. Eggermont and Peter A. Tass. *Maladaptive Neural Synchrony in Tinnitus: Origin and Restoration.* Frontiers in Neurology, vol. 6, 2015. (Cited on page 52.)

[Emina & Kropff 2022] Facundo Emina and Emilio Kropff. *Selective connectivity enhances storage capacity in attractor models of memory function.* Frontiers in Systems Neuroscience, page 104, 2022. (Cited on page 93.)

[Engel 1996] Jerome Engel. *Excitation and Inhibition in Epilepsy.* Canadian Journal of Neurological Sciences / Journal Canadien des Sciences Neurologiques, vol. 23, no. 3, page 167–174, 1996. (Cited on page 113.)

[Esclapez *et al.* 1999] M Esclapez, J C Hirsch, Y Ben-Ari and C Bernard. *Newly formed excitatory pathways provide a substrate for hyperexcitability in experimental temporal lobe epilepsy.* J Comp Neurol, vol. 408, no. 4, pages 449–460, 1999. (Cited on page 66.)

[Fisher & Velasco 2014] Robert S. Fisher and Ana Luisa Velasco. *Electrical brain stimulation for epilepsy.* Nature Reviews Neurology, vol. 10, no. 5, page 261–270, 2014. (Cited on page 13.)

[Fornito *et al.* 2016] Alex Fornito, Andrew Zalesky and Edward T. Bullmore. Fundamentals of brain network analysis. Elsevier, 2016. (Cited on pages 14, 15 and 51.)

[Fortel *et al.* 2019] Igor Fortel, Mitchell Butler, Laura E. Korthauer, Liang Zhan, Olusola Ajilore, Ira Driscoll, Anastasios Sidiropoulos, Yanfu Zhang, Heng Guo Leiand Huang, Dan Schonfeld and Alex Leow. *Brain Dynamics Through the Lens of Statistical Mechanics by Unifying Structure and Function.* In Dinggang Shen, Tianming Liu, Terry M. Peters, Lawrence H. Staib, Sean Essert Carolineand Zhou, Pew-Thian Yap and Ali Khan, editeurs, Medical Image Computing and Computer Assisted Intervention – MICCAI 2019, pages 503–511, Cham, 2019. Springer International Publishing. (Cited on pages 83 and 89.)

[Fortel *et al.* 2020] Igor Fortel, Laura E Korthauer, Zachery Morrissey, Liang Zhan, Olusola Ajilore, Ouri Wolfson, Ira Driscoll, Dan Schonfeld and Alex Leow. *Connectome Signatures of Hyperexcitation in Cognitively Intact Middle-Aged Female APOE-ε4 Carriers.* Cerebral Cortex, vol. 30, no. 12, pages 6350–6362, 2020. (Cited on pages 83 and 89.)

[Fortel *et al.* 2022] Igor Fortel, Mitchell Butler, Laura E. Korthauer, Liang Zhan, Olusola Ajilore, Anastasios Sidiropoulos, Yichao Wu, Ira Driscoll, Dan Schonfeld and Alex Leow. *Inferring excitation-inhibition dynamics using a maximum entropy model unifying brain structure and function.* Network Neuroscience, vol. 6, no. 2, pages 420–444, 2022. (Cited on pages 83 and 89.)

[Fortel *et al.* 2023] Igor Fortel, Liang Zhan, Olusola Ajilore, Yichao Wu, Scott Mackin and Alex Leow. *Disrupted Excitation-Inhibition Balance in Cognitively Normal Individuals at Risk of Alzheimer's Disease.* J Alzheimers Dis, vol. 95, no. 4, pages 1449–1467, 2023. (Cited on pages 83 and 89.)

[Foutz & Wong 2022] Thomas J. Foutz and Michael Wong. *Brain stimulation treatments in epilepsy: Basic mechanisms and clinical advances.* Biomedical Journal, vol. 45, no. 1, page 27–37, 2022. (Cited on page 13.)

[Friston *et al.* 2000] K.J. Friston, A. Mechelli, R. Turner and C.J. Price. *Nonlinear Responses in fMRI: The Balloon Model, Volterra Kernels, and Other Hemodynamics.* NeuroImage, vol. 12, no. 4, pages 466–477, 2000. (Cited on pages 39 and 120.)

[Friston *et al.* 2003] K.J. Friston, L. Harrison and W. Penny. *Dynamic causal modelling.* NeuroImage, vol. 19, no. 4, page 1273–1302, 2003. (Cited on page 39.)

[Garcia-Ramos *et al.* 2016] Camille Garcia-Ramos, Jack J. Lin, Tanja S. Kellermann, Leonardo Bonilha, Vivek Prabhakaran and Bruce P. Hermann. *Graph theory and cognition: A complementary avenue for examining neuropsychological status in epilepsy.* Epilepsy & Behavior, vol. 64, pages 329–335, 2016. (Cited on page 113.)

[Gast *et al.* 2024] Richard Gast, Sara A Solla and Ann Kennedy. *Neural heterogeneity controls computations in spiking neural networks.* Proceedings of the National Academy of Sciences, vol. 121, no. 3, page e2311885121, 2024. (Cited on page 93.)

[Gentiletti *et al.* 2022] Damiano Gentiletti, Marco de Curtis, Vadym Gnatkovsky and Piotr Suffczynski. *Focal seizures are organized by feedback between neural activity and ion concentration changes.* eLife, vol. 11, 2022. (Cited on page 88.)

[Gerster *et al.* 2021] Moritz Gerster, Halgurd Taher, Antonín Škoch, Jaroslav Hlinka, Maxime Guye, Fabrice Bartolomei, Viktor Jirsa, Anna Zakharova and Simona Olmi. *Patient-Specific Network Connectivity Combined With a Next Generation Neural Mass Model to Test Clinical Hypothesis of Seizure Propagation.* Frontiers in Systems Neuroscience, vol. 15, page 675272, 2021. (Cited on page 65.)

[Gewaltig & Diesmann 2007] Marc-Oliver Gewaltig and Markus Diesmann. *NEST (NEural Simulation Tool).* Scholarpedia, vol. 2, no. 4, page 1430, 2007. (Cited on page 93.)

[Ghulaxe *et al.* 2023] Yash Ghulaxe, Abhishek Joshi, Jay Chavada, Shreyash Huse, Bhakti Kalbande and Prayas Sarda. *Understanding focal seizures in adults: A comprehensive review.* Cureus, 2023. (Cited on page 91.)

[Grewe *et al.* 2010] Benjamin F Grewe, Dominik Langer, Hansjörg Kasper, Björn M Kampa and Fritjof Helmchen. *High-speed in vivo calcium imaging reveals neuronal network activity with near-millisecond precision.* Nature methods, vol. 7, no. 5, pages 399–405, 2010. (Cited on page 103.)

[Grone & Baraban 2015] Brian P Grone and Scott C Baraban. *Animal models in epilepsy research: Legacies and new directions.* Nature Neuroscience, vol. 18, no. 3, page 339–343, 2015. (Cited on page 65.)

[Gros 2024] Claudius Gros. Complex and adaptive dynamical systems: A comprehensive introduction. Springer International Publishing Springer, 2024. (Cited on page 26.)

[Grosu *et al.* 2023] George F Grosu, Alexander V Hopp, Vasile V Moca, Harald Bârzan, Andrei Ciuparu, Maria Ercsey-Ravasz, Mathias Winkel, Helmut Linde and Raul C Mureșan. *The fractal brain: scale-invariance in structure and dynamics.* Cerebral Cortex, vol. 33, no. 8, page 4574–4605, 2023. (Cited on page 63.)

[Gurkiewicz *et al.* 2011] Meron Gurkiewicz, Alon Korngreen, Stephen G Waxman and Angelika Lampert. *Kinetic modeling of Nav1. 7 provides insight into erythromelalgia-associated F1449V mutation.* Journal of Neurophysiology, vol. 105, no. 4, pages 1546–1557, 2011. (Cited on page 93.)

[Gómez-Nava *et al.* 2022] Luis Gómez-Nava, Richard Bon and Fernando Peruani. *Intermittent collective motion in sheep results from alternating the role of leader and follower.* Nature Physics, vol. 18, no. 12, page 1494–1501, 2022. (Cited on page 33.)

[Hagberg *et al.* 2008] Aric A. Hagberg, Daniel A. Schult and Pieter J. Swart. *Exploring Network Structure, Dynamics, and Function using NetworkX.* page 11–15, Pasadena, California, 2008. (Cited on page 49.)

[Hananeia *et al.* 2024] Nicholas Hananeia, Christian Ebner, Christos Galanis, Hermann Cuntz, Alexander Opitz, Andreas Vlachos and Peter Jedlicka. *Multiscale modelling of location-and frequency-dependent synaptic plasticity induced by transcranial magnetic stimulation in the dendrites of pyramidal neurons.* bioRxiv, 2024. (Cited on page 93.)

[Hashemi *et al.* 2020] M. Hashemi, A.N. Vattikonda, V. Sip, M. Guye, F. Bartolomei, M.M. Woodman and V.K. Jirsa. *The Bayesian Virtual Epileptic Patient: A probabilistic framework designed to infer the spatial map of epileptogenicity in a personalized large-scale brain model of epilepsy spread.* NeuroImage, vol. 217, page 116839, 2020. (Cited on pages 45 and 65.)

[Heck *et al.* 2014] Christianne N. Heck, David King-Stephens, Andrew D. Massey, Dileep R. Nair, Barbara C. Jobst, Gregory L. Barkley, Vicenta Salanova,

Andrew J. Cole, Michael C. Smith, Ryder P. Gwinn and et al. *Two-year seizure reduction in adults with medically intractable partial onset epilepsy treated with responsive neurostimulation: Final results of the RNS system pivotal trial.* Epilepsia, vol. 55, no. 3, page 432–441, 2014. (Cited on pages 66 and 83.)

[Heffern *et al.* 2021] Elleard F. Heffern, Holly Huelskamp, Sonya Bahar and R. Fredrik Inglis. *Phase transitions in biology: From bird flocks to population dynamics.* Proceedings of the Royal Society B: Biological Sciences, vol. 288, no. 1961, 2021. (Cited on page 33.)

[Herculano-Houzel *et al.* 2006] Suzana Herculano-Houzel, Bruno Mota and Roberto Lent. *Cellular scaling rules for rodent brains.* Proceedings of the National Academy of Sciences, vol. 103, no. 32, page 12138–12143, 2006. (Cited on page 3.)

[Herculano-Houzel 2009] Suzana Herculano-Houzel. *The human brain in numbers: a linearly scaled-up primate brain.* Frontiers in Human Neuroscience, vol. 3, page 857, 2009. (Cited on page 93.)

[Herculano-Houzel 2012] Suzana Herculano-Houzel. *The remarkable, yet not extraordinary, human brain as a scaled-up primate brain and its associated cost.* Proceedings of the National Academy of Sciences, vol. 109, no. supplement_1, pages 10661–10668, 2012. (Cited on page 93.)

[Hines 1984] Gail S. Hines. *Advances in simulation software technology.* SIMULATION, vol. 42, no. 1, pages 36–36, 1984. (Cited on page 96.)

[Hodgkin & Huxley 1952a] Alan L Hodgkin and Andrew F Huxley. *A quantitative description of membrane current and its application to conduction and excitation in nerve.* The Journal of physiology, vol. 117, no. 4, page 500, 1952. (Cited on pages 93 and 96.)

[Hodgkin & Huxley 1952b] Allan L Hodgkin and Andrew F Huxley. *The components of membrane conductance in the giant axon of Loligo.* The Journal of physiology, vol. 116, no. 4, page 473, 1952. (Cited on page 96.)

[Hodgkin & Huxley 1952c] Allan L Hodgkin and Andrew F Huxley. *Currents carried by sodium and potassium ions through the membrane of the giant axon of Loligo.* The Journal of physiology, vol. 116, no. 4, page 449, 1952. (Cited on page 96.)

[Hodgkin *et al.* 1952] Alan L Hodgkin, Andrew F Huxley and Bernard Katz. *Measurement of current-voltage relations in the membrane of the giant axon of Loligo.* The Journal of physiology, vol. 116, no. 4, page 424, 1952. (Cited on page 96.)

[Hou 2020] Jianghui Hou. *Biophysical Approaches for tight junction.* A Laboratory Guide to the Tight Junction, page 89–151, 2020. (Cited on page 5.)

[Houssaini *et al.* 2020] Kenza El Houssaini, Christophe Bernard and Viktor K. Jirsa. *The Epileptor Model: A Systematic Mathematical Analysis Linked to the Dynamics of Seizures, Refractory Status Epilepticus, and Depolarization Block.* eneuro, vol. 7, no. 2, pages ENEURO.0485–18.2019, 2020. (Cited on pages 41 and 68.)

[Huberfeld *et al.* 2007] Gilles Huberfeld, Lucia Wittner, Stéphane Clemenceau, Michel Baulac, Kai Kaila, Richard Miles and Claudio Rivera. *Perturbed chloride homeostasis and GABAergic signaling in Human Temporal Lobe Epilepsy.* The Journal of Neuroscience, vol. 27, no. 37, page 9866–9873, 2007. (Cited on page 89.)

[Jehi 2018] Lara Jehi. *The Epileptogenic Zone: Concept and Definition.* Epilepsy Currents, vol. 18, pages 12–16, 2018. (Cited on pages 68 and 77.)

[Jeong *et al.* 2000] H. Jeong, B. Tombor, R. Albert, Z. N. Oltvai and A.-L. Barabási. *The large-scale organization of metabolic networks.* Nature, vol. 407, no. 6804, page 651–654, 2000. (Cited on page 51.)

[Jirsa *et al.* 2014] Viktor K. Jirsa, William C. Stacey, Pascale P. Quilichini, Anton I. Ivanov and Christophe Bernard. *On the nature of seizure dynamics.* Brain, vol. 137, no. 8, pages 2210–2230, 2014. (Cited on pages 39 and 41.)

[Jirsa *et al.* 2016] V.K. Jirsa, T. Proix, Dionysios Perdikis, M.M. Woodman, Huifang Wang, Jorge Gonzalez-Martinez, Christophe Bernard, Christian Bénar, Maxime Guye, Patrick Chauvel and Fabrice Bartolomei. *The Virtual Epileptic Patient: Individualized whole-brain models of epilepsy spread:.* NeuroImage, vol. 145, 2016. (Cited on pages 45, 65 and 87.)

[Jirsa *et al.* 2017] V.K. Jirsa, T. Proix, D. Perdikis, M.M. Woodman, H. Wang, J. Gonzalez-Martinez, C. Bernard, C. Bénar, M. Guye, P. Chauvel and et al. *The virtual epileptic patient: Individualized whole-brain models of epilepsy spread.* NeuroImage, vol. 145, page 377–388, 2017. (Cited on page 65.)

[Jirsa *et al.* 2023] Viktor Jirsa, Huifang Wang, Paul Triebkorn, Meysam Hashemi, Jayant Jha, Jorge Gonzalez-Martinez, Maxime Guye, Julia Makhalova and Fabrice Bartolomei. *Personalised virtual brain models in epilepsy.* Lancet Neurol, vol. 22, no. 5, pages 443–454, 2023. (Cited on pages 65 and 90.)

[Jobst & Cascino 2015] Barbara C. Jobst and Gregory D. Cascino. *Resective epilepsy surgery for drug-resistant focal epilepsy.* JAMA, vol. 313, no. 3, page 285, 2015. (Cited on page 11.)

[Kaculini *et al.* 2021] Christian M Kaculini, Amelia J Tate-Looney and Ali Seifi. *The history of epilepsy: From ancient mystery to modern misconception.* Cureus, 2021. (Cited on page 2.)

[Kandel *et al.* 2013] Eric R. Kandel, James H. Schwartz, Thomas M. Jessell, Steven A. Siegelbaum and A. J. Hudspeth. Principles of neural science. McGraw-Hill, New York, 5th édition, 2013. (Cited on page 5.)

[Kang & Petrasek 2014] M. Kang and Z. Petrasek. *Random Graphs: Theory and Applocations from Nature to Society to the Brain.* Internationale Mathematische Nachrichten, vol. 227, pages 1–24, 2014. (Cited on page 63.)

[Kanner & Bicchi 2022] Andres M. Kanner and Manuel Melo Bicchi. *Antiseizure Medications for Adults With Epilepsy: A Review.* JAMA, vol. 327, no. 13, pages 1269–1281, 2022. (Cited on pages 66, 83 and 87.)

[Keezer *et al.* 2016] Mark R Keezer, Sanjay M Sisodiya and Josemir W Sander. *Comorbidities of epilepsy: Current concepts and future perspectives.* The Lancet Neurology, vol. 15, no. 1, page 106–115, 2016. (Cited on page 2.)

[Khateb *et al.* 2021] Mohamed Khateb, Noam Bosak and Moshe Herskovitz. *The Effect of Anti-seizure Medications on the Propagation of Epileptic Activity: A Review.* Frontiers in Neurology, vol. 12, 2021. (Cited on page 88.)

[Kuramoto 1984] Yoshiki Kuramoto. *Chemical Oscillations, Waves, and Turbulence.* In Springer Series in Synergetics, 1984. (Cited on pages 52 and 55.)

[Kusch *et al.* 2024] Lionel Kusch, Sandra Diaz-Pier, Wouter Klijn, Kim Sontheimer, Christophe Bernard, Abigail Morrison and Viktor Jirsa. *Multiscale co-simulation design pattern for neuroscience applications.* Frontiers in Neuroinformatics, vol. 18, page 1156683, 2024. (Cited on pages 94 and 101.)

[Ladwig *et al.* 2022] Zach Ladwig, Benjamin A. Seitzman, Ally Dworetsky, Yuhua Yu, Babatunde Adeyemo, Derek M. Smith, Steven E. Petersen and Caterina Gratton. *Bold cofluctuation 'events' are predicted from static functional connectivity.* NeuroImage, vol. 260, page 119476, 2022. (Cited on page 120.)

[Li & Cai 2004] W. Li and X. Cai. *Statistical analysis of airport network of China.* Physical Review E, vol. 69, no. 4, page 046106, 2004. (Cited on page 51.)

[Li & Cook 2018] Michael C. H. Li and Mark J. Cook. *Deep brain stimulation for drug-resistant epilepsy.* Epilepsia, vol. 59, no. 2, page 273–290, 2018. (Cited on page 13.)

[Liao *et al.* 2017] Xuhong Liao, Athanasios V. Vasilakos and Yong He. *Small-world human brain networks: Perspectives and challenges.* Neuroscience & Biobehavioral Reviews, vol. 77, page 286–300, 2017. (Cited on page 17.)

[Linssen *et al.* 2024] Charl Linssen, Pooja N. Babu, Younes Bouhadjar, Leander Ewert, Willem Wybo, Melissa Lober, Florian Feller, Bernhard Rumpe and Abigail Morrison. *NESTML 8.0.0*, 2024. (Cited on page 93.)

[Liu *et al.* 2020] Yuhan Liu, Vasily Grigorovsky and Berj Bardakjian. *Excitation and Inhibition Balance Underlying Epileptiform Activity.* IEEE Transactions on Biomedical Engineering, vol. 67, no. 9, page 2473–2481, 2020. (Cited on page 113.)

[Loligo 1952] AO Loligo. *The dual effect of membrane potential on sodium conductance in the giant.* J Physiol, vol. 6, pages 497–506, 1952. (Cited on page 96.)

[Lu *et al.* 2017] Wei Lu, Jing Feng, Bo Wen, Kewei Wang and Jin-Hui Wang. *Activity-induced spontaneous spikes in GABAergic neurons suppress seizure discharges: an implication of computational modeling.* Oncotarget, vol. 8, no. 20, pages 32384–32397, 2017. (Cited on page 90.)

[Lu *et al.* 2024] Han Lu, Sandra Diaz, Maximilian Lenz and Andreas Vlachos. *The interplay between homeostatic synaptic scaling and homeostatic structural plasticity maintains the robust firing rate of neural networks.* eLife, 2024. (Cited on pages 93 and 103.)

[Lu *et al.* 2025] Han Lu, Shreyash Garg, Maximilian Lenz and Andreas Vlachos. *Repetitive magnetic stimulation with iTBS600 induces persistent structural and functional plasticity in mouse organotypic slice cultures.* bioRxiv, 2025. (Cited on page 93.)

[Luboeinski & Tetzlaff 2021] Jannik Luboeinski and Christian Tetzlaff. *Memory consolidation and improvement by synaptic tagging and capture in recurrent neural networks.* Communications Biology, vol. 4, no. 1, page 275, 2021. (Cited on page 93.)

[Luboeinski *et al.* 2024] Jannik Luboeinski, Sebastian Schmitt, Shirin Shafiee, Thorsten Hater, Fabian Bösch and Christian Tetzlaff. *Plastic Arbor: a modern simulation framework for synaptic plasticity – from single synapses to networks of morphological neurons.* arXiv:2411.16445, 2024. (Cited on page 112.)

[Lv *et al.* 2018] H. Lv, Z. Wang, E. Tong, L. M. Williams, G. Zaharchuk, M. Zeineh, A. N. Goldstein-Piekarski, T. M. Ball, C. Liao and M. Wintermark. *Resting-State Functional MRI: Everything That Nonexperts Have Always Wanted to Know.* American Journal of Neuroradiology, vol. 39, no. 8, page 1390–1399, 2018. (Cited on page 20.)

[Lynn & Bassett 2019] Christopher W. Lynn and Danielle S. Bassett. *The physics of brain network structure, function and control.* Nature Reviews Physics, vol. 1, no. 5, page 318–332, 2019. (Cited on pages 21 and 22.)

[Magiorkinis *et al.* 2010] Emmanouil Magiorkinis, Kalliopi Sidiropoulou and Aristidis Diamantis. *Hallmarks in the history of epilepsy: Epilepsy in antiquity.* Epilepsy & Behavior, vol. 17, no. 1, page 103–108, 2010. (Cited on page 2.)

[Magiorkinis *et al.* 2014] Emmanouil Magiorkinis, Aristidis Diamantis, Kalliopi Sidiropoulou and Christos Panteliadis. *Highights in the history of epilepsy: The last 200 years.* Epilepsy Research and Treatment, vol. 2014, page 1–13, 2014. (Cited on page 2.)

[Makhalova *et al.* 2022] Julia Makhalova, Samuel Medina Villalon, Huifang Wang, Bernard Giusiano, Marmaduke Woodman, Christian Bénar, Maxime Guye, Viktor Jirsa and Fabrice Bartolomei. *Virtual epileptic patient brain modeling: Relationships with seizure onset and surgical outcome.* Epilepsia, vol. 63, no. 8, pages 1942–1955, 2022. (Cited on pages 45, 65 and 90.)

[Manos *et al.* 2018a] Thanos Manos, Magteld Zeitler and Peter A. Tass. *How stimulation frequency and intensity impact on the long-lasting effects of coordinated reset stimulation.* PLOS Computational Biology, vol. 14, no. 5, 2018. (Cited on page 52.)

[Manos *et al.* 2018b] Thanos Manos, Magteld Zeitler and Peter A. Tass. *Short-term dosage regimen for stimulation-induced long-lasting desynchronization.* Frontiers in Physiology, vol. 9, 2018. (Cited on page 52.)

[Manos *et al.* 2021] Thanos Manos, Sandra Diaz-Pier and Peter A. Tass. *Long-term desynchronization by coordinated reset stimulation in a neural network model with synaptic and structural plasticity.* Frontiers in Physiology, vol. 12, 2021. (Cited on pages 51 and 93.)

[Manos *et al.* 2023] Thanos Manos, Sandra Diaz-Pier, Igor Fortel, Ira Driscoll, Liang Zhan and Alex Leow. *Enhanced simulations of whole-brain dynamics using hybrid resting-state structural connectomes.* Front. Comput. Neurosci., vol. 17, page 1295395, 2023. (Cited on pages 65, 83, 89 and 121.)

[Marshall *et al.* 2021] Grant F. Marshall, Alfredo Gonzalez-Sulser and Catherine M. Abbott. *Modelling epilepsy in the mouse: Challenges and solutions.* Disease Models & Mechanisms, vol. 14, no. 3, 2021. (Cited on page 65.)

[Mecarelli 2019] Oriano Mecarelli, editeur. Clinical electroencephalography. Springer Cham, 1 édition, 2019. 343 b/w illustrations, 383 illustrations in colour. (Cited on page 20.)

[Meier *et al.* 2022] Jil M. Meier, Dionysios Perdikis, André Blickensdörfer, Leon Stefanovski, Qin Liu, Oliver Maith, Helge Ü. Dinkelbach, Javier Baladron, Fred H. Hamker and Petra Ritter. *Virtual deep brain stimulation: Multiscale co-simulation of a spiking basal ganglia model and a whole-brain mean-field model with The Virtual Brain.* Experimental Neurology, vol. 354, page 114111, 2022. (Cited on page 94.)

[Melozzi *et al.* 2017] Francesca Melozzi, Marmaduke Woodman, Viktor Jirsa and Christophe Bernard. *The Virtual Mouse Brain: A Computational Neuroinformatics Platform To Study Whole Mouse Brain Dynamics.* eNeuro, 2017. (Cited on pages 23, 41, 45, 49, 65, 66, 68, 69, 70, 77, 87, 107, 120 and 121.)

[Meunier *et al.* 2010] David Meunier, Renaud Lambiotte and Edward T. Bullmore. *Modular and Hierarchically Modular Organization of Brain Networks.* Frontiers in Neuroscience, vol. 4, 2010. (Cited on page 19.)

[Miller & Hakimian 2013] John W. Miller and Shahin Hakimian. *Surgical treatment of epilepsy.* CONTINUUM: Lifelong Learning in Neurology, vol. 19, page 730–742, 2013. (Cited on page 11.)

[Miner & Triesch 2016] Daniel Miner and Jochen Triesch. *Plasticity-driven self-organization under topological constraints accounts for non-random features of cortical synaptic wiring.* PLOS Computational Biology, vol. 12, no. 2, page e1004759, 2016. (Cited on page 93.)

[Mirollo & Strogatz 2007] R. Mirollo and S.H. Strogatz. *The Spectrum of the Partially Locked State for the Kuramoto Model.* Journal of Nonlinear Science, vol. 17, no. 4, page 309–347, 2007. (Cited on page 55.)

[Mlinar *et al.* 2016] Simona Mlinar, Davorina Petek, Živa Cotič, Metka Mencin Čeplak and Marjan Zaletel. *Persons with Epilepsy: Between Social Inclusion and Marginalisation.* Behavioural Neurology, vol. 2016, page 1–10, 2016. (Cited on page 3.)

[Monteverdi *et al.* 2023] Anita Monteverdi, Fulvia Palesi, Michael Schirner, Francesca Argentino, Mariateresa Merante, Alberto Redolfi, Francesca Conca, Laura Mazzocchi, Stefano F Cappa, Matteo Cotta Ramusino*et al. Virtual brain simulations reveal network-specific parameters in neurodegenerative dementias.* Frontiers in Aging Neuroscience, vol. 15, page 1204134, 2023. (Cited on page 94.)

[Naidich *et al.* 2013] Thomas P. Naidich, Mauricio Castillo, Soonmee Cha and James G. Smirniotopoulos, editeurs. Imaging of the brain. Expert Radiology Series, Expert Consult- Online and Print. Elsevier/Saunders, Philadelphia, PA, 2013. (Cited on page 20.)

[Nayebi *et al.* 2021] Aran Nayebi, Alexander Attinger, Malcolm Campbell, Kiah Hardcastle, Isabel Low, Caitlin S Mallory, Gabriel Mel, Ben Sorscher, Alex H Williams, Surya Ganguli, Lisa Giocomo and Dan Yamins. *Explaining heterogeneity in medial entorhinal cortex with task-driven neural networks.* In M. Ranzato, A. Beygelzimer, Y. Dauphin, P.S. Liang and J. Wortman Vaughan, editeurs, Advances in Neural Information Processing Systems, volume 34, pages 12167–12179. Curran Associates, Inc., 2021. (Cited on page 93.)

[Netoff *et al.* 2004] Theoden I. Netoff, Robert Clewley, Scott Arno, Tara Keck and John A. White. *Epilepsy in Small-World Networks.* The Journal of Neuroscience, vol. 24, no. 37, pages 8075–8083, 2004. (Cited on page 113.)

[Newman 2006] M. E. J. Newman. *Modularity and community structure in networks.* Proceedings of the National Academy of Sciences, vol. 103, no. 23, page 8577–8582, 2006. (Cited on page 19.)

[Newman 2010] Mark Newman. Networks: An introduction. Oxford University Press, 2010. (Cited on pages 14 and 15.)

[Nicolis & Nicolis 2012] Gregoire Nicolis and Catherine Nicolis. Foundations of complex systems: Emergence, information and prediction. World Scientific Publishing Co., Inc., USA, 2nd édition, 2012. (Cited on page 51.)

[Nissen *et al.* 2021] Ida A. Nissen, Ana P. Millán, Cornelis J. Stam, Elisabeth C. van Straaten, Linda Douw, Petra J. Pouwels, Sander Idema, Johannes C. Baayen, Demetrios Velis, Piet Van Mieghem and et al. *Optimization of epilepsy surgery through virtual resections on individual structural brain networks.* Scientific Reports, vol. 11, no. 1, 2021. (Cited on pages 45, 65 and 87.)

[Novak *et al.* 2022] Ajda Novak, Karmen Vizjak and Martin Rakusa. *Cognitive impairment in people with epilepsy.* Journal of Clinical Medicine, vol. 11, no. 1, page 267, 2022. (Cited on page 91.)

[Oh *et al.* 2014] Seung Wook Oh, Julie A. Harris, Lydia Ng, Brent Winslow, Nicholas Cain, Stefan Mihalas, Quanxin Wang, Chris Lau, Leonard Kuan, Alex M. Henry and et al. *A mesoscale connectome of the Mouse Brain.* Nature, vol. 508, no. 7495, page 207–214, 2014. (Cited on pages 21, 23, 69 and 107.)

[Olmi *et al.* 2019] Simona Olmi, Spase Petkoski, Maxime Guye, Fabrice Bartolomei and Viktor Jirsa. *Controlling seizure propagation in large-scale brain networks.* PLOS Computational Biology, vol. 15, no. 2, 2019. (Cited on pages 65 and 87.)

[Onos *et al.* 2022] Kristen D. Onos, Sara K. Quinney, David R. Jones, Andrea R. Masters, Ravi Pandey, Kelly J. Keezer, Carla Biesdorf, Ingrid F. Metzger, Jill A. Meyers, Johnathon Peters and et al. *Pharmacokinetic, pharmacodynamic, and transcriptomic analysis of chronic levetiracetam treatment in 5XFAD mice: A Model-AD Preclinical Testing Core Study.* Alzheimer's & Dementia: Translational Research & Clinical Interventions, vol. 8, no. 1, 2022. (Cited on page 89.)

[Ott 2002] Edward Ott. Chaos in dynamical systems. Cambridge University Press, 2 édition, 2002. (Cited on pages 26 and 29.)

[Petkoski & Jirsa 2019] Spase Petkoski and Viktor K. Jirsa. *Transmission time delays organize the brain network synchronization.* Philosophical Transactions of the Royal Society A: Mathematical, Physical and Engineering Sciences, vol. 377, no. 2153, page 20180132, 2019. (Cited on page 90.)

[Pikovsky *et al.* 2001] Arkady S Pikovsky, Michael Rosenblum and Jürgen Kurths. *Synchronization: A Universal Concept in Nonlinear Sciences.* 2001. (Cited on pages 51 and 58.)

[Poldrack & Gorgolewski 2017] Russell A Poldrack and Krzysztof J Gorgolewski. *OpenfMRI: Open sharing of task fMRI data.* Neuroimage, vol. 144, pages 259–261, 2017. (Cited on page 93.)

[Popovych *et al.* 2019] Oleksandr V. Popovych, Thanos Manos, Felix Hoffstaedter and Simon B. Eickhoff. *What can computational models contribute to neuroimaging data analytics?* Frontiers in Systems Neuroscience, vol. 12, 2019. (Cited on pages 65 and 93.)

[Popovych *et al.* 2021] Oleksandr V. Popovych, Kyesam Jung, Thanos Manos, Sandra Diaz-Pier, Felix Hoffstaedter, Jan Schreiber, B.T. Thomas Yeo and Simon B. Eickhoff. *Inter-subject and inter-parcellation variability of resting-state whole-brain dynamical modeling.* NeuroImage, vol. 236, page 118201, 2021. (Cited on pages 52, 65 and 121.)

[Proix *et al.* 2018] Timothée Proix, Viktor K. Jirsa, Fabrice Bartolomei, Maxime Guye and Wilson Truccolo. *Predicting the spatiotemporal diversity of seizure propagation and termination in human focal epilepsy.* Nature Communications, vol. 9, no. 1, 2018. (Cited on page 43.)

[Quigg *et al.* 2011] Mark Quigg, John Rolston and Nicholas M. Barbaro. *Radiosurgery for epilepsy: Clinical experience and potential antiepileptic mechanisms.* Epilepsia, vol. 53, no. 1, page 7–15, 2011. (Cited on page 12.)

[Quinarez *et al.* 2023] Rachel Vital Quinarez, Mayuresh V. Kothare and Gautam Kumar. *Forced temporal spiking timing stimulation to control frequency-specific oscillations in epileptic seizures: A computational study.* Brain Stimulation, vol. 16, no. 1, page 274–275, 2023. (Cited on page 89.)

[Rabuffo *et al.* 2024] Giovanni Rabuffo, Abhirup Bandyopadhyay, Carmela Calabrese, Kashyap Gudibanda, Damien Depannemaecker, Lavinia Mitiko Takarabe, Maria Luisa Saggio, Mathieu Desroches, Anton Ivanov, Marja-Leena Linne, Christophe Bernard, Spase Petkoski and Viktor K. Jirsa. *Biophysically inspired mean-field model of neuronal populations driven by ion exchange mechanisms.* bioRxiv, 2024. (Cited on page 99.)

[Raghavan *et al.* 2019] Manoj Raghavan, Dominic Fee and Paul E. Barkhaus. *Generation and propagation of the action potential.* Handbook of Clinical Neurology, page 3–22, 2019. (Cited on page 6.)

[Rao & Rolston 2023] Vikram R. Rao and John D. Rolston. *Unearthing the mechanisms of responsive neurostimulation for epilepsy.* Communications Medicine, vol. 3, no. 1, page 166, 2023. (Cited on page 13.)

[Reyes 2003] Alex D Reyes. *Synchrony-dependent propagation of firing rate in iteratively constructed networks in vitro.* Nature neuroscience, vol. 6, no. 6, pages 593–599, 2003. (Cited on page 93.)

[Reynolds 2004] Edward H Reynolds. *Todd, faraday, and the electrical basis of brain activity.* The Lancet Neurology, vol. 3, no. 9, page 557–563, 2004. (Cited on page 2.)

[Ribeiro *et al.* 2021] Tiago L. Ribeiro, Dante R. Chialvo and Dietmar Plenz. *Scale-Free Dynamics in Animal Groups and Brain Networks.* Frontiers in Systems Neuroscience, vol. 14, page 591210, 2021. (Cited on page 63.)

[Ritter *et al.* 2013] Petra Ritter, Michael Schirner, Anthony R McIntosh and Viktor K Jirsa. *The virtual brain integrates computational modeling and multimodal neuroimaging.* Brain Connectivity, vol. 3, no. 2, pages 121–145, 2013. (Cited on page 94.)

[Rodrigues *et al.* 2015] Francisco A. Rodrigues, Thomas K. DM. Peron, Peng Ji and Jürgen Kurths. *The Kuramoto model in complex networks.* Physics Reports, 2015. (Cited on page 52.)

[Roopun 2008] Anita K Roopun. *Temporal interactions between cortical rhythms.* frontiers in Neuroscience, vol. 2, no. 2, page 145–154, 2008. (Cited on page 89.)

[Rouhani *et al.* 2023] Ehsan Rouhani, Ehsan Jafari and Amir Akhavan. *Suppression of seizure in childhood absence epilepsy using robust control of deep brain stimulation: A simulation study.* Scientific Reports, vol. 13, no. 1, 2023. (Cited on page 88.)

[Rubio *et al.* 2019] Carmen Rubio, Elisa Taddei, Veronica Custodio and Carlos Paz. *Surgical alternatives for the control of epileptic seizures.* Neurology and Neurosurgery, vol. 2, no. 2, 2019. (Cited on page 77.)

[Sacramento *et al.* 2015] João Sacramento, Andreas Wichert and Mark CW van Rossum. *Energy efficient sparse connectivity from imbalanced synaptic plasticity rules.* PLOS Computational Biology, vol. 11, no. 6, page e1004265, 2015. (Cited on page 93.)

[Saggio & Jirsa 2024] Maria Luisa Saggio and Viktor Jirsa. *Bifurcations and bursting in the Epileptor.* PLOS Computational Biology, vol. 20, no. 3, 2024. (Cited on page 41.)

[Sandler *et al.* 2018] Roman A. Sandler, Kunling Geng, Dong Song, Robert E. Hampson, Mark R. Witcher, Sam A. Deadwyler, Theodore W. Berger and Vasilis Z. Marmarelis. *Designing patient-specific optimal neurostimulation patterns for seizure suppression.* Neural Computation, vol. 30, no. 5, page 1180–1208, 2018. (Cited on page 88.)

[Sankaraneni & Lachhwani 2015] Ram Sankaraneni and Deepak Lachhwani. *Antiepileptic drugs—a review.* Pediatric Annals, vol. 44, no. 2, 2015. (Cited on pages 6 and 11.)

[Sanz Leon *et al.* 2013] Paula Sanz Leon, Stuart Knock, M. Woodman, Lia Domide, Jochen Mersmann, Anthony McIntosh and Viktor Jirsa. *The Virtual Brain: a simulator of primate brain network dynamics.* Frontiers in Neuroinformatics, vol. 7, 2013. (Cited on pages 49, 68 and 94.)

[Sanz-Leon *et al.* 2015] Paula Sanz-Leon, Stuart A. Knock, Andreas Spiegler and Viktor K. Jirsa. *Mathematical framework for large-scale brain network modeling in the virtual brain.* NeuroImage, vol. 111, page 385–430, 2015. (Cited on pages 49, 68 and 94.)

[Scheffer *et al.* 2017] Ingrid E. Scheffer, Samuel Berkovic, Giuseppe Capovilla, Mary B. Connolly, Jacqueline French, Laura Guilhoto, Edouard Hirsch, Satish Jain, Gary W. Mathern, Solomon L. Moshé, Douglas R. Nordli, Emilio Perucca, Torbjörn Tomson, Samuel Wiebe, Yue-Hua Zhang and Sameer M. Zuberi. *ILAE classification of the epilepsies: Position paper of the ILAE Commission for Classification and Terminology.* Epilepsia, vol. 58, no. 4, page 512–521, 2017. (Cited on page 7.)

[Schirner *et al.* 2022] Michael Schirner, Lia Domide, Dionysios Perdikis, Paul Triebkorn, Leon Stefanovski, Roopa Pai, Paula Prodan, Bogdan Valean, Jessica Palmer, Chloê Langford, André Blickensdörfer, Michiel van der Vlag, Sandra Diaz-Pier, Alexander Peyser, Wouter Klijn, Dirk Pleiter, Anne Nahm, Oliver Schmid, Marmaduke Woodman, Lyuba Zehl, Jan Fousek, Spase Petkoski, Lionel Kusch, Meysam Hashemi, Daniele Marinazzo, Jean-François Mangin, Agnes Flöel, Simisola Akintoye, Bernd Carsten Stahl, Michael Cepic, Emily Johnson, Gustavo Deco, Anthony R. McIntosh, Claus C. Hilgetag, Marc Morgan, Bernd Schuller, Alex Upton, Colin McMurtrie, Timo Dickscheid, Jan G. Bjaalie, Katrin Amunts, Jochen Mersmann, Viktor Jirsa and Petra Ritter. *Brain simulation as a cloud service: The Virtual Brain on EBRAINS.* NeuroImage, vol. 251, page 118973, 2022. (Cited on page 94.)

[Scott 1975] Alwyn C Scott. *The electrophysics of a nerve fiber.* Reviews of Modern Physics, vol. 47, no. 2, page 487, 1975. (Cited on page 96.)

[Seitzman *et al.* 2019] Benjamin A. Seitzman, Abraham Z. Snyder, Eric C. Leuthardt and Joshua S. Shimony. *The State of Resting State Networks.*

Topics in Magnetic Resonance Imaging, vol. 28, no. 4, page 189–196, 2019. (Cited on page 24.)

[Shaheen *et al.* 2022] Hina Shaheen, Swadesh Pal and Roderick Melnik. *Multiscale co-simulation of deep brain stimulation with brain networks in neurodegenerative disorders.* Brain Multiphysics, vol. 3, page 100058, 2022. (Cited on page 94.)

[Shukla *et al.* 2017] Navika Shukla, Allen L Ho, Arjun Pendharkar, Eric Sussman and Casey Halpern. *Laser interstitial thermal therapy for the treatment of epilepsy: Evidence to date.* Neuropsychiatric Disease and Treatment, vol. Volume 13, page 2469–2475, 2017. (Cited on page 12.)

[Shusterman & Troy 2008] Vladimir Shusterman and William C. Troy. *From baseline to epileptiform activity: A path to synchronized rhythmicity in large-scale neural networks.* Physical Review E, vol. 77, no. 6, 2008. (Cited on page 65.)

[Sidiropoulou *et al.* 2010] K. Sidiropoulou, A. Diamantis and E. Magiorkinis. *Hallmarks in 18th- and 19th-century epilepsy research.* Epilepsy & Behavior, vol. 18, no. 3, page 151–161, 2010. (Cited on page 2.)

[Sillanpää *et al.* 2017] Matti Sillanpää, Dieter Schmidt, Maiju M. Saarinen and Shlomo Shinnar. *Remission in epilepsy: How long is enough?* Epilepsia, vol. 58, no. 5, page 901–906, 2017. (Cited on page 9.)

[Skrehot *et al.* 2023] Henry C. Skrehot, Dario J. Englot and Zulfi Haneef. *Neurostimulation in focal epilepsy: A systematic review and meta-analysis.* Epilepsy & Behavior, vol. 142, page 109182, 2023. (Cited on page 88.)

[Spencer *et al.* 2002] Susan S. Spencer, Johannes Schramm, Allen Wyler, Michael O'Connor, Darren Orbach, Gregory Krauss, Michael Sperling, Orrin Devinsky, Christian Elger, Ronald Lesser, Lisa Mulligan and Michael Westerveld. *Multiple Subpial Transection for Intractable Partial Epilepsy: An International Meta-analysis.* Epilepsia, vol. 43, no. 2, page 141–145, 2002. (Cited on page 12.)

[Sporns 2010] Olaf Sporns. Networks of the brain. The MIT Press, 2010. (Cited on page 51.)

[Sporns 2013] Olaf Sporns. *Structure and function of Complex Brain Networks.* Dialogues in Clinical Neuroscience, vol. 15, no. 3, page 247–262, 2013. (Cited on pages 21 and 22.)

[Stafford *et al.* 2014] James M. Stafford, Benjamin R. Jarrett, Oscar Miranda-Dominguez, Brian D. Mills, Nicholas Cain, Stefan Mihalas, Garet P. Lahvis, K. Matthew Lattal, Suzanne H. Mitchell, Stephen V. David and et al. *Large-scale topology and the default mode network in the mouse connectome.*

Proceedings of the National Academy of Sciences, vol. 111, no. 52, page 18745–18750, 2014. (Cited on page 65.)

[Stam *et al.* 2009] C. J. Stam, W. De Haan, A. Daffertshofer, B. F. Jones, I. Manshanden, A. M. Van Cappellen Van Walsum, T. Montez, J. P. A. Verbunt, J. C. De Munck, B. W. Van Dijk, H. W. Berendse and P. Scheltens. *Graph theoretical analysis of magnetoencephalographic functional connectivity in Alzheimer's disease.* Brain, vol. 132, no. 1, page 213–224, 2009. (Cited on page 63.)

[Stefanovski *et al.* 2021] Leon Stefanovski, Jil Mona Meier, Roopa Kalsank Pai, Paul Triebkorn, Tristram Lett, Leon Martin, Konstantin Bülau, Martin Hofmann-Apitius, Ana Solodkin, Anthony Randal McIntosh*et al. Bridging scales in Alzheimer's disease: biological framework for brain simulation with the virtual brain.* Frontiers in Neuroinformatics, vol. 15, page 630172, 2021. (Cited on page 94.)

[Stephan & Friston 2009] K.E. Stephan and K.J. Friston. *Functional connectivity.* Encyclopedia of Neuroscience, page 391–397, 2009. (Cited on page 120.)

[Stimberg *et al.* 2019] Marcel Stimberg, Romain Brette and Dan FM Goodman. *Brian 2, an intuitive and efficient neural simulator.* eLife, vol. 8, page e47314, 2019. (Cited on page 93.)

[Strogatz 2001] Steven H. Strogatz. *Exploring complex networks.* Nature, vol. 410, no. 6825, page 268–276, 2001. (Cited on page 51.)

[Strogatz 2018] Steven H. Strogatz. Nonlinear dynamics and chaos. CRC Press, 0 édition, 2018. (Cited on pages 26 and 51.)

[Suma *et al.* 2024] Antonio Suma, Daniel Sigg, Seamus Gallagher, Giuseppe Gonnella and Vincenzo Carnevale. *Ion channels in critical membranes: clustering, cooperativity, and memory effects.* PRX Life, vol. 2, no. 1, page 013007, 2024. (Cited on page 93.)

[Sumadewi *et al.* 2023] Komang Trisna Sumadewi, Saktivi Harkitasari and David Christopher Tjandra. *Biomolecular mechanisms of epileptic seizures and epilepsy: A Review.* Acta Epileptologica, vol. 5, no. 1, 2023. (Cited on page 7.)

[Sánchez *et al.* 2024] J. Domingo Sánchez, Jorge Gómez-Carpintero, Juan F. González and J. Carlos Menéndez. *Twenty-first century antiepileptic drugs. an overview of their targets and synthetic approaches.* European Journal of Medicinal Chemistry, vol. 272, page 116476, 2024. (Cited on page 11.)

[Taylor *et al.* 2014] Peter Neal Taylor, Yujiang Wang, Marc Goodfellow, Justin Dauwels, Friederike Moeller, Ulrich Stephani and Gerold Baier. *A computational study of stimulus driven epileptic seizure abatement.* PLoS ONE, vol. 9, no. 12, 2014. (Cited on page 88.)

[Tetzlaff *et al.* 2025] Svenja K Tetzlaff, Ekin Reyhan, Nikolas Layer, C Peter Bengtson, Alina Heuer, Julian Schroers, Anton J Faymonville, Atefeh Pourkhalili Langeroudi, Nina Drewa, Elijah Keifert*et al.* *Characterizing and targeting glioblastoma neuron-tumor networks with retrograde tracing.* Cell, vol. 188, no. 2, pages 390–411, 2025. (Cited on page 93.)

[Thom 2014] Maria Thom. *Review: Hippocampal sclerosis in epilepsy: A Neuropathology Review.* Neuropathology and Applied Neurobiology, vol. 40, no. 5, page 520–543, 2014. (Cited on page 8.)

[Thompson & Kelvin 1855] William Thompson and L Kelvin. *On the theory of the electric telegraph.* Proc. Royal Soc. London, vol. 7, pages 382–399, 1855. (Cited on page 96.)

[Tigerholm *et al.* 2014] Jenny Tigerholm, Marcus E Petersson, Otilia Obreja, Angelika Lampert, Richard Carr, Martin Schmelz and Erik Fransén. *Modeling activity-dependent changes of axonal spike conduction in primary afferent C-nociceptors.* Journal of Neurophysiology, vol. 111, no. 9, pages 1721–1735, 2014. (Cited on page 93.)

[Tigerholm *et al.* 2015] Jenny Tigerholm, Marcus E Petersson, Otilia Obreja, Esther Eberhardt, Barbara Namer, Christian Weidner, Angelika Lampert, Richard W Carr, Martin Schmelz and Erik Fransén. *C-fiber recovery cycle supernormality depends on ion concentration and ion channel permeability.* Biophysical Journal, vol. 108, no. 5, pages 1057–1071, 2015. (Cited on page 93.)

[Toffa *et al.* 2020] Dènahin Hinnoutondji Toffa, Lahoud Touma, Tahir El Meskine, Alain Bouthillier and Dang Khoa Nguyen. *Learnings from 30 years of reported efficacy and safety of vagus nerve stimulation (VNS) for epilepsy treatment: A critical review.* Seizure, vol. 83, pages 104–123, 2020. (Cited on pages 66 and 83.)

[Toyoda *et al.* 2013] Izumi Toyoda, Mark R Bower, Fernando Leyva and Paul S Buckmaster. *Early activation of ventral hippocampus and subiculum during spontaneous seizures in a rat model of temporal lobe epilepsy.* J Neurosci, vol. 33, no. 27, pages 11100–11115, 2013. (Cited on pages 65, 66, 70 and 77.)

[Tsuboyama *et al.* 2020] Melissa Tsuboyama, Harper L Kaye and Alexander Rotenberg. *Review of Transcranial Magnetic Stimulation in Epilepsy.* Clin Ther, vol. 42, no. 7, pages 1155–1168, 2020. (Cited on pages 66, 83 and 87.)

[Tufenkjian & Lüders 2012] Krikor Tufenkjian and Hans O. Lüders. *Seizure semiology: Its value and limitations in localizing the Epileptogenic Zone.* Journal of Clinical Neurology, vol. 8, no. 4, page 243, 2012. (Cited on page 9.)

[van den Heuvel & Hulshoff Pol 2010] Martijn P. van den Heuvel and Hilleke E. Hulshoff Pol. *Exploring the brain network: A review on resting-state fMRI*

functional connectivity. European Neuropsychopharmacology, vol. 20, no. 8, page 519–534, 2010. (Cited on page 25.)

[van den Heuvel & Sporns 2013] Martijn P. van den Heuvel and Olaf Sporns. *Network hubs in the human brain.* Trends in Cognitive Sciences, vol. 17, no. 12, page 683–696, 2013. (Cited on page 19.)

[van den Heuvel & Sporns 2019] Martijn P van den Heuvel and Olaf Sporns. *A cross-disorder connectome landscape of brain dysconnectivity.* Nat Rev Neurosci, vol. 20, no. 7, pages 435–446, 2019. (Cited on page 87.)

[Van Rossum *et al.* 2000] Mark CW Van Rossum, Guo Qiang Bi and Gina G Turrigiano. *Stable Hebbian learning from spike timing-dependent plasticity.* Journal of neuroscience, vol. 20, no. 23, pages 8812–8821, 2000. (Cited on page 103.)

[Vattikonda *et al.* 2021] Anirudh N. Vattikonda, Meysam Hashemi, Viktor Sip, Marmaduke M. Woodman, Fabrice Bartolomei and Viktor K. Jirsa. *Identifying spatio-temporal seizure propagation patterns in epilepsy using Bayesian inference.* Communications Biology, vol. 4, no. 1, page 1244, 2021. (Cited on page 43.)

[Von Helmholz 1850] H Von Helmholz. *Messungen über den zeitlichen Verlauf der Zuckung animalischer Muskeln und die Fortpflanzungsgeschwindigkeit der Reizung in den Nerven.* Archiv für Anatomie, Physiologie und wissenschaftliche Medicin, vol. 17, pages 176–364, 1850. (Cited on page 96.)

[Vossel *et al.* 2021] Keith Vossel, Kamalini G. Ranasinghe, Alexander J. Beagle, Alice La, Kasey Ah Pook, Madelyn Castro, Danielle Mizuiri, Susanne M. Honma, Nisha Venkateswaran, Mary Koestler and et al. *Effect of levetiracetam on cognition in patients with alzheimer disease with and without epileptiform activity.* JAMA Neurology, vol. 78, no. 11, page 1345, 2021. (Cited on page 89.)

[Walker 2015] Matthew Walker. *Hippocampal sclerosis: Causes and prevention.* Seminars in Neurology, vol. 35, no. 03, page 193–200, 2015. (Cited on page 8.)

[Walls *et al.* 2014] Anne B. Walls, Helle S. Waagepetersen, Lasse K. Bak, Arne Schousboe and Ursula Sonnewald. *The glutamine–glutamate/GABA cycle: Function, regional differences in glutamate and GABA production and effects of interference with GABA metabolism.* Neurochemical Research, vol. 40, no. 2, page 402–409, 2014. (Cited on page 7.)

[Wang *et al.* 2023] Xiu Wang, Chang Liu, Zhong Zheng, Wenhan Hu, Chao Zhang, Xiaoli Yang, Xiaoqiu Shao, Jian-Guo Zhang and Kai Zhang. *Epilepsy in hypothalamic hamartomas: Semiology Spectrum and predictor analyses of 78 patients.* Annals of Clinical and Translational Neurology, vol. 10, no. 8, page 1365–1373, 2023. (Cited on page 8.)

[Wang 2002] Xiao-Jing Wang. *Probabilistic decision making by slow reverberation in cortical circuits.* Neuron, vol. 36, no. 5, page 955–968, 2002. (Cited on pages 34 and 99.)

[Watts & Strogatz 1998] Duncan J. Watts and Steven H. Strogatz. *Collective dynamics of 'small-world' networks.* Nature, vol. 393, no. 6684, page 440–442, 1998. (Cited on pages 17, 51 and 53.)

[West *et al.* 2002] Anne E West, Eric C Griffith and Michael E Greenberg. *Regulation of transcription factors by neuronal activity.* Nature Reviews Neuroscience, vol. 3, no. 12, pages 921–931, 2002. (Cited on page 93.)

[Wicks *et al.* 2016] Robert T. Wicks, Walter J. Jermakowicz, Jonathan R. Jagid, Daniel E. Couture, Jon T. Willie, Adrian W. Laxton and Robert E. Gross. *Laser interstitial thermal therapy for Mesial Temporal Lobe epilepsy.* Neurosurgery, vol. 79, no. Supplement 1, 2016. (Cited on page 12.)

[Wong & Wang 2006] Kong-Fatt Wong and Xiao-Jing Wang. *A recurrent network mechanism of time integration in perceptual decisions.* The Journal of Neuroscience, vol. 26, no. 4, page 1314–1328, 2006. (Cited on pages 35 and 36.)

[Wong *et al.* 1986] Robert K. S. Wong, Roger D. Traub and Richard Miles. *Cellular basis of neuronal synchrony in epilepsy.* Advances in neurology, vol. 44, pages 583–92, 1986. (Cited on page 51.)

[Wu *et al.* 2021] Ying-Chang Wu, Ying-Siou Liao, Wen-Hsiu Yeh, Sheng-Fu Liang and Fu-Zen Shaw. *Directions of Deep Brain Stimulation for Epilepsy and Parkinson's Disease.* Frontiers in Neuroscience, vol. 15, page 680938, 2021. (Cited on page 13.)

[Yasumatsu *et al.* 2008] Nobuaki Yasumatsu, Masanori Matsuzaki, Takashi Miyazaki, Jun Noguchi and Haruo Kasai. *Principles of long-term dynamics of dendritic spines.* Journal of Neuroscience, vol. 28, no. 50, pages 13592–13608, 2008. (Cited on page 93.)

[Yizhar *et al.* 2011] Ofer Yizhar, Lief E. Fenno, Matthias Prigge, Franziska Schneider, Thomas J. Davidson, Daniel J. O'Shea, Vikaas S. Sohal, Inbal Goshen, Joel Finkelstein, Jeanne T. Paz and et al. *Neocortical excitation/inhibition balance in information processing and social dysfunction.* Nature, vol. 477, no. 7363, page 171–178, 2011. (Cited on page 89.)

[Zheng *et al.* 2013] Pengsheng Zheng, Christos Dimitrakakis and Jochen Triesch. *Network self-organization explains the statistics and dynamics of synaptic connection strengths in cortex.* PLOS Computational Biology, vol. 9, no. 1, page e1002848, 2013. (Cited on page 93.)

[Zhou *et al.* 2020] Bo Zhou, Yanqiu Che, Qing Qin, Yingmei Qin and Chunxiao Han. *Seizure suppression in a thalamocortical computational model of absence*

epilepsy by linear delayed feedback control. 2020 13th International Congress on Image and Signal Processing, BioMedical Engineering and Informatics (CISP-BMEI), 2020. (Cited on page 90.)